Preparation and investigation of anode materials with highly conductive materials for high-performance lithium-ion batteries

高导电材料在锂离子电池负极材料中的制备与研究

A Thesis Submitted to

University of Liverpool

in Partial Fulfillment of the Requirements for

the Degree of Doctor of Philosophy

in the Department of Electrical Engineering and Electronics

by

Yinchao Zhao

BEng Electrical and Electronic Engineering

Xi'an Jiaotong-Liverpool University

Abstract

With the increased demand for developing energy storage technologies, lithium-ion batteries have been considered as one of the most promising candidates due to its high energy density, excellent cyclic performance, and environmental benignity. Indeed, extensive applications of lithium-ion batteries are witnessed in the market, for example, in portable electronic equipment. However, the commercialized graphite anodes for lithium-ion batteries exhibiting low theoretical specific capacity is far from meeting the tremendous demands created by the fast-growing market. Therefore, enormous efforts have been devoted to developing desirable electrode materials with better recyclability and advanced capacity for next-generation lithium-ion batteries.

Although alloy anode materials like silicon have the highest gravimetric and volumetric capacity, its huge volume change and low electron and ions conductivity still hinder the broad application in other fields, such as large-scale energy storage systems. Similar challenges also impede the wide implementation of conversion materials in Li-ion batteries. This work is focused on employing different highly conductive materials to improve the electrical conductivity of the entire electrode. At the same time, the formation of the conductive framework is beneficial to accommodate the substantial volume change of the active materials.

In **Chapter 3**, copper nanowires and multi-wall carbon nanotubes coated on the surface of Cu foils built a porous substrate to support the active materials. Silicon was

deposited on the porous substrate by the template of copper nanowires and multi-wall carbon nanotubes. The formation of copper nanowires/silicon and multi-wall carbon nanotubes/silicon core-shell structures intrinsically reduces the volume expansion of active materials. Meanwhile, the poles created by the intertwined copper nanowires and multi-wall carbon nanotubes further accommodate the stress from volume change. In addition, the copper nanowires/silicon and multi-wall carbon nanotubes/silicon core-shell structure provide the highly efficient electrons and Li^+ diffusion pathways. As a result, we have demonstrated that multi-wall carbon nanotubes/copper nanowires/silicon delivers a high specific capacity of 1845 mAh g^{-1} in a half cell at a current density of 3.5 A g^{-1} after 180 cycles with a capacity retention of 85.1 %.

In **Chapter 4**, a free-standing silicon-based anode was developed by preparing a three-dimensional copper nanowires/silicon nanoparticles@carbon composite using freeze-drying. Silicon nanoparticles were uniformly attached along with the copper nanowires, which was reinforced by the carbon coatings. The three-dimensional conductive structure allows the silicon nanoparticles to distribute evenly as well as enhance the electrical and ionic conductivity of the whole electrode. Similarly, considerable interspace produced by the three-dimensional structure can relieve the stress produced by the vast volume expansion of silicon nanoparticles, which is also restricted by the carbon coating layers during the charge and discharge processes. Moreover, the outer layers strengthen the stability of the three-dimensional framework and the contact between the copper nanowires and silicon nanoparticles. The electrochemical performance of copper nanowires/silicon nanoparticles@carbon

composite electrode has been measured, which exhibits excellent cycling performance.

In **Chapter 5**, a new highly conductive material, MXene nanosheets, was introduced to promote the electrochemical performance in lithium-ion batteries. In this chapter, the cobalt oxides were chosen as the active material for its controllable and facile synthesis methods. Meanwhile, cobalt oxides, one of the conversion materials as anodes for lithium-ion batteries, face similar issues with silicon. Therefore, an anode involving cobalt oxides nanoparticles mixed with MXene nanosheets on Ni foams has been developed. Small-size cobalt oxides nanoparticles were uniformly distributed within the MXene nanosheets leading to high lithium ions and electrons transmission efficiency, as well as preventing restacking of MXene nanosheets and colossal volume change of the cobalt oxides nanoparticles. As shown in Chapter 5, cobalt oxides /MXene composite electrode remains a stable capacity of 307 mAh g^{-1} after 1000 cycles when the current density approaches 5 C, which indicates the enormous potential of cobalt oxides/MXene composite as an anode for the high-performance lithium-ion batteries.

Keywords: Lithium-ion batteries; Silicon; Cobalt oxides; Copper nanowires; Multi-walled carbon nanotubes; MXene; Free-standing; Three-dimensional

摘要

随着人们对能量储存技术的需求急剧增大，锂离子电池因其高能量密度，出色的循环性能和环境友好性而被视为最有前途的候选者之一。实际上，市场已经见证了锂离子电池的广泛应用，例如在便携式电子设备中。然而，对于已经广泛商业化的石墨锂离子电池来说，它较低的理论比容量远远不能满足快速增长的市场所产生的巨大需求。因此，开发具有更好循环性和高容量密度的锂离子电池的电极材料变得尤为迫切。

尽管像硅这样的合金嵌锂机制的负极材料具有最高的理论比容量和体积比容量，但是巨大的体积变化以及较低的电子和离子传导率仍然阻碍了它在其他领域的广泛应用，例如大规模储能系统。属于转换嵌锂机制的负极材料也同样面对着类似的挑战。这项工作的重点是采用不同的高导电性材料来改善整个电极的电导率。同时，导电框架的形成有利于容纳活性材料的巨大体积变化。

在第 3 章中，多壁碳纳米管和铜纳米线在铜箔集流器表面上构建了多孔结构，以支撑硅负极。硅沉积在带有铜纳米线和多壁碳纳米管的多孔集流体上，从而形成了纳米级硅材料，最终在本质上减少了活性材料的体积膨胀。同时，由缠结的铜纳米线和多壁碳纳米管形成的大量孔洞进一步适应了由体积变化产生的应力。此外，铜纳米线/硅和多壁碳纳米管/硅的核-壳结构提供了高效的电子和锂离子的扩散途径。结果，我们证明了多壁碳纳米管/铜纳米线/硅的复合电极在 3.5 A g^{-1} 的电流密度下，经过 180 个充放电循环后，电池仍然具有 1845 mAh g^{-1} 的高比容量，且比容量保持为 85.1%。

在第 4 章中，通过冷冻干燥制备三维铜纳米线/硅纳米颗粒@碳的复合材料，开发了一种自支撑的硅基负极。硅纳米颗粒与铜纳米线均匀地附着在一起而碳薄膜涂层也进一步增强了由铜纳米线搭建的三维结构的稳定性。三维导电结构使硅纳米颗粒均匀分布，并增强了整个电极的电子和离子电导率。类似地，由三维结构产生的相当大的间隙可以缓解硅纳米颗粒在充放电过程中产生巨大体积膨胀所导致的应力。同时，碳薄膜外壳对应力也起到了抑制作用。此外，碳薄膜外层不仅增强了三维框架的稳定性还增强了铜纳米线和硅纳米颗粒之间的接触。铜纳米线/硅纳米颗粒@碳的复合电极的电化学性测试表明其具有优异的循环性能。

在第 5 章中，介绍了一种新的高导电材料 MXene 纳米片，以提高锂离子电池的电化学性能。在本章中，氧化钴因其可控的，容易的制备方法被选作活性材料。同时，作为锂离子电池的属于转换嵌锂机制的负极材料之一，氧化钴面临着与硅相同的问题。因此，我们研究了在 Ni 泡沫上结合有 MXene 纳米片和氧化钴纳米颗粒的负极。小尺寸的氧化钴纳米颗粒均匀分布在 MXene 纳米片上，从而导致高锂离子和电子传输效率，并防止 MXene 纳米片的重新堆积和氧化钴纳米粒子的巨大体积变化。如第 5 章所示，当电流密度接近 5 C 时，氧化钴/ MXene 复合电极在 1000 次循环后仍保持 307 mAh g^{-1} 的稳定比容量，这表明氧化钴/ MXene 的复合电极是一个有着巨大潜力的高性能的锂离子电池的负极材料。

关键词：锂离子电池；硅；氧化钴；铜纳米线；多壁碳纳米管；二维过渡金属碳氮化物；自支撑；三维

Acknowledgments

During my four years of study, a lot of people have given their kind help to me. The work may not be completed without their strong support. I am very grateful for their always standing by me, which impresses me for the whole life.

Firstly, I would like to give my deepest gratitude to my supervisor Prof. Ce Zhou Zhao, who has given me precious suggestions not only on the research but also about daily life over the past four years. He guided and encouraged me to deal with the difficulties that I meet during the study. I am very grateful for his patient teaching.

I also want to thank my secondary supervisor Dr.Li Yang for her kindly help with my research work. She always spent a lot of time giving suggestions and revising my articles no matter how busy she was.

I would like to thank my other supervisors, Dr. Ivona Z. Mitrovic, Prof. Stephen Taylor, and Prof. Paul R. Chalker for their supporting while I was studying at the University of Liverpool.

Furthermore, I appreciate Dr. Graham Dawson, Dr. Sang Lam, and Dr. Chun Zhao for sharing their experience in both research and Ph.D. studies. They often paid attention to the progress in my work.

In addition, I want to give my sincere gratitude to my senior fellows Dr. Jingjin

Wu, Dr. Yifei Mu, Dr. Qifeng Lu, Dr. Ruize Sun. They shared with me a lot of experience in doing the experiment, analyzing experimental results, writing articles, and so on. They always encouraged me with their similar experience met during the Ph.D. study.

Moreover, I want to thank my research group members: Mr. Chenguang Liu, Mr. Ruowei Yi, Ms. Yi Sun, Ms. Yudan Yuan, Ms. Miao Cui, Mr. Yutao Cai, Mr. Yuxiao Fang, Mr. Xiangfei Lin and Mr. Xianwei Geng, Ms. Yanfei Qi, Mr. Zongjie Shen, Mr. Qihan Liu, and Mr. Tianshi Zhao. They are my friends as well as the copartners. We often discussed the experimental section, the experimental results, as well as the articles. The precious suggestions they gave me made a great help in my research work.

Last but not least, I need to give special thanks to my parents for their unconditional love and trust. They always stood with me, which gave me high power to complete a four-year Ph.D. study. I am very profoundly moved for their silent support and care. I want to express my heartfelt acknowledgment of all they gave me.

Yinchao Zhao

Jan. 2020

List of Publications

Journal Articles

[1] **Yinchao Zhao**, Chenguang Liu, Yi Sun, Ruowei Yi, Yutao Cai, Yinqing Li, Ivona Mitrovic, Stephen Taylor, Paul Chalker, Li Yang, and Ce Zhou Zhao. "3D-Structured Multi-Walled Carbon Nanotubes/Copper Nanowires Composite as a Porous Current Collector for the Enhanced Silicon-Based Anode." *Journal of Alloys and Compounds*, 803: 505-13, 2019

[2] **Yinchao Zhao**, Chenguang Liu, Ruowei Yi, Ziqian Li, Yanbing Chen, Yinqing Li, Ivona Mitroviz, Stephen Taylor, Paul Chalker, Li Yang, and Ce Zhou Zhao. "Facile Preparation of Co_3O_4 Nanoparticles Incorporating with Highly Conductive MXene Nanosheets as High-Performance Anodes for Lithium-Ion Batteries." *Electrochimica Acta*, 345: 136203, 2020

[3] Chenguang Liu, **Yinchao Zhao**, Ruowei Yi, Yi Sun, Yinqing Li, Li Yang, Ivona Mitrovic, Stephen Taylor, Paul Chalker, and Ce Zhou Zhao. "Alloyed Cu/Si Core-Shell Nanoflowers on the Three-Dimensional Graphene Foam as an Anode for Lithium-Ion Batteries." *Electrochimica Acta*, 306: 45-53, 2019

[4] Chenguang Liu, **Yinchao Zhao**, Ruowei Yi, Hao Wu, Wenbin Yang, Yinqing Li, Ivona Mitrovic, Stephen Taylor, Paul Chalker, Li Yang, and Ce Zhou Zhao. "Enhanced Electrochemical Performance by GeOx-Coated MXene Nanosheet Anode with Hydrophilia Lithium Polyacrylate Binder in Lithium-ion Batteries" Electrochimica Acta, under review.

[5] Jingjin Wu, **Yinchao Zhao**, Ce Zhou Zhao, Li Yang, Qifeng Lu, Qian Zhang, Jeremy Smith, and Yongming Zhao. "Effects of Rapid Thermal Annealing on the Structural, Electrical, and Optical Properties of Zr-Doped ZnO Thin Films Grown by Atomic Layer Deposition." *Materials*, 9(8): 695, 2016

[6] Ruowei Yi, Chenguang Liu, **Yinchao Zhao**, Laurence J. Hardwick, Yinqing Li, Xianwei Geng, Qian Zhang, Li Yang, and Ce Zhou Zhao. "A Light-Weight Free-Standing Graphene Foam-Based Interlayer Towards Improved Li-S Cells." *Electrochimica Acta*, 299: 479-88, 2019

[7] Ruowei Yi, Xiangfei Lin, **Yinchao Zhao**, Chenguang Liu, Yinqing Li, Laurence J. Hardwick, Li Yang, Cezhou Zhao, Xianwei Geng, and Qian Zhang. "Fabrication of a Light-Weight Dual-Function Modified Separator Towards High-Performance Lithium-Sulfur Batteries." *ChemElectroChem*, 6: 3648-56, 2019

[8] Qifeng Lu, Yifei Mu, **Yinchao Zhao**, Ce Zhou Zhao, Li Yang, Stephen Taylor, and Paul Chalker. “Investigation of the electrical performance of hfo_2 dielectrics deposited on passivated germanium substrates.” *Materials Science and Engineering*, 201, 2017

[9] Yudan Yuan, Ruowei Yi, Yi Sun, Jianqiao Zeng, Jiaqi Li, Jiahao Hu, **Yinchao Zhao**, Wei Sun, Chun Zhao, Li Yang, and Ce Zhou Zhao. “Porous Activated Carbons Derived from Pleurotus eryngii for Supercapacitor Applications.” *Journal of Nanomaterials*, 2018:1-10, 2018

[10] Xianwei Geng, Ruowei Yi, Zhiming Yu, Cezhou Zhao, Yinqing Li, Qiuping Wei, Chenguang Liu, **Yinchao Zhao**, Bing Lu, and Li Yang. "Isothermal Sulfur Condensation into Carbon Nanotube/Nitrogen-Doped Graphene Composite for High Performance Lithium–Sulfur Batteries." *Journal of Materials Science: Materials in Electronics*, 29: 10071-81, 2018

Conference Papers

[1] **Yinchao Zhao**, Chenguang Liu, Ruowei Yi, Yi Sun, Li Yang, and Ce Zhou Zhao. "3D Copper Sponges-Supported Si Hollow Nanowires as Advanced Anode Materials for Lithium-Ion Battery." *2nd International Conference on Green Energy and Environment Engineering (CGEEE)*, 2019

[2] Chenguang Liu, **Yinchao Zhao**, Ran Shi, Ruowei Yi, Yi Sun, Li Yang, and Ce Zhou Zhao. "In-situ measurement of stress evolution and pulverization in a composite silicon electrode by high frequency capacitance characterization." *2nd International Conference on Green Energy and Environment Engineering* (CGEEE), 2019,

[3] Yi Sun, Chenguang Liu, **Yinchao Zhao**, Ruowei Yi, Li Yang, and Ce Zhou Zhao. "Graphene oxides mixed in hierarchical porous polyacrylonitrile-based carbons for supercapacitor electrodes." *2nd International Conference on Green Energy and Environment Engineering (CGEEE)*, 2019

[4] Ruowei Yi, Xiangfei Lin, **Yinchao Zhao**, Chenguang Liu, Yinqing Li, Laurence J. Hardwick, Li Yang, Ce Zhou Zhao, Xianwei Geng, Qian Zhang. "A Light-weight Dual-functional Modified Separator via Facile Fabrication towards High Performance Li-S Batteries." *2nd International Conference on Green Energy and Environment Engineering (CGEEE)*, 2019

[5] Qifeng Lu, Sang Lam, Yifei Mu, Ce Zhou Zhao, **Yinchao Zhao**, Yuxiao Fang, Li Yang, Stephen Taylor, and Paul Chalker. "Atomic layer deposition of HfO_2 gate dielectric with surface treatments and post-metallization annealing for germanium MOSFETs." *IEEE 17th International Conference on Nanotechnology (IEEE-NANO)*, 2017

[6] Yudan Yuan, Ruowei Yi, Yi Sun, Jianqiao Zeng, Jiaqi Li, Jiahao Hu, **Yinchao Zhao**, Wei Sun, Chun Zhao, Li Yang, and Ce Zhou Zhao. "Facile Fabrication of Porous

Carbon Materials Derived from Pleurotus Eryngii for Supercapacitor Electrodes.” *IEEE International Conference on Electron Devices and Solid State Circuits (EDSSC)*, 2018

Patents

[1] **Yinchao Zhao**, Zitan Chen, Chenguang Liu, Ruowei Yi, Li Yang, and Ce Zhou Zhao, *Wrapped silicon negative electrode material and preparation method*, Patent Application No.: CN 108039461 A

[2] **Yinchao Zhao**, Chenguang Liu, Liquan Pi, Ruowei Yi, Li Yang, and Ce Zhou Zhao, *Preparation method for copper-silicon compound cathode piece, and application*. Patent Application No.: CN 109560256 A

[3] **Yinchao Zhao**, Chenguang Liu, Haowei Song, Ruowei Yi, Li Yang, and Ce Zhou Zhao, *Preparation method and application of copper carbon silicon composite negative electrode plate*, Patent Application No.: CN 109638224 A

[4] Chenguang Liu, **Yinchao Zhao**, Ruowei Yi, Li Yang, and Ce Zhou Zhao, *Graphene-based nanoflower-shaped silicon-copper alloy electrode material, and preparation method and application*, Patent Application No.: CN 109599534 A

[5] Chenguang Liu, **Yinchao Zhao**, Ruowei Yi, Li Yang, and Ce Zhou Zhao, *Lithium-ion battery electrode stress in-situ measurement system*, Patent Application No.: CN 109671996 A

[6] Chenguang Liu, Minxue Gu, **Yinchao Zhao**, Ruowei Yi, Li Yang, and Ce Zhou Zhao, *Self-assembly-based graphene-silicon composite electrode material and preparation method*, Patent Application No.: CN 108023070 A

[7] Yudan Yuan, Jianqiao Zeng, Yi Sun, **Yinchao Zhao**, Wei Sun, Li Yang, and Ce Zhou Zhao, *Preparation method of carbon-based composite material for supercapacitor*, Patent No.: CN 108039288 A

[8] Ruowei Yi, Li Yang, Ce Zhou Zhao, **Yinchao Zhao**, Chenguang Liu, and Xianwei Geng, *Three-dimensional dendritic nitrogen-doped graphene nanotube and preparation method*, Patent Application No.: CN 108039460 A

[9] Yudan Yuan, Ruowei Yi, Jiaqi Li, Yi Sun, **Yinchao Zhao**, Chenguang Liu, Wei Sun, Chun Zhao, Li Yang, and Ce Zhou Zhao, *Preparation method of polyacrylonitrile/molybdenum disulfide composite material applied to super capacitor*, Patent Application No.: CN 108305789 A

[10] Li Yang, Ce Zhou Zhao, Ruowei Yi, Chenguang Liu, **Yinchao Zhao**, and Xianwei Geng, *Positive electrode material of one-dimensional sulfur-conductive high polymer lithium-sulfur battery and preparation method*, Patent Application No.: CN 107863523 A

[11] Ruowei Yi, Li Yang, Ce Zhou Zhao, Chenguang Liu, **Yinchao Zhao**, and Xianwei Geng, *Lithium-sulfur battery taking nitrogen-doped foamy graphene sheet as middle layer, and preparation method*, Patent Application No.: CN 107887557 A

[12] Ruowei Yi, Li Yang, Ce Zhou Zhao, Chenguang Liu, **Yinchao Zhao**, and Xianwei Geng, *Method for manufacturing intermediate layer of conductive high polymer compound for lithium-sulfur batteries*, Patent Application No.: CN 108039462 A

[13] Ruowei Yi, Li Yang, Ce Zhou Zhao, Yudan Yuan, Chenguang Liu, **Yinchao Zhao**, and Xiangfei Lin, *Composite cathode sheet for lithium-sulfur battery and preparation method*, and application, Patent Application No.: CN 109671907 A

[14] Ruowei Yi, Li Yang, Ce Zhou Zhao, Yudan Yuan, Chenguang Liu, **Yinchao Zhao**, Xianwei Geng, and Xiangfei Lin, *Composite diaphragm for lithium-sulfur battery and preparation method and application*, Patent Application No.: CN 109686902 A

List of Figures

List of Tables

Table of Content

List of Abbreviations and Acronyms

Abbreviations	Completed spelling
1D/2D/3D	one/two/three-dimensional
Al	aluminum
a-Si	amorphous Si
CO_2	carbon dioxide (greenhouse gas)
COMXn	Co_3O_4/MXene composite (mass ratio of Co_3O_4/MXene =n)
Cu NWs	copper nanowires
$CuSO_4 \cdot 5H_2O$	copper sulfate pentahydrate
CV	cyclic voltammetry
DI water	deionized water
DMC	dimethyl carbonate
EC	ethylene carbonate
EDA	ethylenediamine
EDX	energy-dispersive X-ray spectroscopy
EIS	electrochemical impedance spectroscopy
Ge	germanium
HRTEM	high-resolution transmission electron microscopy
IPA	isopropyl alcohol
LIBs	lithium-ion batteries
LiC_6	lithiated graphite
$LiCoO_2$	lithium cobalt oxide
Li-ions/Li^+	lithium-ions
$LiMO_2$	transition metal oxides

$Li\text{-}O_2$	lithium-oxygen
Li-S	lithium-sulfur
LPCVD	low-pressure chemical vapor deposition
MCS	MWCNTs/Cu NWs/Si
MCSn	MWCNTs/Cu NWs/Si (MWCNTs: Cu NWs = 1:n)
MWCNTs	multi-walled carbon nanotubes
MXene	$Ti_3C_2T_x$ (one type of MXene; In the passage, MXene specifically refers to $Ti_3C_2T_x$)
N_2H_4	hydrazine
NaOH	sodium hydroxide
NCA	$Li[Ni_xCo_yAl_z]O_2$
NCM	$Li[Ni_xCo_yMn_z]O_2$
Ni-Cd	nickel-cadmium
Ni-MH	nickel-hydride
NMP	N-Methyl-2-pyrrolidone
OCP	open-circuit potential
PCS	pure Cu NWs/Si (MWCNTs: Cu NWs = 0:1)
Pb-acid	lead-acid
PECVD	plasma-enhanced chemical vapor deposition
PMS	pure MWCNTs/Si (MWCNTs: Cu NWs = 1:0)
PVDF	polyvinylidene fluoride
PVP	polyvinyl pyrrolidone
rpm	revolutions per minute
Sb	antimony
sccm	standard cubic centimeter per minute

SEI	solid-electrolyte interphase
SEM	scanning electron microscopy
Si	silicon
Si NTs	silicon nanotubes
Si NWs	silicon nanowires
SiNPs	silicon nanoparticles
slm	standard liter per minute
Sn	tin
TEM	transmission electron microscopy
XRD	X-ray diffraction

Chapter 1: Literature Review

1.1 Development of energy storage systems

Since industrialization, energy resources always play a critical and irreplaceable role in the development of human society. Energy has been considered as the lifeblood of a country. Nowadays, the world faces two main challenges. Firstly, fossil fuels such as coal, petroleum, and natural gas supply about 85% of the global power consumption, which has done immeasurable and catastrophic effects on the ecological environment and human health [1, 2]. Notably, excess greenhouse gas (e.g., CO_2) emission brings about global warming. The other problem is the limited storage of the unsustainable fossil fuels on earth. Although fossil fuels have been overused, it still cannot satisfy the fast-growing energy demands of the market. Therefore, it seems to be of critical and urgent importance to considerably develop and use environmental-friendly and sustainable energy resources to alleviate the energy crisis and environmental issues.

Recently, the usage of clean and renewable energy resources such as water, geothermal, solar, and wind energy for electricity production has gained a remarkable achievement in the development of energy capture technology such as the dam, geothermal heat pumps, solar cells, and wind turbines [3]. However, the output fluctuating with the environment and the low energy conversion efficiency of the new energy resources lead to the discontinuous and insufficient power supply, indicating the reason why clean energy resources have failed to replace conventional fossil fuel so far

[4] completely. Therefore, it is significant to developing the energy storage system for continuous and stable power supply. For instance, electric vehicles are embedded with batteries instead of internal combustion engines of conventional cars, which implies the transformation from the engine propulsion to electrical propulsion reducing the transportation emission [4, 5]. Hence, energy storage equipment with long-term stability and high energy density plays a significant role in facilitating the development of renewable energy and energy storage systems [6].

In this regard, batteries, which work with the mutual transformation between the chemical energy and electrical energy [7], have attracted considerable attention for its excellent electrochemical performance. Among the rechargeable batteries systems, Nickel-cadmium (Ni-Cd), nickel-hydride (Ni-MH), and lead-acid (Pb-acid) batteries were developed with mature fabrication technology and occupied extensive energy storage market before the lithium-based batteries [8]. However, there is a memory effect occurring with the Ni-Cd and Ni-MH batteries, and Ni-Cd and Pb-acid batteries pose a threat to the environment due to the poisonous metal Cd and Pb. Moreover, taking the application in electric vehicles or portable devices into account, the above batteries are limited for their relatively low energy density and mass density. Therefore, lithium-based batteries have been recognized as the one of the most potential energy storage systems because of their outstanding energy density and high security, such as lithium-sulfur (Li-S), Li metal, lithium-oxygen (Li-O_2), and lithium-ion (Li-ion) batteries [9]. However, the severe problems involving the “shuttle effect” of the polysulfides and uncontrollable lithium dendrites hinder the commercialization of the Li-S batteries [10].

Similarly, the uncontrollable growth of lithium dendrites causes unsatisfied cycling performance and security problems for the Li metal batteries. With respect to the Li-O_2 batteries, the surge of polarization occurs during the oxygen redox reactions results in the low reversibility efficiency and capacity fading over cycling [6]. By contrast with these batteries, lithium-ion batteries (LIBs) have a comparable volumetric and gravimetric energy density, as well as the environmental friendliness and safety. Consequently, LIBs have intense competitiveness in the area of portable electronics and electric vehicles.

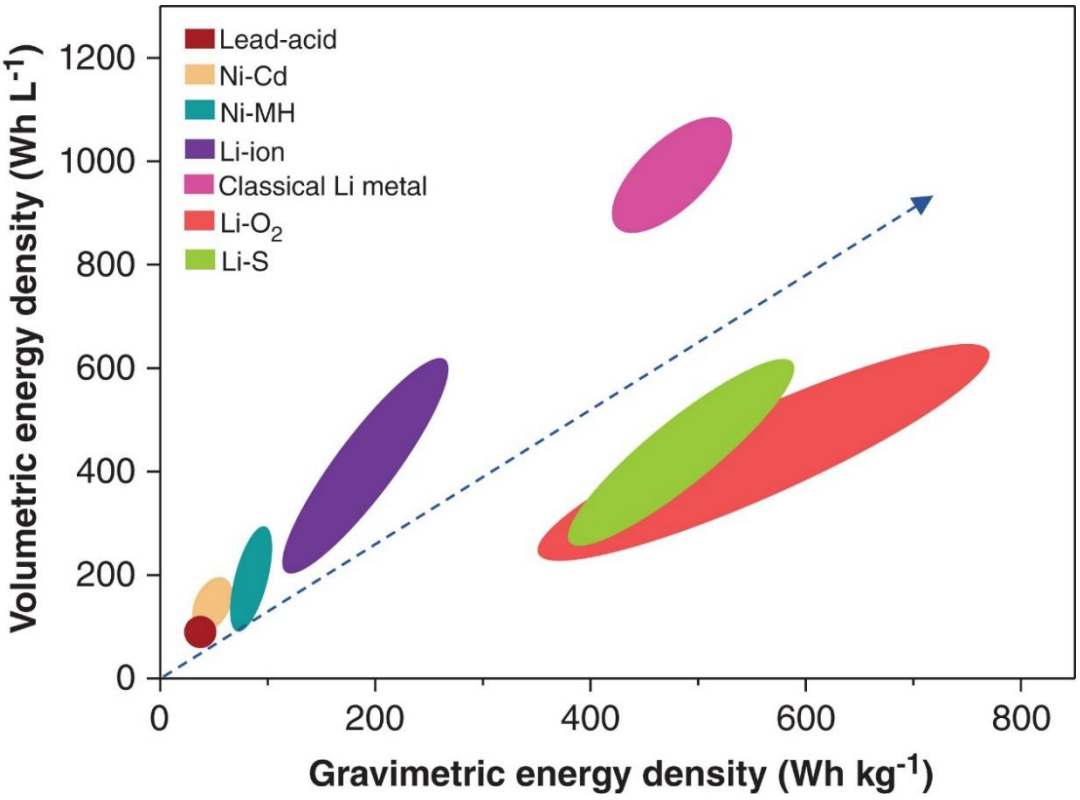

Figure 1.1 Plot of gravimetric energy density vs. volumetric energy density of various rechargeable batteries [11].

1.2 Working principle of lithium-ion batteries

Initially, lithium metal thrusted into the research spotlight for its extraordinarily high specific capacity of 3860 mAh g^{-1}, low density of 0.51 g cm^{-3}, and the lowest reduction potential of -3.04 V (vs. H_2/H^+) [12, 13]. However, over the past 40 years, lithium metal batteries have not come into commercialization, which is mainly ascribed to severe safety issues caused by the growth of Li dendrites and the short cycling lifespan resulting from the modest Coulombic efficiency. The LIBs realized the commercialization at Sony Corporation in 1991, which was developed on the fundamental research results of John Goodenough [14]. During the commercialization, the company employed lithium cobalt oxide ($LiCoO_2$) and lithiated graphite (LiC6) as the cathode and anode in LIBs, respectively [7].

The configuration of a lithium-ion battery consists of shells, separator, electrolyte, cathode, and anode with the typical shapes such as coin, cylindrical, prismatic, and pouch cells, as shown in **Figure 1.2**.

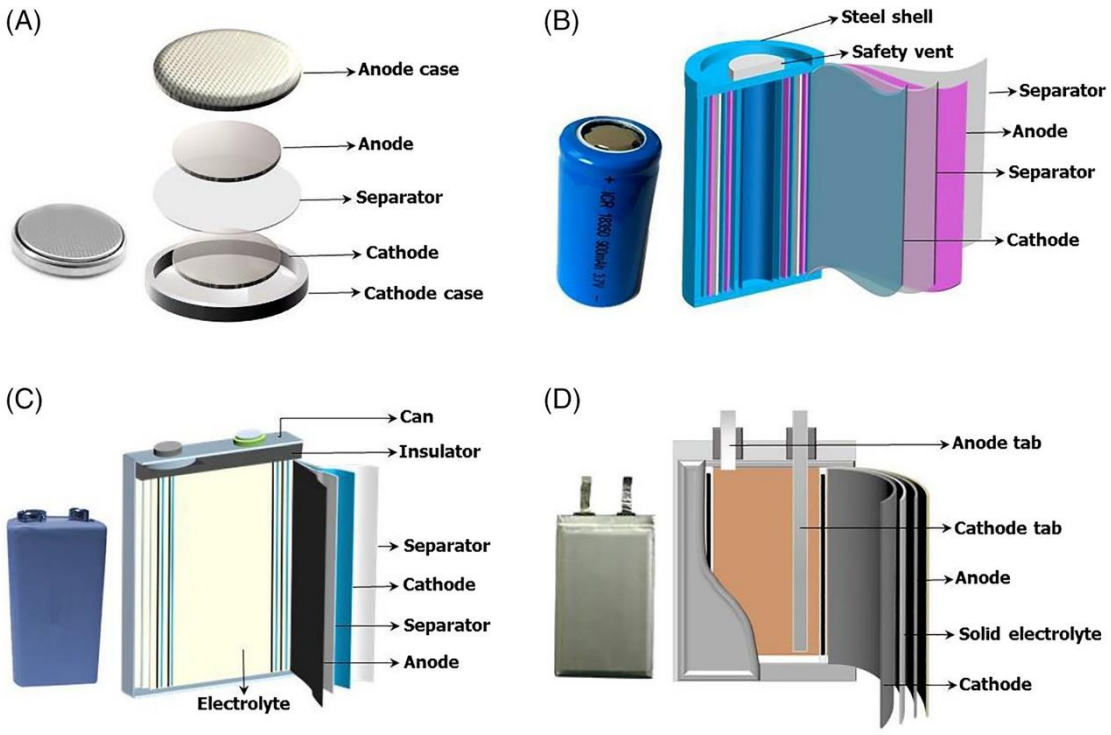

Figure 1.2 Different shapes of Li-ion batteries, including coin, cylindrical, prismatic, and pouch cells [11].

Figure 1.3 illustrates the operating mode of LIBs, where $LiCoO_2$ (left electrode in the figures) and graphite (right electrode in the figures) are cathode and anode materials, respectively, in the schematic diagram. The battery works when the lithium-ions carried by the electrolyte back and forth between cathode and anode through a separator. A battery exhibits an initial state of completely discharged, namely the cathode full of Li-ions (**Figure 1.3a**) [4, 15]. Thus, the battery starts with charging. During the charging process, lithium-ions detach from the cathode ($LiCoO_2$) and are embedded in the interlayer of the anode (graphite). Meanwhile, the electrons transfer in the same direction through the external circuit. Therefore, the current in the external circuit flows from the negative electrode to the positive electrode (**Figure 1.3b**). On the contrary,

during the discharging process, both lithium-ions and electrons migrate in the reversed direction. In this way, the current flows from the positive electrode to the negative electrode with lighting a bulb (**Figure 1.3d**). The corresponding electrochemistry reactions occurring during the intercalation and de-intercalation process are expressed as follows,

Cathode: $LiCoO_2 \rightleftharpoons xLi^+ + xe^- + Li_{1-x}CoO_2$ (1)

Anode: $C_6 + xLi^+ + xe^- \rightleftharpoons Li_xC_6$ (2)

Overall reaction: $LiCoO_2 + 6C \rightleftharpoons Li_xC_6 + Li_{1-x}CoO_2$ (3)

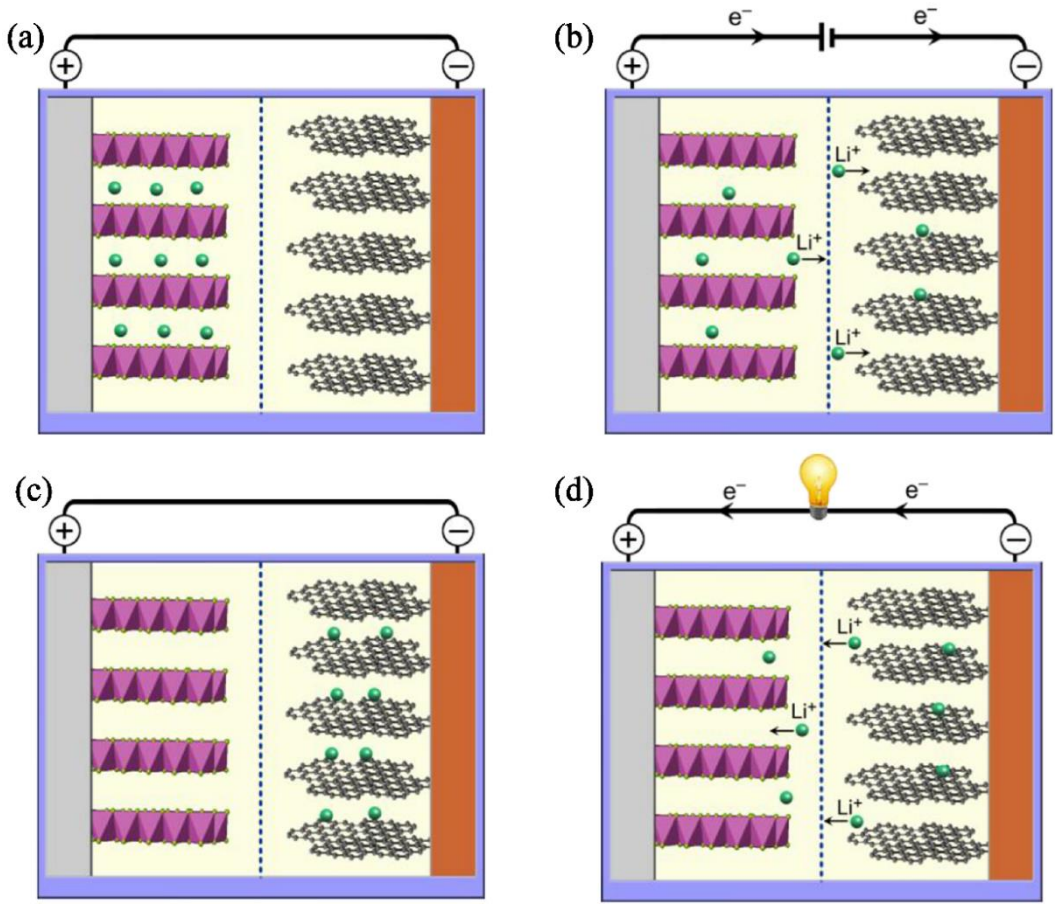

Figure 1.3 Scheme of lithium-ion batteries at the stages of the completely discharged (a), the charging process (b), the completely charged (c), and the discharging process (d) (cathode is $LiCoO_2$ and anode is graphite) [11].

1.3 Cathode materials of lithium-ion batteries

The cathode is taken as one of the critical components in LIBs. Concerning the energy density, he materials with high theoretical specific capacity and working potential, low cost, excellent electrochemical stability, and superior electronic and ionic conductivity could be selected as the cathode for the LIBs [16]. Today, accessible cathode materials can be divided into three categories based on their crystal structures, such as layered, spinel, and olivine.

1.3.1 Layered cathode materials

The layered lithiated transition metal oxides $LiMO_2$ (M=Co, Ni, and Mn) have been widely applied as the cathode in LIBs. **Figure 1.4a** illustrates the layered structure of $LiMO_2$, where the Li-ions intercalate between the interlayers of the MO_6. Although the theoretical capacity is 274 mAh g^{-1}, the practical capacity only achieves half of the theoretical capacity. On the other hand, only half of Li-ions are contrived to escape from the cathode to the anode during the charging process, which is ascribed to the unstable structure of $Li_{1-x}CoO_2$ and considerable irreversible reaction, if x exceeds 0.5. Over the past 30 years, $LiCoO_2$ has dominated the market of rechargeable LIBs for its cycling stability and safety performance [17]. However, the high cost of rare materials Co, low thermal stability, and attenuation in capacity at large current densities on a long-term cycling urge researcher to improve the properties of $LiCoO_2$ or develop the competitive candidates. For instance, cycling performance, rate capability, and intrinsic thermal stability of cathode materials can be enhanced by surface coatings such as carbon and metal oxides [18-20]. The coating layers not only improve the electronic conductivity but also provide a protective layer to prevent Co from dissolving in the electrolyte [21]. In addition, Ni and Mn are used to substitute the Co in $LiMO_2$. However, the complicated synthesis method and the thermal instability hinder the practical application of $LiNiO_2$ and $LiMnO_2$ [22]. Then, Delmasa and his group made impressive progress in synthesis $LiNi_{1-y}Co_yO_2$, in which $LiCoO_2$ and $LiNiO_2$ form a complementary relationship [23]. After that, the electrochemical performance of the cathode can be further enhanced by the new generation layered ternary materials such

as $Li[Ni_xCo_yMn_z]O_2$ (NCM) and $Li[Ni_xCo_yAl_z]O_2$ (NCA) with a higher specific capacity, improved thermal stability, and lower cost [24-26]. The concentration of Ni, Co, and Mn in the cathode materials makes a defining difference in thermal stability, capacity retention, and specific discharge capacity (**Figure 1.5**).

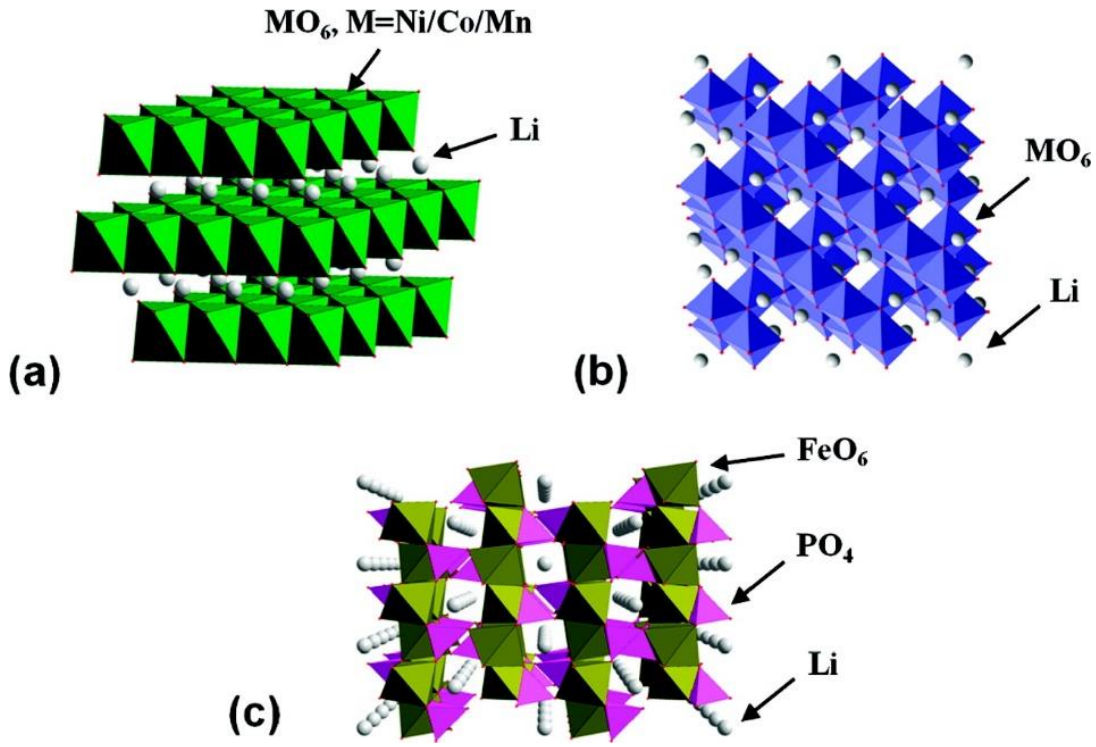

Figure 1.4 Structures of cathode materials: (a) Layered structure ($LiMO_2$, M=Ni/Co/Mn), (b) spinel structure ($LiMn_2O_4$), and (c) olivine structure ($LiFePO_4$) [27].

1.3.2 Spinel cathode materials

Figure 1.4b shows the cathode materials with spinel structure such as $LiMn_2O_4$. Compared with $LiCoO_2$, $LiMn_2O_4$ exhibits higher working potential around 4V, low cost, and stable structure. Besides, it demonstrates that the spinel structure of $LiMn_2O_4$

could provide a highly efficient Li^+ diffusion channel, leading to outstanding rate capability. However, the safety problems may occur when the $LiMn_2O_4$-based LIBs work at the high temperature, which is ascribed to the soluble Mn in the electrolyte, Jahn-Teller distortion induced by large amount of Mn^{3+} in $LiMn_2O_4$[28], and decomposes of the electrolyte.

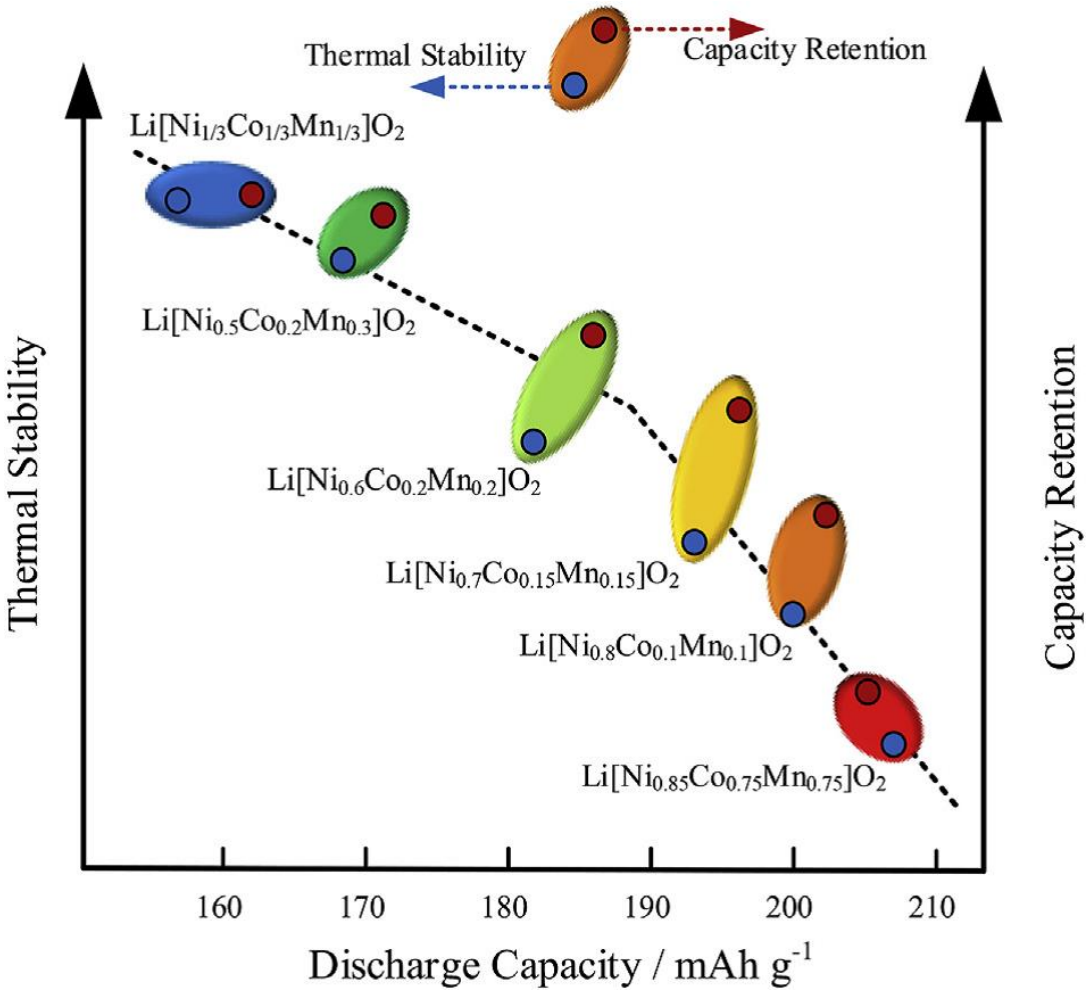

Figure 1.5 The effect of different contents of Ni, Co, and Mn elements in $LiNi_xO_yMn_zO_2$ on thermal stability, specific capacity, and capacity retention [29].

1.3.3 Olivine cathode materials

In **Figure 1.4c**, $LiFePO_4$ is one kind of cathode materials with olivine structure. $LiFePO_4$ has attracted great attention since Goodenough discovered it because of its low cost, excellent electrochemical properties, and non-toxicity [30]. Nevertheless, some noticeable problems include low electronic and ionic conductivity and modest working potential (3.4 V), which leads to poor rate capability and low energy density, respectively. Recently, popular approaches involve size minimization to increase Li^+ diffusion efficiency [31]. Surface coating with conducting materials and meal-ions doping also are effective methods to improve the electronic conductivity [32]. All methods above are beneficial to the rate capability of batteries but at the expense of the production cost. Moreover, as far as improving working voltage is concerned, the transition metal redox such as Co, Mn, and Ni elements could take the place of Fe element [33, 34].

Table 1.1 Summary of the cathode materials with corresponding categories, capacity, working potential, and Li^+ diffusion coefficient [35, 36].

Name	**Structures**	**Theoretical capacity (mAh g^{-1})**	**Actual capacity**	**Working potential (V)**	**Li^+ diffusion coefficient (m^2*S^{-1})**
$LiCoO_2$	layered	274	140	3.7	10^{-12}~10^{-11}
$LiNi_xCo_yMn_zO_2$	layered	275	1	3.5	10^{-11}~10^{-10}
$LiMn_2O_4$	spinel	148	120	4.0	10^{-14}~10^{-12}
$LiFePO_4$	olivine	160	150	3.4	10^{-15}~10^{-12}

1.4 Anode materials of lithium-ion batteries

By contrast with cathode materials, anode materials also play a decisive role in the electrochemical performance of LIBs. Generally, a practical and ideal anode should possess the following characteristics: (1) a low working potential; (2) high gravimetric and volumetric capacity; (3) high Coulombic efficiency; (4) high ionic and electronic conductivity; (5) small volume change during the lithiation/delithiation process; (6) excellent structural stability; (7) low cost, safety, and environmental benignity. These conditions are the criteria for researchers and developers to select suitable anode materials for LIBs.

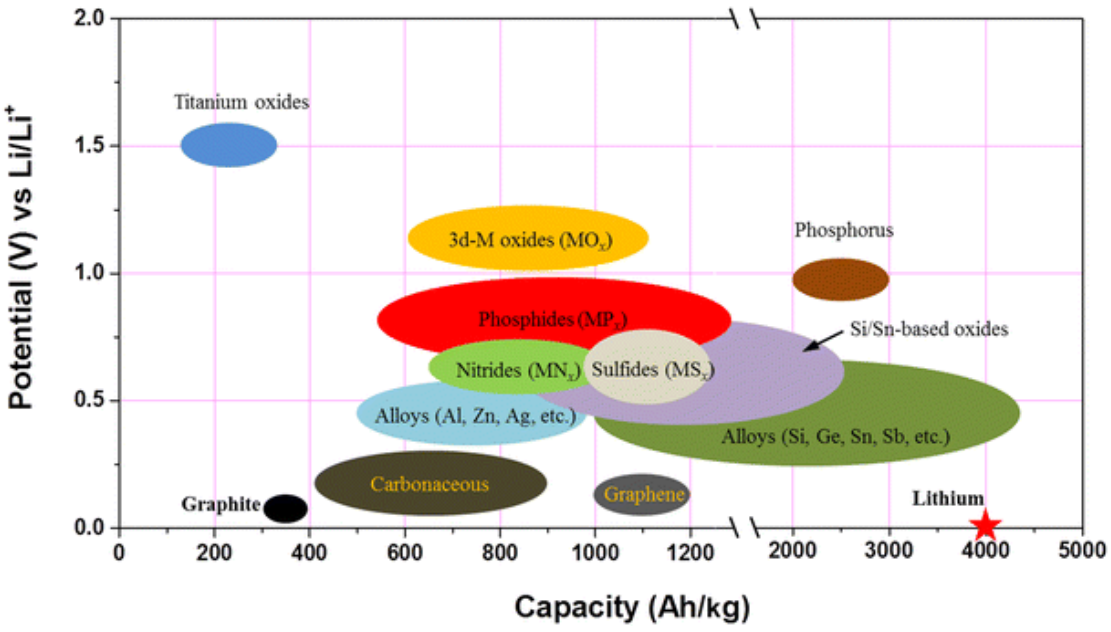

Figure 1.6 Illustration of various anode materials with corresponding working voltage and specific capacity [37].

Figure 1.6 shows the redox potential and the correlated gravimetric capacity of various anode materials. Li metal has a huge advantage in both specific capacity

(3860 mAh g^{-1}) and working potential (0 V versus Li^+/Li). Unfortunately, the severe safety problems associated with the internal short circuit resulting from the uncontrollable growth of the lithium dendrites limit the widely practical application in LIBs. Therefore, the upsurging demand for LIBs with high energy density and cycling stability urges people to develop more advanced anode materials, e.g., graphite, semiconductor, or transition metal oxides, as shown in **Figure 1.6**. All the anode materials can be classified into three categories corresponding to their lithiation and delithiation mechanisms, namely intercalation, alloy, and conversion, as displayed in **Figure 1.7** [38].

Table 1.2 Summary of the anode materials with relevant properties [38-42].

Anode material	**Lithiated phase**	**Theoretical specific capacity (mAh g^{-1})**	**Theoretical charge density (mAh cm^{-3})**	**Working potential (V)**	**Volume variation (%)**
Li	Li	3862	2047	0	100
C	LiC_6	372	837	0.05	12
$Li_4Ti_5O_{12}$	$Li_7Ti_5O_{12}$	175	613	1.55	1
TiO_2	$Li_{0.5}TiO_2$	335	1280	0.8	<4
Si	$Li_{4.4}Si$	4200	9786	0.4	420
Sn	$Li_{4.4}Sn$	994	7246	0.6	260
Ge	$Li_{4.4}Ge$	1625	7367	0.5	272
Sb	Li_3Sb	660	4422	0.9	200

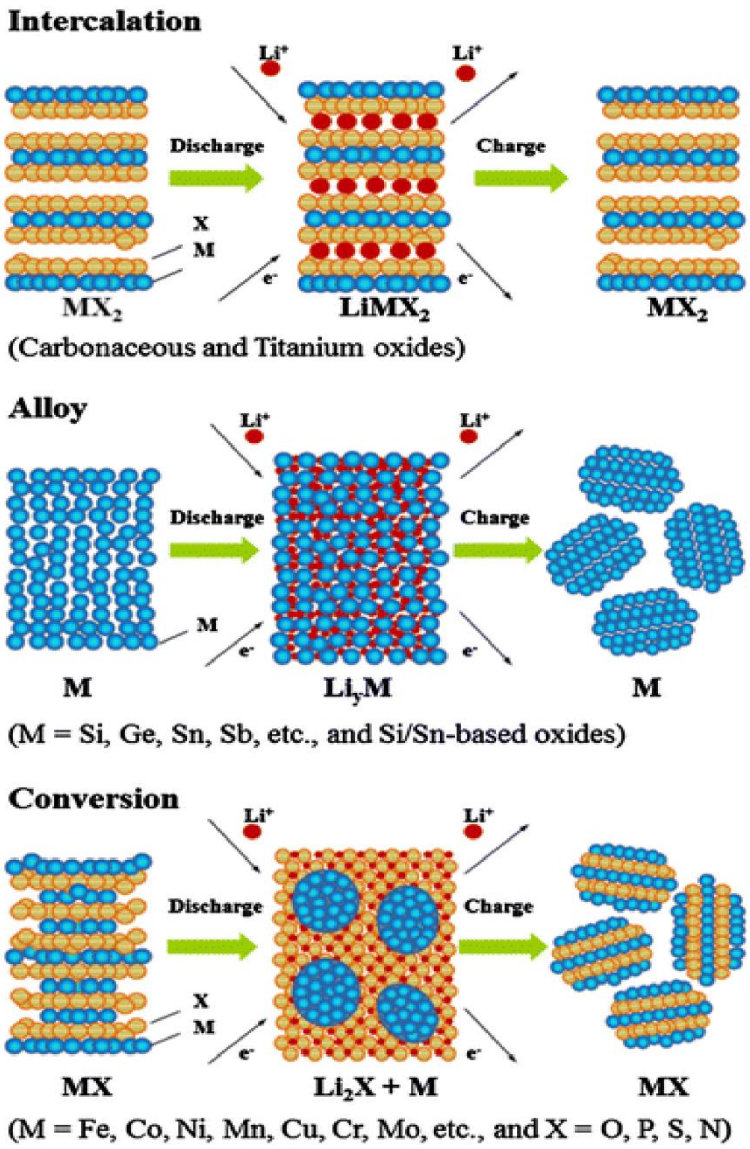

Figure 1.7 Three categories of lithiation and delithiation mechanisms for different anode materials [39].

1.4.1 Intercalation mechanism

Generally, carbon-based and titanium-based anode materials abide by the intercalation mechanism [40]. Commonly, these materials have large interlayer spacing or lattice spacing, which is beneficial for the insertion and extraction of Li^+ between the interlayers or within the lattice framework, respectively [41]. According to the

intercalation mechanism, the amount of Li-ions inserted into the anode is limited. On the other hand, there is little volume change occurring in the anode materials during the charge/discharge procedure. Therefore, these anode materials possess relatively low specific capacity but high capacity retention and excellent cycling performance.

1.4.1.1 Carbon-based anode materials

For instance, graphite, one of the carbon-based materials, has been put into highly commercial production due to its safety, stability, low cost, and small working potential (0.05 V) [42]. Typically, every six carbon atoms encompass one Li atom, as described by Equation (2). In this case, the theoretical specific capacity of graphite is restricted to 372 mAh g^{-1}.

Graphene, one atomic sheet of graphite, is extremely attractive due to its large specific surface area (2630 m^2 g^{-1}), excellent conductivity (~15000 cm^2 V^{-1} s^{-1}), and thermal conductivity (5300 W m^{-1} K^{-1}) [43, 44]. However, there are several limitations for graphene to become an ideal anode material in LIBs. Firstly, a lot of functional groups on the surface of graphene negatively affect the conductivity. Furthermore, the van der Waals force will cause the graphene layers to stack up, which hinders Li-ions transporting in the anode materials. Therefore, researchers prefer to combine graphene with other active materials as a composite anode for LIBs.

1.4.1.2 Titanium-based anode materials

Titanium-based anode materials (e.g., TiO_2 and $Li_4Ti_5O_{12}$) follow the intercalation mechanism. Nevertheless, the capacity depends on the crystallinity, particle size, structure, and surface area rather than the interlayer spacing (Equation (4) and (5)) [45]. TiO_2 and $Li_4Ti_5O_{12}$ exhibit the theoretical capacity of 167 and 175 mAh g^{-1} [46], respectively, which is inferior to the carbon-based anode materials. Besides, titanium-based anode materials have no superiority in electronic conductivity (10^{-12}~10^{-13} S cm^{-1}). In terms of operating potential, TiO_2 and $Li_4Ti_5O_{12}$ are 0.8 and 1.55 V (versus Li^+/Li), exceeding that of the carbon-based anode leading to a smaller output voltage. However, the stable working potential results in extremely high safety performance and prolonged cycling life.

$$Li_4Ti_5O_{12} + 3Li^+ + 3e^- \rightleftharpoons Li_7Ti_5O_{12} \qquad (4)$$

$$TiO_2 + xLi^+ + xe^- \rightleftharpoons Li_xTiO_2 \qquad (5)$$

Further research work to enhance the electrochemical performance of titanium-based LIBs focuses on structural transformation and modification by other conductive materials. For example, titanium-based materials contrived into nanotubes and nanoparticles exhibit excellent cycling performance [47, 48]. Moreover, TiO_2 and $Li_4Ti_5O_{12}$ can deliver higher capacity and superior rate performance by doping highly conductive materials like Sb [49], Br [50], and Ag [51] or being encapsulated by carbon [52, 53].

1.4.2 Alloy/de-alloy mechanism

Over the past twenty years, the alloy/de-alloy anodes have attracted considerable attention for their distinguished theoretical specific capacities that are 2-20 times larger than that of intercalation materials, which is attributed to the alloy/de-alloy mechanism. During the lithiation process, the anode M together with the Li^+ diffusing from the cathode form the lithium alloy Li_xM, as expressed by Equation (6). During the delithiation process, the alloy Li_xM oxidizes, while Li-ions release from the anode and move to the cathode through the electrolyte.

$$M + xLi^+ + xe^- \rightleftharpoons Li_xM \qquad (6)$$

Anode materials M complying with the alloying/de-alloying mechanism contain group IV and V elements such as silicon (Si), germanium (Ge), tin (Sn), antimony (Sb), aluminum (Al) as well as the relative metal oxides like SiO, SnO_2, and SnO_2. Here, Si is taken as an example for explanation. Concerning Si, one Si atoms, on average, accommodate 4.4 Li atoms to form the Li-Si alloy ($Li_{22}Si_5$) [54]. Hence, among the various anode materials, Si possesses the highest theoretical gravimetric capacity of 4200 mAh g^{-1} and a volumetric capacity of 9786 mAh cm^{-3} [55].

Apart from the high theoretical capacity, the alloy anodes have advantages in suitable delithiation voltage. For example, the delithiation voltages of Mg, Al, and Si locate at 0.1 V, 0.3 V, and 0.4 V with reference to Li^+/Li, respectively, which is very close to that of graphite and lower than most anode materials. The suitable working

potential promises a high energy density of LIBs. Meanwhile, it is not easy for Li-ions to escape from Si anode and form dangerous lithium dendritic crystal. It is worth noting that most alloy materials are equipped with high electrical conductivity, such as Ge that is 10^4 times larger than Si (10^{-3} S cm^{-1}) [56]. As far as Si is concerned, the electrical conductivity is a deficiency in contrast with other alloy materials. Furthermore, the reserves of various anode materials on the earth cause the unequal production cost. Especially, the storage of silicon ranks second in the world and is friendly to the environment. By comparison, the cost of using Ge as an anode for LIBs is more expensive than Si.

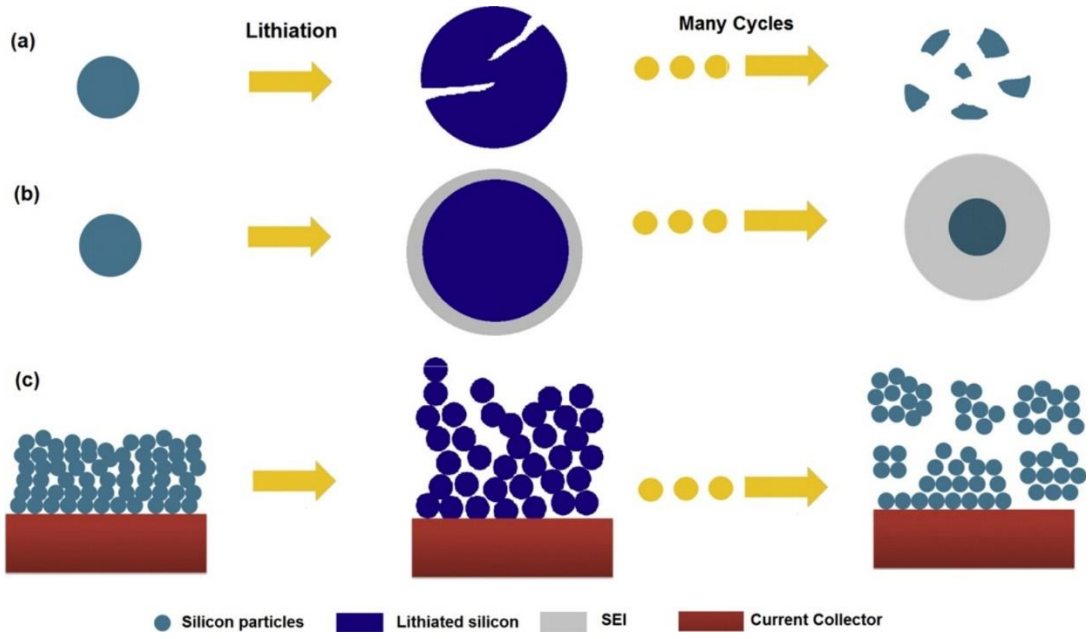

Figure 1.8 Challenges for Si-based anode: (a) Material pulverization; (b) Uncontrollable growth of SEI layers; (c) The detachment between active materials and current collector [57].

Although alloy anodes possess remarkable advantages compared with the intercalation anodes, there are still some barriers that hinder their mature commercialization. Firstly, the considerable volume expansion during lithiation and delithiation cycling processes leads to cracking and pulverization on the alloy anodes, as shown in **Figure 1.8a and Figure 1.8c** [58]. Among the alloys materials, Al has a relatively low volume expansion that is actually 96 times larger than that of the titanium (1%). More interesting, Si will expand and contract by 400% during the charging and discharging processes, which is ascribed to the large capacity of Li-ions [59]. The vast volume change eventually causes the cracking and pulverization of materials over long-term cycles, as well as the separation between the active materials and the detachment between active materials and current collectors [60]. It indicates that alloy anodes undergo the fading in the capacity over long-term charging/discharging cycling.

Alloy anodes must face another challenge of the unstable growth of the solid-electrolyte interphase (SEI). The SEI layer, locating the interface between active materials and the electrolyte, consists of the decomposition products of the organic electrolyte. If the voltage is lower than 1 V with respect to Li^+/Li, the organic electrolyte will decompose at the surface of anode materials and generate the SEI layers [57]. Since SEI films are ionically conducting and electronically insulating, it could prevent the excessive formation of SEI films on the surface of anodes. However, the massive volume expansion of Si anode at lithiation state damages SEI films, as illustrated in **Figure 1.8b**. In this circumstance, the bare surface of active materials recontacts the electrolyte companying by the generation of SEI layers. As a consequence, the SEI

layers become thicker and thicker during the lithiation and delithiation cycling processes at the expense of the Li-ions in the electrolyte and electrical conductivity of the electrode. Additionally, the increased thickness of SEI films is equivalent to the extended Li^+ diffusion distance, implying a lower diffusion efficiency of Li-ions.

To solve these issues, one simplified approach is to contrive the nanostructured Si materials to accommodate the considerable volume change, such as silicon nanoparticles (Si NPs) [61], silicon nanowires (Si NWs) [62], and silicon nanotubes (Si NTs) [63]. Except that, the outer shell is widely used to not only restrict the massive volume expansion but also stabilize the formation of SEI layers. For instance, Cui *et al.* constructed the silicon particles sheathed by amorphous titanium oxide (Si@a-TiO_2) core-shell structure as an anode [64]. The self-healing a-TiO_2 film plays the role of an artificial SEI, which attenuates the expansion of silicon and reinforces the anode with excellent Coulombic efficiency. However, the electrochemical performance of Si@a-TiO_2 at high current density is unsatisfied due to low Li^+ diffusion efficiency and inferior electrical conductivity. It is necessary to apply highly conductive materials in the anode to improve the rate performance of the LIBs.

1.4.3 Conversion mechanism

The conversion mechanism could be manifested by the following Equation (7).

$$M_xN_y + zLi^+ + ze^- \rightleftharpoons xM + Li_zN_y \qquad (7)$$

M represents metal elements such as Fe, Co, Mn, Ni, and Cu, while N refers to O,

P, S, N, and Sb elements [37, 65]. It is found that transition metal compounds follow the conversion mechanism when they act as the anode in LIBs, including oxides, phosphides, sulfides, and nitrides. The reversible lithiation and delithiation processes involve the generation and decomposition of lithium compounds (Li_zN_y) and the corresponding oxidation and reduction of transition metal oxides (M_xN_y). The conversion anode materials exhibit excellent theoretical capacity ranging from 500-1800 mAh g^{-1} [38, 66] that considerably exceeds that of intercalation anode materials. Moreover, the working potential is commonly larger than 0.5V (vs. Li^+/Li), resulting in LIBs with more safe performance than the commercialized graphite-based batteries. Furthermore, the preparation for conversion materials is facile and controllable. Even though these advantages make the conversion anode materials strong competitive with the intercalation or alloy anode materials, some intrinsic issues should be solved to enhance their electrochemical performance.

Similar to alloy materials, the conversion materials, especially metal transition oxides, suffer huge volume expansion during lithiation and delithiation processes. Besides, the poor electrical conductivity and serious voltage lag phenomena impede the transition metal oxide becoming an ideal anode in LIBs [67].

Therefore, to address these challenges, researchers often put forward the strategies in respect of restructuring conversion materials into nanoscale and compounding them with other complementary materials. Here, take cobalt oxides (Co_3O_4) as an example. The double metal oxides, such as $NiCo_2O_4$ and $ZnCo_2O_4$, were applied to relieve the

volume expansion and increase electrical conductivity [68, 69]. Normally, the complemental materials involve carbon nanotube, graphene, and metal materials that feature high electrical conductivity and strong mechanical strength. Prof. Cheng and his research group designed an anode with Co_3O_4 anchored on graphene, which displayed excellent electrochemical performance with superior reversible capacity and excellent cycling stability and rate capability [70]. Li and co-workers also synthesized porous Co_3O_4 sheets on graphene foams, which exhibited excellent flexibility and mechanical strength with a high specific capacity of 790 mAh g^{-1} after 100 cycles at a current density of 0.1 C [71].

1.5 Highly conductive materials introduced in anodes

The main challenges for the alloy materials and conversion materials involve the huge volume expansion and low electrical conductivity. Therefore, the methods to tackle these problems are almost identical. For example, most active materials are constructed into nanoscale to relieve the stress from the volume expansion. On the other hand, highly conductive materials are introduced to improve the electrical conductivity of the entire electrode, including metal, carbon, and so on.

1.5.1 Metal materials

Although the employment of metal materials will increase the production cost of the Li-ion batteries, the improvement in electrical conductivity by using metal materials is considerable. The recent strategy to tackle this challenge is to prepare active materials

directly on the conductive substrates such as copper foam [72, 73], nickel foam [74], carbon cloth [75, 76], and so on. A three-dimensional (3D) conductive network not only improves the electrical conductivity by providing the fast transport paths for electron and ions but also provides an excellent cycling life span by accommodating the volume expansion of active materials and anchoring them from falling off the substrate [77]. Hongxiang Wang and co-workers combined the Cu/amorphous Si (a-Si) core-shell nanowires with the flexible copper foam as a binder-free anode used in LIBs. The anode showed an excellent stable performance with only 0.03 % average capacity loss per cycle at 1 A g^{-1} after 1000 cycles [78]. It is noted that the core-shell nanowires structure has been increasingly developed to further ameliorate the electrochemical performance of Si-based LIBs, such as Cu-Si [73, 79, 80] and Sn-Si [81] featuring conductive metal as the core part. Zhang's group directly deposited Si film on Cu NWs anchored on a porous nickel foam and subsequently coated the Cu/Si core-shell nanowires with Ge films [82]. After 3000 cycles, Cu/Si/Ge composite retained a high specific capacity of 1523 mAh g^{-1} at a particular current density of 1 A g^{-1}. These previous studies indicate that the electrochemical performance of Si-based anodes could be improved by constructing the metal/Si core-shell structure on a porous and flexible substrate.

1.5.2 Carbon-based materials

Carbon such as graphene and carbon nanotube is used to encapsulate nanostructured Si, as shown in **Figure 1.9**. The application of carbon nanotube prevents the pulverization of active materials. Yu's group reported a porous custard-apple-like Si@C structure, which maintains an excellent reversible capacity of 900 mAh g^{-1} at high current density (2 A g^{-1}) with a long cycling life of over 4000 cycles [83]. Besides, Kung's group combined the Si with graphene as an anode for LIBs with the improved electrochemical performance [84]. The carbon nanotube and graphene involved in the anode could restrain the considerable volume changes. More importantly, the poor conductivity of the electrode is enhanced with highly efficient electrons and Li^+ diffusion pathways. It is worth noting that two-dimensional (2D) graphene functions as the flexible support for uniform distribution of nanosized active materials will further relieve the stress caused by volume expansion.

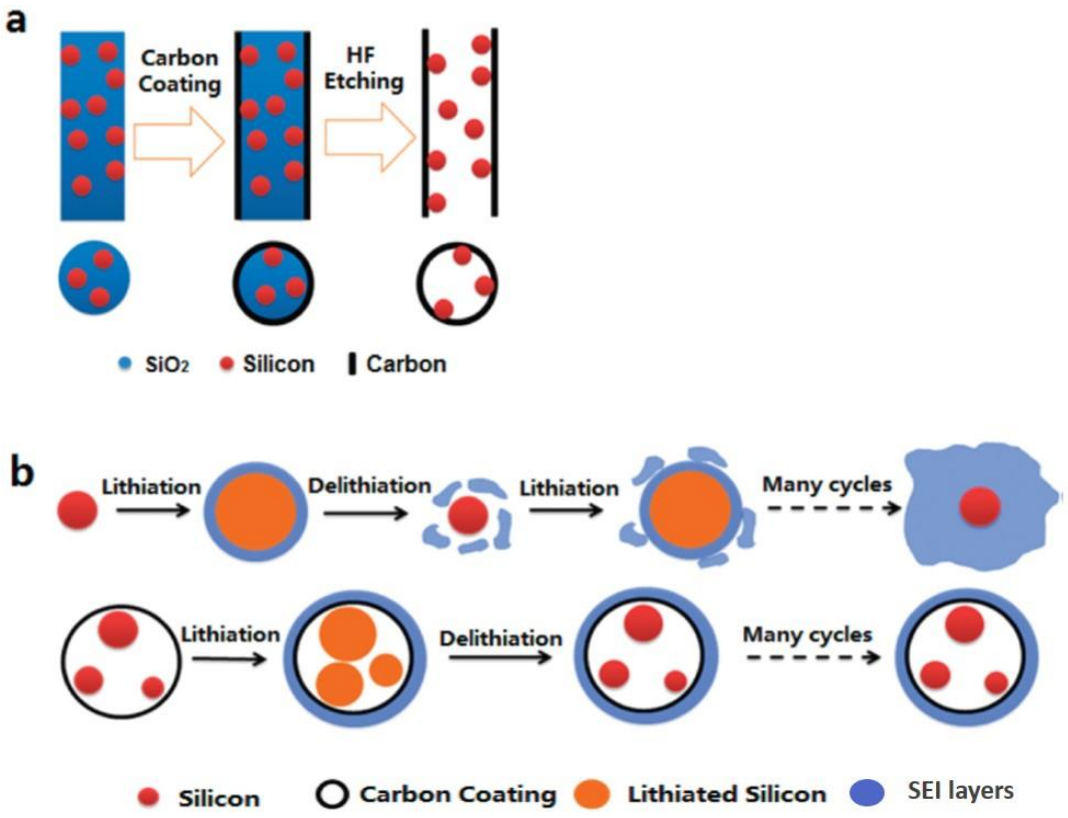

Figure 1.9 (a) Scheme of synthesizing the Si NPs@CNTs. (b) The controllable growth of SEI layers on the Si NPs@CNTs electrode [85].

1.5.3 Two dimensional MXene

Recently, there is considerable scientific interest in the newly available family of MXenes materials. An analog as graphene, this 2D layered material with the structure of transition metal carbides, or nitrides exhibits superior electronic conductivity, large interlayer spacing for highly efficient Li^+ diffusion pathways, and environmental benignity, making it useful as energy storage materials [86]. Gogotsi et al. discovered a novel 2D transition-metal carbide $Ti_3C_2T_x$ (one type of MXene), where T represents the functional groups (-OH, -F, and -O) on the surface. They applied it in transparent and flexible energy storage [87-89]. Their MXene was obtained by removing a group

element (IIIA or IVA) layer using HF from the original MAX phases [90]. M is a transition metal and A is a group 13 or 14 elements of the periodic table. X is C or N. After etching, the MXene was delaminated into few layers leaving large intercalation spacing to enhance Li^+ diffusion. Long-term cycling stability and excellent rate capability were demonstrated by numerous excellent work [91, 92]. However, due to their ordinary theoretical capacity of 126.4 mAh g^{-1} at 1 C [93], the challenges remain for their practical applications of energy storage in the near future.

In this way, researchers focus on integrating MXene with the active materials to improve the electrochemical performance of LIBs. Zhang *et al*. employed MXene as a matrix to support amorphous Si as anode for LIBs, which exhibited a high specific capacity of 557 mAh g^{-1} after 500 cycles at the current density 1 C of and excellent cycling stability [94]. Moreover, Zhang *et al.* reported a sandwich-like structured Sn/SnO_2/MXene composite as an anode that achieved impressive progress in the electrochemical performance of LIBs [95].

1.6 Objectives

To satisfy the increasing demand for reliable energy storage systems, LIBs have attracted significant attention for their high energy density, excellent cyclic performance, and environmental benignity. Although LIBs have occupied a part of the market, such as hybrid electric vehicles, portable electronic equipment, and other energy storage fields, many fundamental issues are required to be solved. The alloy materials and conversion materials with a high gravimetric and volumetric capacity still

face the challenges involving the massive volume expansion and the low electrical conductivity impede their broad application in the energy storage fields.

The objectives of the thesis are to address the challenges above and improve the electrochemical performance for LIBs. In the thesis, Si and Co_3O_4 were taken as examples to verify the feasibility of the solutions. Si has been considered as one of the most potential anode materials for its largest specific capacity. In Chapter 3, multi-walled carbon nanotubes (MWCNTs)/copper nanowires (Cu NWs)-coated on the Cu foils were used as a 3D porous substrate for Si deposition. The highly conductive Cu NWs cooperating with robust MWCNTs improve not only the inferior electronic conductivity of the Si active material but also the total frame stability. Furthermore, the three-dimensional structure creates numerous voids on the surface of the Cu foils. Such a porous structure of the modified current collector offers flexible volume expansion of active materials during lithiation/delithiation processes. Interestingly, silicon was deposited by the template of Cu NWs and MWCNTs to form Cu NWs/Si and MWCNTs/Si core-shell structures simultaneously, which could minimize the deformation strain and significantly improve the long-term cycling performance in a real battery.

In Chapter 3, it is demonstrated that the highly conductive Cu NWs applied in the electrode of Si-based LIBs can enhance the cycling performance by increasing the electrons diffusion efficiency. However, the current collector (Cu foils) used in Chapter 3 accounts for a majority of the weight of the whole electrode, which is not beneficial

to the application in portable or wearable electronic devices. Therefore, in Chapter 4, Cu NWs were introduced to build a 3D conductive framework to support the Si NPs with carbon outer layers as a free-standing anode for LIBs. The 3D framework created by the intertwined Cu NWs accompanying the thin-film carbon shell not only allows the Si NPs to distribute uniformly but also provides an efficient transmission pathway for electrons and ions. Meanwhile, considerable interspace left by the 3D structure can relieve the stress produced by the vast volume expansion of Si NPs. In addition, the Cu NWs@C core-shell structure strengthens the stability of the 3D framework. Meanwhile, the carbon layer encapsulating Si along Cu NWs enhances the contact between the Si NPs and Cu NWs, leading to excellent electrochemical performance of the Cu NWs/Si NPs@C composite electrode.

In Chapter 5, two-dimensional layered MXene, similar to graphene, was used to improve the electrochemical performance of anodes for LIBs. MXene is endowed with high electrical conductivity as well as high strength with a stable structure. Therefore, a facile strategy for preparing Co_3O_4 nanoparticles incorporated with MXene nanosheets on Ni foams has been developed. Four distinguishing features were achieved for this Co_3O_4/MXene composite electrode: (i) The large interlayer spacing of MXene nanosheets allows the Co_3O_4 nanoparticles to distribute uniformly, functioning as a flexible buffer to restrain the volume expansion. (ii) The intercalation of Co_3O_4 in MXene nanosheets prevents not only the agglomeration of Co_3O_4 nanoparticles but also the stacking of MXene nanosheets. (iii) The MXene provides a 3D framework to enhance electrons and Li^+ transmission efficiency. (iv) The mass loading of anode

materials on Ni foam increases significantly due to the considerable Co_3O_4 nanoparticles attached to the MXene nanosheets, which offers a large surface area in the nanoscale.

Concerning each composite electrode, various characterization techniques, such as XRD, Raman, SEM, and TEM, were conducted to investigate the morphology and structure of the composite. Moreover, the electrochemical measurement was performed on each as-prepared composite electrodes in three chapters to analyze their electrochemical performance. The corresponding specific capacity of the composite electrodes was measured at constant current density over long-term cycling and at various current densities to investigate the rate capability of batteries.

1.7 References

[1] M. I. Hoffert, K. Caldeira, G. Benford, D. R. Criswell, C. Green, H. Herzog, A. K. Jain, H. S. Kheshgi, K. S. Lackner, J. S. Lewis, H. D. Lightfoot, W. Manheimer, J. C. Mankins, M. E. Mauel, L. J. Perkins, M. E. Schlesinger, T. Volk, and T. M. L. Wigley, "Advanced Technology Paths to Global Climate Stability: Energy for a Greenhouse Planet," *Science,* vol. 298, no. 5595, pp. 981-987, 2002.

[2] M. Li, J. Lu, Z. Chen, and K. Amine, "30 Years of Lithium-Ion Batteries," *Advanced Materials,* vol. 30, no. 33, p. 1800561, 2018.

[3] *Renewable Energy: An Overview*, N. R. E. L. U.S. Department of Energy DOE/GO-102001-1102, 2001.

[4] V. Etacheri, R. Marom, R. Elazari, G. Salitra, and D. Aurbach, "Challenges in the Development of Advanced Li-Ion Batteries: A Review," *Energy & Environmental Science,* vol. 4, no. 9, pp. 3243-3262, 2011.

[5] "Technical Assessment of Advanced Transit Bus Propulsion Systems " Battelle, Texas2002, Available: https://afdc.energy.gov/files/pdfs/dart_tech_assess.pdf.

[6] K. Song, D. A. Agyeman, J. Jung, M. R. Jo, J. Yang, and Y. M. Kang, "A Review of the Design Strategies for Tailored Cathode Catalyst Materials in Rechargeable Li-O_2 Batteries," *Israel Journal of Chemistry,* vol. 55, no. 5, pp. 458-471, 2015.

[7] Hristian Julien • Alain Mauger and A. V. K. Zaghib, *Lithium Batteries* Springer, 2016.

[8] Masaki Yoshio, Raloh J. Brodd, and A. Kozawa, *Lithium-Ion Batteries*. Springer, 2009.

[9] W. Kang, N. Deng, J. Ju, Q. Li, D. Wu, X. Ma, L. Li, M. Naebe, and B. Cheng, "A Review of Recent Developments in Rechargeable Lithium-Sulfur Batteries," *Nanoscale,* vol. 8, no. 37, pp. 16541-16588, 2016.

[10] M. Liu, N. Deng, J. Ju, L. Fan, L. Wang, Z. Li, H. Zhao, G. Yang, W. Kang, J. Yan, and B. Cheng, "A Review: Electrospun Nanofiber Materials for Lithium-

Sulfur Batteries," *Advanced Functional Materials,* vol. 29, no. 49, p. 1905467, 2019.

[11] Y. Liang, C. Z. Zhao, H. Yuan, Y. Chen, W. Zhang, J. Q. Huang, D. Yu, Y. Liu, M. M. Titirici, Y. L. Chueh, H. Yu, and Q. Zhang, "A Review of Rechargeable Batteries for Portable Electronic Devices," *InfoMat,* vol. 1, no. 1, pp. 6-32, 2019.

[12] W. Xu, J. Wang, F. Ding, X. Chen, E. Nasybulin, Y. Zhang, and J. G. Zhang, "Lithium Metal Anodes for Rechargeable Batteries," *Energy & Environmental Science,* vol. 7, no. 2, pp. 513-537, 2014.

[13] P. Shi, T. Li, R. Zhang, X. Shen, X. B. Cheng, R. Xu, J. Q. Huang, X. R. Chen, H. Liu, and Q. Zhang, "Lithiophilic LiC_6 Layers on Carbon Hosts Enabling Stable Li Metal Anode in Working Batteries," *Advanced Materials,* vol. 31, no. 8, p. 1807131, 2019.

[14] K. Mizushima, P. C. Jones, P. J. Wiseman, and J. B. Goodenough, "Li_xCoO_2 (0<x<-1): A New Cathode Material for Batteries of High Energy Density," *Materials Research Bulletin,* vol. 15, no. 6, pp. 783-789, 1980.

[15] J. Jiang and C. Zhang, *Fundamentals and Applications of Lithium-Ion Batteries in Electric Drive Vehicles*. John Wiley & Sons Singapore Pte. Ltd, 2015.

[16] J. L. Shi, D. D. Xiao, M. Ge, X. Yu, Y. Chu, X. Huang, X. D. Zhang, Y. X. Yin, X. Q. Yang, Y. G. Guo, L. Gu, and L. J. Wan, "High-Capacity Cathode Material with High Voltage for Li-Ion Batteries," *Advanced Materials,* vol. 30, no. 9, p. 1705575, 2018.

[17] S. S. Zhang, K. Xu, and T. R. Jow, "Study of the Charging Process of a $LiCoO_2$-Based Li-Ion Battery," *Journal of Power Sources,* vol. 160, no. 2, pp. 1349-1354, 2006.

[18] J. Cho, Y. W. Kim, B. Kim, J. G. Lee, and B. Park, "A Breakthrough in the Safety of Lithium Secondary Batteries by Coating the Cathode Material with $AlPO_4$ Nanoparticles," *Angewandte Chemie International Edition,* vol. 42, no. 14, pp. 1618-1621, 2003.

[19] J. Cho, Y. J. Kim, and B. Park, "Novel $LiCoO_2$ Cathode Material with Al_2O_3

Coating for a Li Ion Cell," *Chemistry of Materials,* vol. 12, no. 12, pp. 3788-3791, 2000.

[20] C. Li, H. P. Zhang, L. J. Fu, H. Liu, Y. P. Wu, E. Rahm, R. Holze, and H. Q. Wu, "Cathode Materials Modified by Surface Coating for Lithium Ion Batteries," *Electrochimica Acta,* vol. 51, no. 19, pp. 3872-3883, 2006.

[21] Z. Chen, Y. Qin, K. Amine, and Y. K. Sun, "Role of Surface Coating on Cathode Materials for Lithium-Ion Batteries," *Journal of Materials Chemistry,* vol. 20, no. 36, pp. 7606-7612, 2010.

[22] W. Ebner, D. Fouchard, and L. Xie, "The $LiNiO_2$/Carbon Lithium-Ion Battery," *Solid State Ionics,* vol. 69, no. 3, pp. 238-256, 1994.

[23] A. Rougier, I. Saadoune, P. Gravereau, P. Willmann, and C. Delmasa, "Effect of Cobalt Substitution on Cationic Distribution in $LiNi_{1-y}Co_yO_2$ Electrode Materials," *Solid State Ionics,* vol. 90, no. 1, pp. 83-90, 1996.

[24] I. Belharouak, W. Lu, D. Vissers, and K. Amine, "Safety Characteristics of $Li(Ni_{0.8}Co_{0.15}Al_{0.05})O_2$ and $Li(Ni_{1/3}Co_{1/3}Mn_{1/3})O_2$," *Electrochemistry Communications,* vol. 8, no. 2, pp. 329-335, 2006.

[25] C. Y. Jhu, Y. W. Wang, C. Y. Wen, and C. M. Shu, "Thermal Runaway Potential of $LiCoO_2$ and $Li(Ni_{1/3}Co_{1/3}Mn_{1/3})O_2$ Batteries Determined with Adiabatic Calorimetry Methodology," *Applied Energy,* vol. 100, pp. 127-131, 2012.

[26] Y. K. Sun, S. T. Myung, B. C. Park, J. Prakash, I. Belharouak, and K. Amine, "High-Energy Cathode Material for Long-Life and Safe Lithium Batteries," *Nature Materials,* vol. 8, no. 4, pp. 320-324, 2009.

[27] Z. Yang, J. Zhang, M. C. W. Kintner Meyer, X. Lu, D. Choi, J. P. Lemmon, and J. Liu, "Electrochemical Energy Storage for Green Grid," *Chemical Reviews,* vol. 111, no. 5, pp. 3577-3613, 2011.

[28] A. Yamada, "Lattice Instability in $Li(LixMn_{2-x})O_4$," *Journal of Solid State Chemistry,* vol. 122, no. 1, pp. 160-165, 1996.

[29] P. K. Nayak, E. M. Erickson, F. Schipper, T. R. Penki, N. Munichandraiah, P. Adelhelm, H. Sclar, F. Amalraj, B. Markovsky, and D. Aurbach, "Review on

Challenges and Recent Advances in the Electrochemical Performance of High Capacity Li- and Mn-Rich Cathode Materials for Li-Ion Batteries," *Advanced Energy Materials,* vol. 8, no. 8, p. 1702397, 2018.

[30] A. K. Padhi, K. S. Nanjundaswamy, and J. B. Goodenough, "Phospho-olivines as Positive-Electrode Materials for Rechargeable Lithium Batteries," *Journal of The Electrochemical Society,* vol. 144, no. 4, pp. 1188-1194, 1997.

[31] M. Gaberscek, R. Dominko, and J. Jamnik, "Is Small Particle Size More Important than Carbon Coating? An Example Study on $LiFePO_4$ Cathodes," *Electrochemistry Communications,* vol. 9, no. 12, pp. 2778-2783, 2007.

[32] J. Wang, Y. Zhang, M. Yi, Z. Shen, L. Liu, H. Liu, and X. Zhang, "Coating $LiFePO_4$ with Conductive Nanodots by Magnetron Sputtering: Toward High-Performance Cathode for Lithium-Ion Batteries," *Energy Technology,* vol. 7, no. 3, p. 1800634, 2019.

[33] H. El-Shinawi, E. J. Cussen, and S. A. Corr, "Morphology-Directed Synthesis of $LiFePO_4$ and $LiCoPO_4$ from Nanostructured $Li_{1+2x}PO_{3+x}$," *Inorganic Chemistry,* vol. 58, no. 10, pp. 6946-6949, 2019.

[34] N. V. Kosova, T. L. Kulova, N. F. Nikolskaya, O. A. Podgornova, A. Y. Rychagov, V. E. Sosenkin, and Y. M. Volfkovich, "Effect of Porous Structure of $LiCoPO_4$ on Its Performance in Hybrid Supercapacitor," *Journal of Solid State Electrochemistry,* vol. 23, no. 7, pp. 1981-1990, 2019.

[35] S. Tang, Z. Wang, H. Guo, J. Wang, X. Li, and G. Yan, "Systematic Parameter Acquisition Method for Electrochemical Model of 4.35 V $LiCoO_2$ Batteries," *Solid State Ionics,* vol. 343, p. 115083, 2019.

[36] S. B. Chikkannanavar, D. M. Bernardi, and L. Liu, "A Review of Blended Cathode Materials for Use in Li-Ion Batteries," *Journal of Power Sources,* vol. 248, pp. 91-100, 2014.

[37] S. Goriparti, E. Miele, F. De Angelis, E. Di Fabrizio, R. Proietti Zaccaria, and C. Capiglia, "Review on Recent Progress of Nanostructured Anode Materials for Li-Ion Batteries," *Journal of Power Sources,* vol. 257, pp. 421-443, 2014.

[38] M. V. Reddy, G. V. Subba Rao, and B. V. R. Chowdari, "Metal Oxides and Oxysalts as Anode Materials for Li Ion Batteries," *Chemical Reviews,* vol. 113, no. 7, pp. 5364-5457, 2013.

[39] J. Lu, Z. Chen, F. Pan, Y. Cui, and K. Amine, "High-Performance Anode Materials for Rechargeable Lithium-Ion Batteries," *Electrochemical Energy Reviews,* vol. 1, no. 1, pp. 35-53, 2018.

[40] M. Noel and V. Suryanarayanan, "Role of Carbon Host Lattices in Li-Ion Intercalation/De-intercalation Processes," *Journal of Power Sources,* vol. 111, no. 2, pp. 193-209, 2002.

[41] D. Rahner, S. Machill, H. Schlörb, K. Siury, M. Kloss, and W. Plieth, "Intercalation Materials for Lithium Rechargeable Batteries," *Journal of Solid State Electrochemistry,* journal article vol. 2, no. 2, pp. 78-84, 1998.

[42] W. Tao, P. Wang, Y. You, K. Park, C. Y. Wang, Y. K. Li, F. F. Cao, and S. Xin, "Strategies for Improving the Storage Performance of Silicon-Based Anodes in Lithium-Ion Batteries," *Nano Research,* journal article vol. 12, no. 8, pp. 1739-1749, 2019.

[43] K. I. Bolotin, Sikes, K.J., Jiang, Z., Klima, M., Fudenberg, G., Hone, J., Kim, P., Stormer, H.L., , "Ultrahigh electron mobility in suspended graphene," *Solid State Commun,* vol. 146, pp. 351–355, 2008.

[44] X. Du, Skachko, I., Barker, A., Andrei, E.Y., "Approaching ballistic transport in suspended graphene," *Nat. Nano,* vol. 3 no. 8, 2008.

[45] J. W. Kang, D. H. Kim, V. Mathew, J. S. Lim, J. H. Gim, and J. Kim, "Particle Size Effect of Anatase TiO_2 Nanocrystals for Lithium-Ion Batteries," *Journal of The Electrochemical Society,* vol. 158, no. 2, pp. A59-A62, 2011.

[46] M. M. Rahman, J.-Z. Wang, M. F. Hassan, D. Wexler, and H. K. Liu, "Amorphous Carbon Coated High Grain Boundary Density Dual Phase $Li_4Ti_5O_{12}$-TiO_2: A Nanocomposite Anode Material for Li-Ion Batteries," *Advanced Energy Materials,* vol. 1, no. 2, pp. 212-220, 2011.

[47] J. Xu, C. Jia, B. Cao, and W. F. Zhang, "Electrochemical Properties of Anatase

TiO_2 Nanotubes as an Anode Material for Lithium-Ion Batteries," *Electrochimica Acta,* vol. 52, no. 28, pp. 8044-8047, 2007.

[48] K. Amine, I. Belharouak, Z. Chen, T. Tran, H. Yumoto, N. Ota, S. T. Myung, and Y. K. Sun, "Nanostructured Anode Material for High-Power Battery System in Electric Vehicles," *Advanced Materials,* vol. 22, no. 28, pp. 3052-3057, 2010.

[49] N. Wang, Z. Bai, Y. Qian, and J. Yang, "Double-Walled Sb@TiO_2−x Nanotubes as a Superior High-Rate and Ultralong-Lifespan Anode Material for Na-Ion and Li-Ion Batteries," *Advanced Materials,* vol. 28, no. 21, pp. 4126-4133, 2016.

[50] G. Du, N. Sharma, V. K. Peterson, J. A. Kimpton, D. Jia, and Z. Guo, "Br-Doped $Li_4Ti_5O_{12}$ and Composite TiO_2 Anodes for Li-Ion Batteries: Synchrotron X-Ray and in situ Neutron Diffraction Studies," *Advanced Functional Materials,* vol. 21, no. 20, pp. 3990-3997, 2011.

[51] B. L. He, B. Dong, and H. L. Li, "Preparation and Electrochemical Properties of Ag-Modified TiO_2 Nanotube Anode Material for Lithium–Ion Battery," *Electrochemistry Communications,* vol. 9, no. 3, pp. 425-430, 2007.

[52] F. F. Cao, X. L. Wu, S. Xin, Y. G. Guo, and L. J. Wan, "Facile Synthesis of Mesoporous TiO_2−C Nanosphere as an Improved Anode Material for Superior High Rate 1.5 V Rechargeable Li Ion Batteries Containing $LiFePO_4$−C Cathode," *The Journal of Physical Chemistry C,* vol. 114, no. 22, pp. 10308-10313, 2010.

[53] S. M. Oh, J. Y. Hwang, C. S. Yoon, J. Lu, K. Amine, I. Belharouak, and Y. K. Sun, "High Electrochemical Performances of Microsphere C-TiO_2 Anode for Sodium-Ion Battery," *ACS Applied Materials & Interfaces,* vol. 6, no. 14, pp. 11295-11301, 2014.

[54] V. L. Chevrier, J. W. Zwanziger, and J. R. Dahn, "First Principles Study of Li–Si Crystalline Phases: Charge Transfer, Electronic Structure, and Lattice Vibrations," *Journal of Alloys and Compounds,* vol. 496, no. 1, pp. 25-36, 2010.

[55] R. A. Huggins, "Lithium Alloy Negative Electrodes," *Journal of Power Sources,* vol. 81–82, pp. 13-19, 1999.

[56] J. G. Ren, Q. H. Wu, H. Tang, G. Hong, W. Zhang, and S. T. Lee, "Germanium–Graphene Composite Anode for High-Energy Lithium Batteries with Long Cycle Life," *Journal of Materials Chemistry A,* vol. 1, no. 5, pp. 1821-1826, 2013.

[57] H. Wu and Y. Cui, "Designing Nanostructured Si Anodes for High Energy Lithium Ion Batteries," *Nano Today,* vol. 7, no. 5, pp. 414-429, 2012.

[58] C. M. Park, J. H. Kim, H. Kim, and H. J. Sohn, "Li-Alloy Based Anode Materials for Li Secondary Batteries," *Chemical Society Reviews,* Review vol. 39, no. 8, pp. 3115-3141, 2010.

[59] B. Liang, Y. Liu, and Y. Xu, "Silicon-Based Materials as High Capacity Anodes for Next Generation Lithium Ion Batteries," *Journal of Power Sources,* vol. 267, pp. 469-490, 2014.

[60] W. J. Zhang, "A Review of the Electrochemical Performance of Alloy Anodes for Lithium-Ion Batteries," *Journal of Power Sources,* Review vol. 196, no. 1, pp. 13-24, 2011.

[61] M. V. Shelke, H. Gullapalli, K. Kalaga, M. T. F. Rodrigues, R. R. Devarapalli, R. Vajtai, and P. M. Ajayan, "Facile Synthesis of 3D Anode Assembly with Si Nanoparticles Sealed in Highly Pure Few Layer Graphene Deposited on Porous Current Collector for Long Life Li-Ion Battery," *Advanced Materials Interfaces,* vol. 4, no. 10, p. 1601043, 2017, Art. no. 1601043.

[62] H. T. Nguyen, F. Yao, M. R. Zamfir, C. Biswas, K. P. So, Y. H. Lee, S. M. Kim, S. N. Cha, J. M. Kim, and D. Pribat, "Highly Interconnected Si Nanowires for Improved Stability Li-Ion Battery Anodes," *Advanced Energy Materials,* vol. 1, no. 6, pp. 1154-1161, 2011.

[63] C. K. Chan, H. Peng, G. Liu, K. McIlwrath, X. F. Zhang, R. A. Huggins, and Y. Cui, "High-Performance Lithium Battery Anodes using Silicon Nanowires," *Nat Nano,* vol. 3, no. 1, pp. 31-35, 2008.

[64] Y. Jin, S. Li, A. Kushima, X. Zheng, Y. Sun, J. Xie, J. Sun, W. Xue, G. Zhou, J. Wu, F. Shi, R. Zhang, Z. Zhu, K. So, Y. Cui, and J. Li, "Self-Healing SEI Enables

Full-Cell Cycling of a Silicon-Majority Anode with a Coulombic Efficiency Exceeding 99.9%," *Energy & Environmental Science,* 2017.

[65] R. Malini, U. Uma, T. Sheela, M. Ganesan, and N. G. Renganathan, "Conversion Reactions: a New Pathway to Realise Energy in Lithium-Ion Battery—Review," *Ionics,* vol. 15, no. 3, pp. 301-307, 2009.

[66] J. Cabana, L. Monconduit, D. Larcher, and M. R. Palacín, "Beyond Intercalation-Based Li-Ion Batteries: The State of the Art and Challenges of Electrode Materials Reacting Through Conversion Reactions," *Advanced Materials,* vol. 22, no. 35, pp. E170-E192, 2010.

[67] P. L. Taberna, S. Mitra, P. Poizot, P. Simon, and J. M. Tarascon, "High Rate Capabilities Fe_3O_4-Based Cu Nano-Architectured Electrodes for Lithium-Ion Battery Applications," *Nat Mater,* vol. 5, no. 7, pp. 567-573, 2006.

[68] H. Wang, L. Hu, C. Wang, Q. Sun, H. Li, and T. Zhai, "High-Loading Individually Dispersed $NiCo_2O_4$ Anchoring on Checkerboard-Like C/CNT Nanosheets as a Binder-Free High Rate Electrode for Lithium Storage," *Journal of Materials Chemistry A,* vol. 7, no. 8, pp. 3632-3641, 2019.

[69] B. Qu, L. Hu, Q. Li, Y. Wang, L. Chen, and T. Wang, "High-Performance Lithium-Ion Battery Anode by Direct Growth of Hierarchical $ZnCo_2O_4$ Nanostructures on Current Collectors," *ACS Applied Materials & Interfaces,* vol. 6, no. 1, pp. 731-736, 2014.

[70] ZhongShuai Wu, Wencai Ren, Lei Wen, Libo Gao, Jinping Zhao, Zongping Chen, Guangmin Zhou, Feng Li, and a. H. M. Cheng, "Graphene Anchored with Co_3O_4 Nanoparticles as Anode of Lithium Ion Batteries with Enhanced Reversible Capacity and Cyclic Performance," *ACS NANO,* vol. 4, no. 6, pp. 3187-3194, 2010.

[71] Y. Yao, Y. Zhu, S. Zhao, J. Shen, X. Yang, and C. Li, "Halide Ion Intercalated Electrodeposition Synthesis of Co_3O_4 Nanosheets with Tunable Pores on Graphene Foams as Free-Standing and Flexible Li-Ion Battery Anodes," *ACS Applied Energy Materials,* vol. 1, no. 3, pp. 1239-1251, 2018.

[72] N. Wang, T. Hang, H. Ling, A. Hu, and M. Li, "High-Performance Si-Based 3D Cu Nanostructured Electrode Assembly for Rechargeable Lithium Batteries," *Journal of Materials Chemistry A,* vol. 3, no. 22, pp. 11912-11919, 2015.

[73] Z. Zhang, Z. L. Wang, and X. Lu, "Multishelled Si@Cu Microparticles Supported on 3D Cu Current Collectors for Stable and Binder-Free Anodes of Lithium-Ion Batteries," *ACS Nano,* vol. 12, no. 4, pp. 3587-3599, 2018.

[74] S. Li, W. Xie, L. Gu, Z. Liu, X. Hou, B. Liu, Q. Wang, and D. He, "Facilely Scraping Si NNanoparticles@Reduced Graphene Oxide Sheets onto Nickel Foam as Binder-Free Electrodes for Lithium Ion Batteries," *Electrochimica Acta,* vol. 193, pp. 246-252, 2016.

[75] Y. Liu, K. Huang, Y. Fan, Q. Zhang, F. Sun, T. Gao, Z. Wang, and J. Zhong, "Binder-Free Si Nanoparticles@Carbon Nanofiber Fabric as Energy Storage Material," *Electrochimica Acta,* vol. 102, pp. 246-251, 2013.

[76] B. Liu, X. Wang, H. Chen, Z. Wang, D. Chen, Y. B. Cheng, C. Zhou, and G. Shen, "Hierarchical Silicon Nanowires-Carbon Textiles Matrix as a Binder-Free Anode for High-Performance Advanced Lithium-Ion Batteries," *Scientific Reports,* vol. 3, p. 1622, 2013.

[77] X. Ma, L. Chen, X. Ren, G. Hou, L. Chen, L. Zhang, B. Liu, Q. Ai, L. Zhang, P. Si, J. Lou, J. Feng, and L. Ci, "High-Performance Red Phosphorus/Carbon Nanofibers/Graphene Free-Standing Paper Anode for Sodium Ion Batteries," *Journal of Materials Chemistry A,* vol. 6, no. 4, pp. 1574-1581, 2018.

[78] H. Wang, H. Song, Z. Lin, X. Jiang, X. Zhang, L. Yu, J. Xu, L. Pan, J. Wang, M. Zheng, Y. Shi, and K. Chen, "Highly Cross-Linked Cu/a-Si Core-Shell Nanowires for Ultra-Long Cycle Life and High Rate Lithium Batteries," *Nanoscale,* vol. 8, no. 5, pp. 2613-2619, 2016.

[79] H. Guan, X. Wang, S. Chen, Y. Bando, and D. Golberg, "Coaxial Cu-Si@C Array Electrodes for High-Performance Lithium-Ion Batteries," *Chemical Communications,* vol. 47, no. 44, pp. 12098-12100, 2011.

[80] H. Song, H. X. Wang, Z. Lin, X. Jiang, L. Yu, J. Xu, Z. Yu, X. Zhang, Y. Liu, P.

He, L. Pan, Y. Shi, H. Zhou, and K. Chen, "Highly Connected Silicon–Copper Alloy Mixture Nanotubes as High-Rate and Durable Anode Materials for Lithium-Ion Batteries," *Advanced Functional Materials,* vol. 26, no. 4, pp. 524-531, 2016.

[81] H. Song, H. X. Wang, Z. Lin, L. Yu, X. Jiang, Z. Yu, J. Xu, L. Pan, M. Zheng, Y. Shi, and K. Chen, "Hierarchical Nano-Branched c-Si/SnO_2 Nanowires for High Areal Capacity and Stable Lithium-Ion Battery," *Nano Energy,* vol. 19, no. Supplement C, pp. 511-521, 2016.

[82] Q. Zhang, H. Chen, L. Luo, B. Zhao, H. Luo, X. Han, J. Wang, C. Wang, Y. Yang, T. Zhu, and M. Liu, "Harnessing the Concurrent Reaction Dynamics in Active Si and Ge to Achieve High Performance Lithium-Ion Batteries," *Energy & Environmental Science,* vol. 11, no. 3, pp. 669-681, 2018.

[83] R. Xu, G. Wang, T. Zhou, Q. Zhang, H.-P. Cong, X. Sen, J. Rao, C. Zhang, Y. Liu, Z. Guo, and S.-H. Yu, "Rational design of Si@carbon with robust hierarchically porous custard-apple-like structure to boost lithium storage," *Nano Energy,* vol. 39, pp. 253-261, 2017.

[84] X. Zhao, C. M. Hayner, M. C. Kung, and H. H. Kung, "In-Plane Vacancy-Enabled High-Power Si–Graphene Composite Electrode for Lithium-Ion Batteries," *Advanced Energy Materials,* vol. 1, no. 6, pp. 1079-1084, 2011.

[85] H. Wu, G. Chan, J. W. Choi, I. Ryu, Y. Yao, M. T. McDowell, S. W. Lee, A. Jackson, Y. Yang, L. Hu, and Y. Cui, "Stable Cycling of Double-Walled Silicon Nanotube Battery Anodes through Solid-Electrolyte Interphase Control," *Nature Nanotechnology,* vol. 7, no. 5, pp. 309-314, 2012.

[86] J. Luo, X. Tao, J. Zhang, Y. Xia, H. Huang, L. Zhang, Y. Gan, C. Liang, and W. Zhang, "Sn^{4+} Ion Decorated Highly Conductive Ti_3C_2 MXene: Promising Lithium-Ion Anodes with Enhanced Volumetric Capacity and Cyclic Performance," *ACS Nano,* vol. 10, no. 2, pp. 2491-9, 2016.

[87] Y. Zhang, Z. Mu, J. Lai, Y. Chao, Y. Yang, P. Zhou, Y. Li, W. Yang, Z. Xia, and S. Guo, "MXene/Si@SiO_x@C Layer-by-Layer Superstructure with

Autoadjustable Function for Superior Stable Lithium Storage," *ACS Nano,* vol. 13, no. 2, pp. 2167-2175, 2019.

[88] S. Luo, R. Wang, J. Yin, T. Jiao, K. Chen, G. Zou, L. Zhang, J. Zhou, L. Zhang, and Q. Peng, "Preparation and Dye Degradation Performances of Self-Assembled MXene-Co_3O_4 Nanocomposites Synthesized via Solvothermal Approach," *ACS Omega,* vol. 4, no. 2, pp. 3946-3953, 2019.

[89] S. Sun, C. Liao, A. M. Hafez, H. Zhu, and S. Wu, "Two-Dimensional MXenes for Energy Storage," *Chemical Engineering Journal,* vol. 338, pp. 27-45, 2018.

[90] M. Q. Zhao, M. Torelli, C. E. Ren, M. Ghidiu, Z. Ling, B. Anasori, M. W. Barsoum, and Y. Gogotsi, "2D Titanium Carbide and Transition Metal Oxides Hybrid Electrodes for Li-Ion Storage," *Nano Energy,* vol. 30, pp. 603-613, 2016.

[91] O. Mashtalir, M. Naguib, V. N. Mochalin, Y. Dall'Agnese, M. Heon, M. W. Barsoum, and Y. Gogotsi, "Intercalation and Delamination of Layered Carbides and Carbonitrides," *Nature Communications,* vol. 4, no. 1, p. 1716, 2013.

[92] D. Sun, M. Wang, Z. Li, G. Fan, L. Z. Fan, and A. Zhou, "Two-Dimensional Ti_3C_2 as Anode Material for Li-Ion Batteries," *Electrochemistry Communications,* vol. 47, pp. 80-83, 2014.

[93] F. Kong, X. He, Q. Liu, X. Qi, Y. Zheng, R. Wang, and Y. Bai, "Improving the Electrochemical Properties of MXene Ti_3C_2 Multilayer for Li-Ion Batteries by Vacuum Calcination," *Electrochimica Acta,* vol. 265, pp. 140-150, 2018.

[94] H. Li, M. Lu, W. Han, H. Li, Y. Wu, W. Zhang, J. Wang, and B. Zhang, "Employing MXene as a Matrix for Loading Amorphous Si Generated upon Lithiation towards Enhanced Lithium-Ion Storage," *Journal of Energy Chemistry,* vol. 38, pp. 50-54, 2019.

[95] D. c. Zuo, S. c. Song, C. s. An, L. b. Tang, Z. j. He, and J. c. Zheng, "Synthesis of Sandwich-Like Structured Sn/SnOx@MXene Composite through in-situ Growth for Highly Reversible Lithium Storage," *Nano Energy,* vol. 62, pp. 401-409, 2019.

Chapter 2: Experimental section

The experimental section mainly consists of the introduction to the various characterization or testing techniques. The principle of the characterization techniques and testing methods are involved.

2.1 Structural and physical characterization

The structural and physical characterization of materials involve X-ray diffraction, Raman spectrometer, scanning electron microscopy, energy-dispersive X-ray spectroscopy, and transmission electron microscopy.

2.1.1 X-ray diffraction

X-ray diffraction (XRD) has been considered as one of the most efficient techniques to investigate the crystalline structure of the materials. The XRD system used in this thesis was D8 Advance made by Bruker using a Cu Kα radiation source. During the measurement, the working voltage is 40 kV, and the current is 40 mA. XRD is composed of an X-ray generator, goniometer, X-ray detector, and X-ray control system. The X-ray beams originate from metal anode materials when they are struck by high-speed moving electrons. Today, Cu is regarded as one of the most popular metal anode materials used in XRD, compared with others such as Cr, Fe, Co, Mo, and Ag. The X-ray generation process occurs in a vacuum diode where cathode materials are heated and release thermal radiation electrons that move to anode with high speed under the high-voltage electric field [1]. X-rays beams (λ=1.5406 Å) arrive at the surface of

a sample through a monochromator with an incident angle of θ. Meanwhile, the X-ray beam interacts with the electrons of the sample. Contrary to ordinary visible light with low energy, the X-ray beam with high energy could penetrate the sample with a certain depth. Thus, the X-rays will diffract and reflect at considerable parallel planes. As illustrated in **Figure 2.1**, all reflected X-ray beams at different lattice planes travel in parallel with varying path lengths. Constructive interference occurs when the path lengths equal to an integer multiple (n) of the electromagnetic radiation wavelength (λ) [2]. In summary, the reflection of X-ray beams abides by Bragg's law (Equation (8)) [3].

$$n\lambda=2d\sin\theta \qquad (8)$$

In Equation (8), d stands for the lattice spacing, which is the distance between two atomic planes, and 2θ represents the diffraction angle. Notably, the lattice spacing (d) is a significant parameter consistent with the crystal structure and atomic composition.

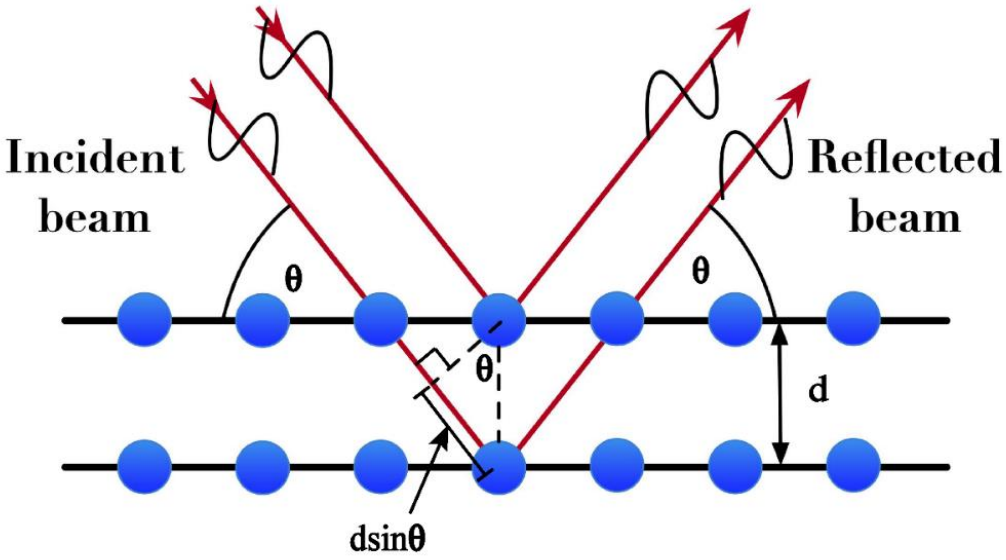

Figure 2.1 Illustration of atomic-scale crystal lattice planes following Bragg's law [2].

At the receiver terminal, the detector transfers the diffracted X-rays to diffracted patterns, including the intensity with corresponding diffraction angles. The crystalline size of sub-micrometer particles can be calculated by the Scherrer Equation (9) according to the XRD pattern [4].

$$L = \frac{K\lambda}{\beta \cos\theta} \qquad (9)$$

L is the average crystallite size, K is relative to the shape of the grains, and β is the breadth at half of the maximum intensity.

2.1.2 Raman spectroscopy

The Raman spectra used in the experiment is the HORIBA HR800 Raman system with a laser wavelength of 532 nm. Raman spectroscopy is a technique used to investigate the structure of the molecule. The analysis depends on the vibrational and rotational modes of molecules or other low-frequency modes of the system by measuring the frequency shift between the monochromatic incident light and inelastic scattering light [5]. The frequency shift, also known as Raman shift, only occurs when the incident photon has an inelastic collision with the molecule of the sample. The elastic collision brings about a reflected light with the same frequency as the incident light without any energy exchanges, namely Rayleigh scattering [6]. On the contrary, the inelastic collision occurs when the incident photon hits a molecule of the sample resulting in the excitation of the molecule to a virtual energy state after energy exchanges. Then, the molecule emits a photon and returns to a specific energy state that is different from the original one. Therefore, the inelastic scattering illustrates that the photon emitted by scattering light has higher or lower frequency compared with the incident photon corresponding to stokes and anti-stokes Raman scattering, respectively, as shown in **Figure 2.2**.

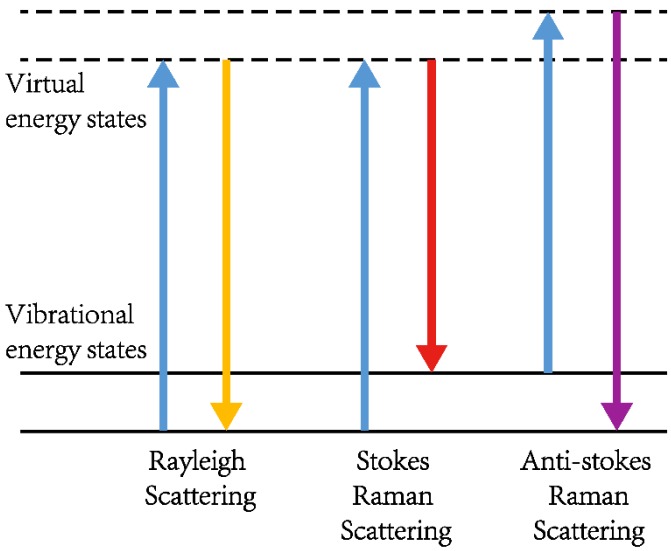

Figure 2.2 Diagram of the Raman scattering [7].

2.1.3 Scanning electron microscopy

The scanning electron microscopy (SEM) has been regarded as one of the most practical instruments for the determination and analysis of the morphology and structure of samples. SEM is widely used in various scientific fields and industry departments for its high resolution and three-dimensional imaging of objects [8]. For example, the resolution of commercial SEM achieves 10 nm, while the SEM for the scientific field is generally endowed with a high-revolution of 2.5 nm. **Figure 2.3** illustrates the schematic diagram of the SEM. An electron beam emitted by an electron gun transforms into a focused beam of the electron (~5 nm, diameter) on the surface of the specimen through a Wehnelt, and two or three condensers. The high-energy electron beam interacts with the specimen producing secondary electrons, backscattered electrons, absorption electrons, Auger electrons, cathodoluminescence, X-rays emission, and transmitted electrons [9]. All products could be considered as the signals carrying the characteristic information of the morphology and structure of the samples. These signals are collected by a receiver and sent to the image tube through an amplifier. One light spot on the image tube corresponds to one point on the sample. All characteristics are transferred to the image by the electron beam scanning the surface of the sample. In this thesis, the SEM was conducted by the JEOL JSM-6510 and Hitachi Regulus 8230.

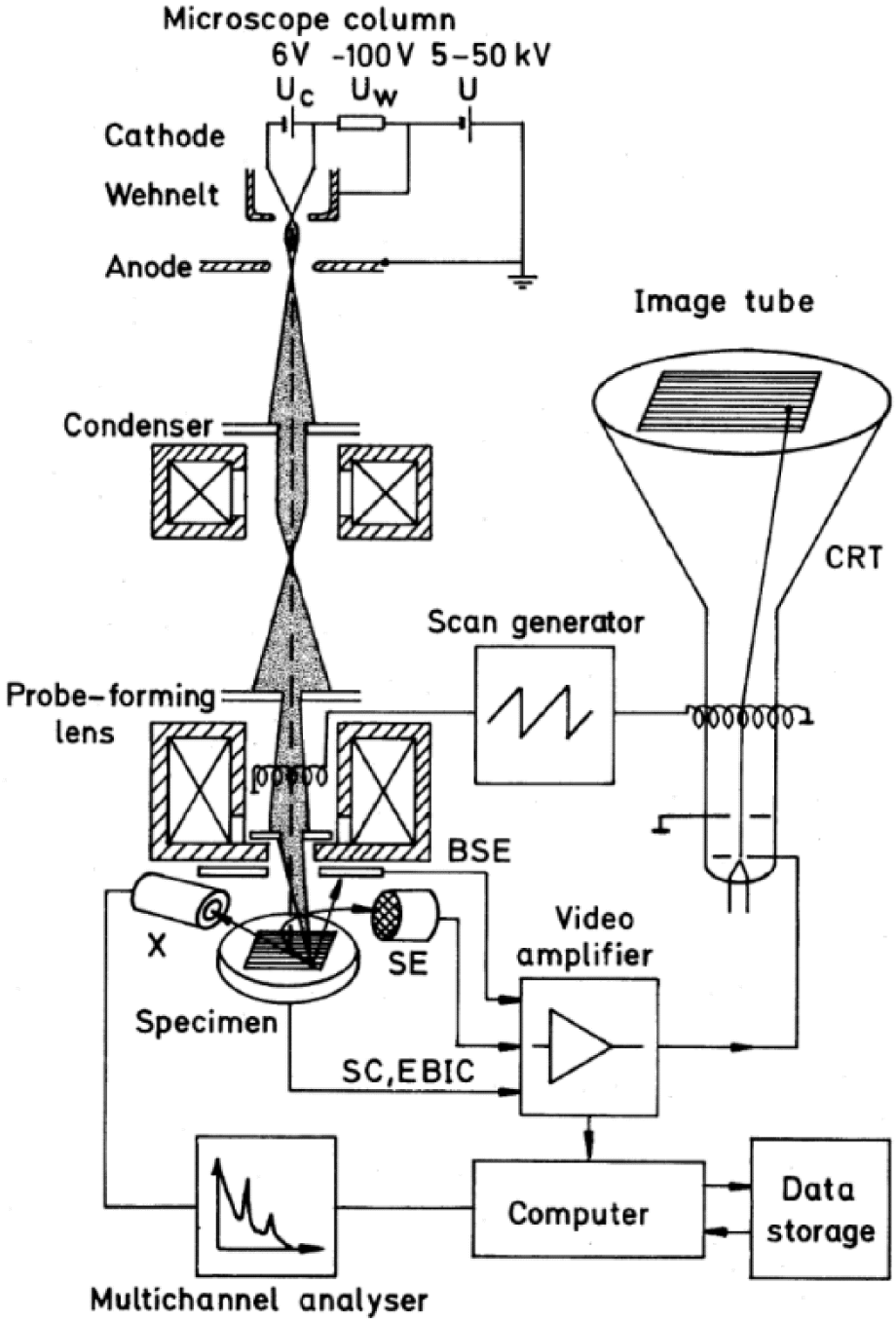

Figure 2.3 Structure and working principle of the SEM (BSE: backscattered electrons; SE: secondary electrons; SC: specimen current; EBIC: electron-beam-induced current; X: x-rays; CRT: cathode-ray tube) [10].

2.1.4 Transmission electron microscopy

Transmission electron microscopy is an analogical technique as SEM to characterize the morphology, structure, and elemental composition of samples. Contrary to SEM, transmission electron microscopy (TEM) and high-resolution transmission electron microscopy (HRTEM) can provide much higher magnification, even up to the atomic level.

The imaging principle of the TEM is divided into three categories according to the reaction of the incident electron beam when it interacts with the specimen. Firstly, if the sample is thin enough with a thickness of less than 10 nm, the electron beam could penetrate the sample with ignorable changes in amplitude. Hence, the changes in the phases of the electron beam carry the characteristic information of the specimen. Secondly, the diffraction of the electron beam occurs with the various amplitudes corresponding to the different locations on the sample. Finally, if the specimen has a large density, the scattering of the electron beam dominates within the different reactions. The receiver collects image information depending on the scattering angles. The large scattering angle indicates the scan part with larger weight and thickness, which implies that little electron beam could penetrate this area. As a consequence, the image relative to this part on the screen is darker. By contrast, the region with high brightness implies the part of the sample has a thinner thickness and smaller weight.

Compared with other characterization techniques, the sample preparation for TEM is more complicated. Normally, the sample suspension should be diluted to make sure

that the thickness of the testing sample ranging from 100 to 200 nm, which is thin enough for electron penetrating. Then, the suspension is dropped onto the films of carbon or copper grids. Regarding various materials, the preparation methods consist of tissue sectioning, mechanical milling, ion etching, and so on.

In the experiment, TEM machines with the type of Tecnai G2 F20S and FEI Talos F200x were applied to characterize the morphology and crystal structure of samples.

2.1.5 Energy-dispersive X-ray spectroscopy

Generally, the energy-dispersive X-ray spectroscopy (EDX) cooperates with SEM and TEM to determine the elemental composition and distribution in the sample. It analyzes the various elements depending on the corresponding energy of X-rays emitted from the specimen. As shown in **Figure 2.4,** when the high-energy incident electron beam strikes an atom, it excites an electron from the inner shell of the atom, leaving a vacancy. Another electron with higher energy from the outer shell is attracted to fill the hole at a lower energy level. During the transfer process, the electron releases energy in the form of X-rays [9, 11]. Therefore, the energy and number of X-rays are significant parameters to determine the elemental constituents in the sample.

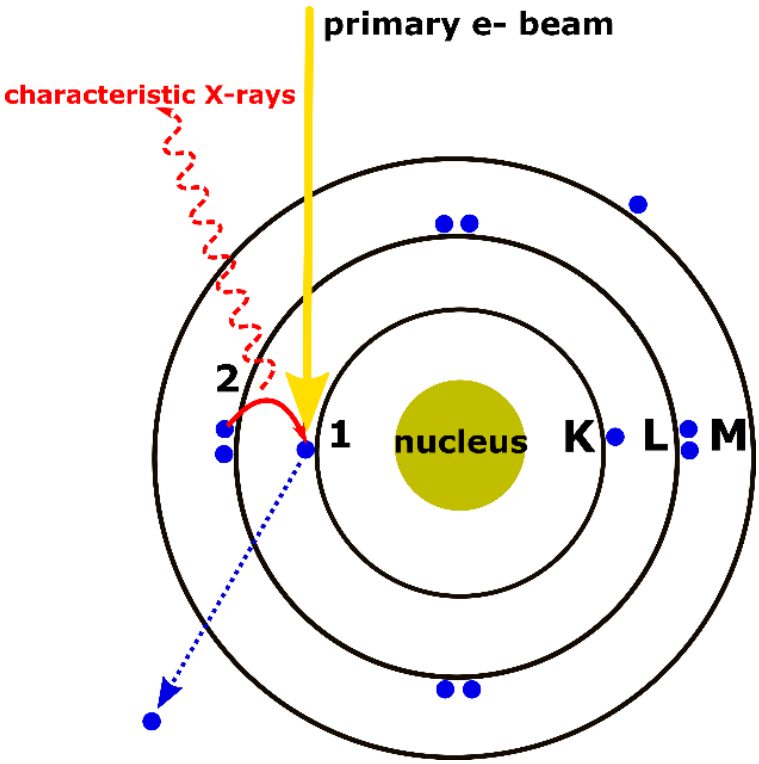

Figure 2.4 Illustration of the X-ray generation procedure [12].

2.2 Assembly and dismantlement of coin-type batteries

The common electrodes were prepared by mixing and stirring. The active materials, conductive agent (super-p), and adhesives (polyvinylidene fluoride, PVDF, or sodium alginate) were mixed according to the mass ratios of 8:1:1 by manual stirring. Then, the dispersing solution (N-Methyl-2-pyrrolidone, NMP, or DI water) around 4 times heavier than the active materials was added into the mixed powder. The whole mixture was magnetically stirred at the speed of ~800 rpm for 6 h. After that, the homogeneous slurry was coated onto the current collector like copper foils by a spreader. The product was dried in a vacuum oven at 80 ℃ for 12 h. The thickness of the electrode was measured in the range of 10-100 μm, which excluded the thickness of copper foils around 11-13 μm. Then, the electrodes were punched into discs with a diameter of 13 mm by a punch with the mass loading of active materials about 1-8 mg/cm^2.

The assembly of 2032-type coin-cells was completed in an argon-filled glove box (Vigor Sci-Lab). The cell consists of a cathode shell, cathode, separator, anode, and anode shell, which were assembled in sequence. Typically, the as-prepared electrodes plays a role as a working electrode, and the metallic lithium foil acts as both the counter and reference electrodes. The separator is the polypropylene–polyethylene–polypropylene trilayer membrane (Celgard 2325). Furthermore, the electrolyte of 1 M $LiPF_6$ dissolved in a mixture of dimethyl carbonate (DMC) and ethylene carbonate (EC) (1:1 by volume) was employed. Finally, the coin cells were sealed by a sealing machine

and stood still for 24 h to make sure that the electrodes were adequately infiltrated in the electrolyte.

After cycling performance testing, the coin cells were sent to the glove box again. An iron clamp was employed to dismantle the coin cell. The electrode was taken out and slightly washed using DMC. Then, the electrode was dried under the atmosphere of argon in the glove box for 12 h. Eventually, the electrode was sealed in a plastic bag and sent to SEM for morphology and structural characterization.

2.3 Electrochemical testing

2.3.1 Cyclic voltammetry

Cyclic voltammetry (CV) is a useful and popular electrochemical technique to investigate the electrochemical behavior in both anode and cathode materials during the lithiation and delithiation procedures of LIBs [13].

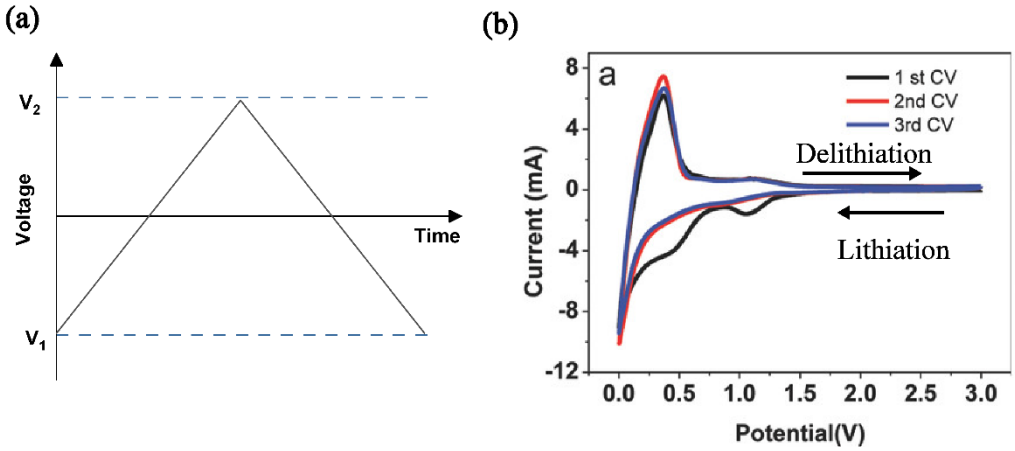

Figure 2.5 (a) The voltage sweeps between V_1 and V_2 with a fixed speed for CV testing. (b) The CV curves for graphite-based LIBs [14].

The controlling potential applied across the anode and cathode sweeps linearly versus time in the form of the triangular wave, as shown in **Figure 2.5a.** The applied voltage starts at V_1 and increases linearly. When it reaches the fixed potential V_2, it turns back with the same scan rate and returns to the initial potential V_1, which is recorded as a cycle. In this thesis, CV was conducted at a scan rate of 0.1 mV s^{-1} in a fixed potential range on an Autolab electrochemical workstation (PGSTAT302N). The potential set for the silicon-based anode and the Co_3O_4-based anode are in the ranges of 0.01-2 V and 0.01-3 V, respectively. Typically, the applied voltage starts at the open-circuit potential (OCP) and sweeps in the negative direction until it reaches 0.01 V. Subsequently, the applied voltage increased to 2 V or 3 V by the step of 0.1 mV s^{-1}. It turns back with the negative scan rate to the initial potential, which is considered as a scanning circulate.

The current response is measured versus the applied potential for several cycles, as plotted in **Figure 2.5b.** A representative CV plot has several cathodic and anodic peaks with corresponding potentials and currents. As fas as the LIBs are concerned, the total number of cathodic and anodic peaks is consistent with the electrochemical reactions occurring in the electrodes. Furthermore, during the first scan, the CV plot exhibits the broad peaks indicating the irreversible reaction, such as the formation of the SEI layer. Generally, during the reduction process, the Li-ions transfer from the anode to cathode, realizing the lithiation of the cathode. Conversely, during the oxidation process, the Li-ions move from the cathode to anode, namely the delithiation procedure. Taking the silicon-based LIBs as an example, the cathodic and anodic peaks represent the alloying

and de-alloying stages of the silicon and Li-ions, respectively. Besides, except for the first cycle, the shape of the following periods seems identical due to the reversibility of the redox reaction.

To analyze the electrochemical kinetics of the electrode, the electrodes were scanned at various scan rates, such as 0.2, 0.4, 0.8,1.2, 1.6, and 2.0 mV s^{-1}. According to cathodic and anodic peaks, the ratios of the diffusion and capacitive-controlled capacity contributions could be obtained.

2.3.2 Electrochemical impedance spectroscopy

Electrochemical impedance spectroscopy (EIS) is a powerful technique to measure the dielectric and transport properties of Li-ion battery according to its frequency response [15]. Contrary to the pure resistors, the impedance of the battery is dependent on frequency. EIS can measure the response current in the form of a sinusoid with the same frequency and different phases when the applied voltage is a sinusoidal signal with a small amplitude. The impedance of the Li-ion battery can be expressed as the Equation (10) [15, 16].

$$Z=\frac{U_0 \sin(wt)}{I_0 \sin(wt+\varphi)}=Z_0\frac{\sin(wt)}{\sin(wt+\varphi)}=Z_0\exp(j\varphi)=Z_0[\cos(\varphi)+\sin(j\varphi)] \qquad (10)$$

$$Z^{'}=R_E+\frac{R_{ct}}{1+\omega^2 {R_{ct}}^2 {C_{dl}}^2} \qquad (11)$$

$$Z^{''}=\frac{{R_{ct}}^2 C_{dl}\omega}{1+\omega^2 {R_{ct}}^2 {C_{dl}}^2} \qquad (12)$$

The typical Nyquist plot of the impedance is displayed as **Figure 2.6**, where Z' and -Z'' act as X and Y-axis representing the real and imaginary parts of the impedance, respectively. The plot is composed of four parts, including R_E, R_{ct}, C_{dl}, and Z_w, which corresponds to various transmission of Li-ions in the battery. R_E represents the electrical resistance of the electrolyte, which implies the diffusion efficiency of the Li-ions in the electrolyte. At high frequency, there is a semi-circle illustrating the charge transfer at the electrode/electrolyte interface. Therefore, R_{ct} is the charge transfer resistance of the interface between the electrode and electrolyte, which is in parallel with the C_{dl}. At the same time, C_{dl} is the double layer charging at the electrode surface. At lower frequency, Z_w stands for the Warburg impedance indicating the Li-ions diffusing in the working electrode materials [17, 18]. These electrical parameters have been summarized in Equation (11) and (12) with the corresponding circuit model shown in **Figure 2.6.**

In the experiment, EIS tests were also conducted on an Autolab electrochemical workstation over a frequency range of 100 kHz to 0.01 Hz with an ac voltage amplitude of 2 mV.

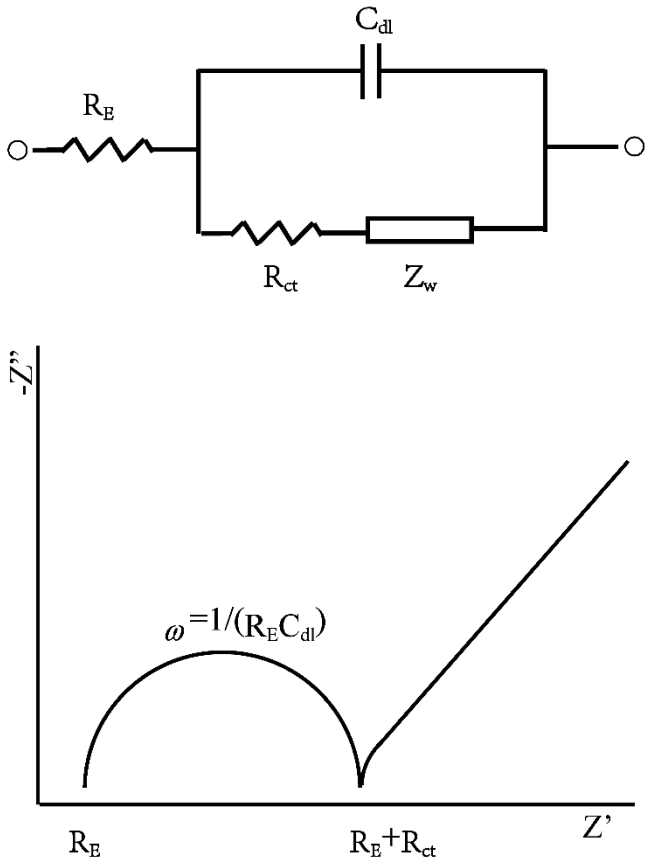

Figure 2.6 Simplified equivalent electrical circuit of the lithium-ion batteries and the corresponding Nyquist plot [15].

2.3.3 Galvanostatic cycling

The galvanostatic cycling is a typical and useful technique to investigate the electrochemical performance and cycling stability of the LIBs. It is conducted by applying a constant current to a cell and measuring the transient voltage. In other words, the LIBs charge and discharge at the constant current within a fixed working potential. As a result, the specific capacity that stands for the total charges stored in the cell is depending on the current density, voltage, and mass loading of the active materials. Commonly, the current density is selected as the fixed number, such as 1 A g^{-1}.

Moreover, the current density could be expressed as the theoretical capacity (mAh g^{-1}) divided by hours (h). 1 C (mA g^{-1}) indicates that it takes 1 hour to fully charge or discharge a cell using the current rate of 1 C. By comparison, C/10 means it spends 10 hours to achieve the same state by the current density of C/10. Therefore, the current density determines the charge and discharge speed of a cell.

Concerning the theoretical capacity, it is calculated by the Equation (13) [19].

$$Q_{theoretical} = \frac{nF}{3.6 \times M} (\text{mAh g}^{-1}) \qquad (13)$$

n is the amount of Li^+ per formula unit of the electrode material. F is Faraday constant (96485 C mol^{-1}). M is the molecular weight of the electrode material [20].

In this thesis, galvanostatic charge/discharge cycling tests were performed on a battery testing system (Neware CT-4008) in the voltage range of 0.01-2.0 V versus Li^+/Li at different current densities. Usually, three discharge/charge cycles at smaller a current density are conducted in advance for the activation of the battery. Then, the cycling test at a specified current density follows.

2.3.4 Rate capability

Rate capability measurement was conducted to investigate the cycling performance of Li-ion battery at various current densities. During the measurement, the current densities are designed as steps while the potential is fixed between the working range. Similarly, the current densities could be defined as a series of specific values such as 0.1, 0.2, 0.5, 1, 2, 5, 10, and 0.1 A g^{-1}. Each step undergoes the same discharge/charge cycles, except that when the current density returns to the initial rate, the battery will be tested over long-term cycling. Also, the current rates can be decided according to the theoretical capacity, namely 0.1 C, 0.5 C, 1 C, 2 C, 5 C, and 0.1 C. The specific capacity of the LIBs responds diversely to the various current densities. For instance, large current density means high charge/discharge speed, which indicates that a portion of Li-ions is not able to insert and extract in the electrode materials, leading to a smaller specific capacity. The factors causing the different rate performance include the electrical and ionic conductivity of the electrode materials, the size of active materials, Li-ions diffusion channels, and so on. Hence, rate capability measurement is a powerful method to investigate the electrochemical performance of the electrode materials.

2.4 References

[1] A. Guinier, *X-ray Diffraction in Crystals, Imperfect Crystals, and Amorphous Bodies*. Courier Corporation, 1994.

[2] R. E. Dinnebier and S. J. L. Billinge, *Powder Diffraction: Theory and Practice*. 2008.

[3] S. T. Misture and R. L. Snyder, "X-ray Diffraction," in *Encyclopedia of Materials: Science and Technology*, K. H. J. Buschow *et al.*, Eds. Oxford: Elsevier, 2001, pp. 9799-9808.

[4] A. L. Patterson, "The Scherrer Formula for X-Ray Particle Size Determination," *Physical Review,* vol. 56, no. 10, pp. 978-982, 1939.

[5] D. J. Gardiner, *Practical Raman Spectroscopy*. 1989.

[6] P. J. Hendra and P. M. Strattonx, "Laser-Raman Spectroscopy," *Chemical reviews,* 1969.

[7] P. Rostron, S. Gaber, and D. Gaber, "Raman Spectroscopy, Review," *International Journal of Engineering and Technical Research,* vol. 6, no. 1, pp. 2454-4698, 2016.

[8] J. Goldstein, *Practical Scanning Electron Microscopy: Electron and Ion Microprobe Analysis*. Springer Science & Business Media, 2012.

[9] J. Bergström, "Chapter 2 - Experimental Characterization Techniques," in *Mechanics of Solid Polymers*, J. Bergström, Ed.: William Andrew Publishing, 2015, pp. 19-114.

[10] L. Reimer, *Scanning Electron Microscopy: Physics of Image Formation and Microanalysis*. Spinger, 2013.

[11] C. Ganesh Kumar, S. Pombala, Y. Poornachandra, and S. Vinod Agarwal, "Chapter 4 - Synthesis, Characterization, and Applications of Nanobiomaterials for Antimicrobial Therapy," in *Nanobiomaterials in Antimicrobial Therapy*, A. M. Grumezescu, Ed.: William Andrew Publishing, 2016, pp. 103-152.

[12] A. Nanakoudis. (2019). *EDX Analysis with SEM: How Does it Work?* Available: https://www.thermofisher.com/blog/microscopy/edx-analysis-with-sem-how-

does-it-work/

[13] N. Elgrishi, K. J. Rountree, B. D. McCarthy, E. S. Rountree, T. T. Eisenhart, and J. L. Dempsey, "A Practical Beginner's Guide to Cyclic Voltammetry," *Journal of Chemical Education,* vol. 95, no. 2, pp. 197-206, 2018.

[14] C. Shen, G. Hu, L. Z. Cheong, S. Huang, J. G. Zhang, and D. Wang, "Direct Observation of the Growth of Lithium Dendrites on Graphite Anodes by Operando EC-AFM," *Small Methods,* vol. 2, no. 2, p. 1700298, 2018.

[15] D. D. Macdonald, "Reflections on the History of Electrochemical Impedance Spectroscopy," *Electrochimica Acta,* vol. 51, no. 8, pp. 1376-1388, 2006.

[16] *Basics of Electrochemical Impedance Spectroscopy*. Available: https://www.gamry.com/application-notes/EIS/basics-of-electrochemical-impedance-spectroscopy/

[17] E. P. Randviir and C. E. Banks, "Electrochemical Impedance Spectroscopy: an Overview of Bioanalytical Applications," *Analytical Methods,* vol. 5, no. 5, pp. 1098-1115, 2013.

[18] K. Dokko, M. Mohamedi, Y. Fujita, T. Itoh, M. Nishizawa, M. Umeda, and I. Uchida, "Kinetic Characterization of Single Particles of $LiCoO_2$ by AC Impedance and Potential Step Methods," *Journal of The Electrochemical Society,* vol. 148, no. 5, pp. A422-A426, 2001.

[19] H. Chen, "Study on the $Li_{1-x}Ni_{0.5}Mn_{1.5}O_4$ for Lithium Ion Batteries: a First-Principles Theory," *International Journal of Electrochemical Science,* vol. 12, pp. 11309-11315, 2017.

[20] P. Tan, Z. Wei, W. Shyy, and T. S. Zhao, "Prediction of the Theoretical Capacity of Non-Aqueous Lithium-Air Batteries," *Applied Energy,* vol. 109, pp. 275-282, 2013.

Chapter 3: MWCNTs/Cu NWs/Si composite as an anode material for lithium-ion batteries

3.1 Introduction

In this section, MWCNTs/ Cu NWs-coated on the Cu foil used as a three-dimensional porous current collector for Si active material has been developed to tackle the problems of silicon-based LIBs. The 3D porous MWCNTs/Cu NWs-coated Cu foil functions as a template for the subsequent deposition of the amorphous Si layer through a plasma-enhanced chemical vapor deposition (PECVD). The highly conductive Cu NWs cooperated with robust MWCNTs improve not only the inferior electric conductivity of the Si active material but also the total frame stability. Furthermore, the three-dimensional structure creates numerous voids on the surface of the Cu foils. Such a porous structure of the modified current collector offers flexible volume expansion during lithiation/delithiation processes. Interestingly, the composite exists in the form of Cu/Si and MWCNTs/Si core-shell structure simultaneously, which minimizes the deformation strain and dramatically improves the long-term cycling performance in a real battery. By adjusting the number of spin-coating, different layers of MWCNTs/Cu NWs were achieved, which has a significant impact on the cycling performance of electrodes. Also, the weight ratio of MWCNTs and Cu NWs has been proved as an essential factor affecting the cycling lifespan of electrodes. As a result, a half cell has been obtained without anycondctive additives or binder, which exihibts a high specific capacity of

1845 mAh g^{-1} in a half cell at a current density of 3.5 A g^{-1} after 180 cycles with a capacity retention of 85.1 %. The demonstrated three-dimensional MWCNTs/Cu NWs current collector coupled with Si active material might inspire new material development on high-performance LIBs.

3.2 Experimental section

3.2.1 Synthesis of Cu NWs

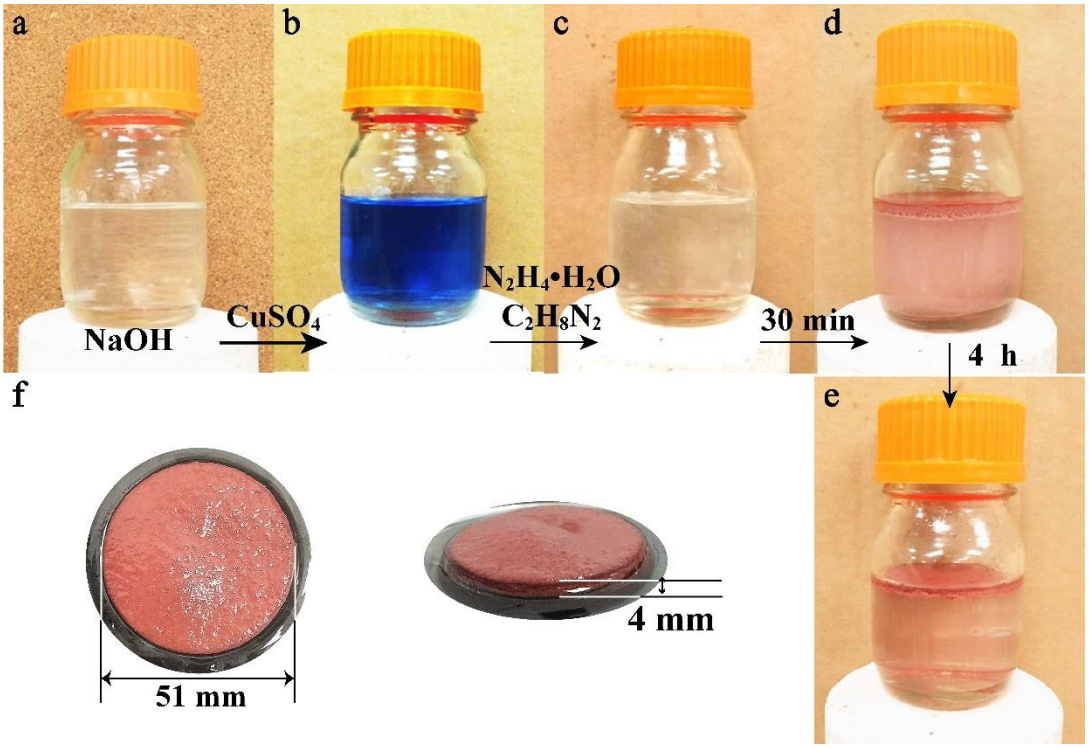

Figure 3.1 Schematics for preparing the Cu NWs.

Initially, Cu NWs were synthesized according to a hydrazine-assisted reduction approach reported by Chang's group with some adaption [1]. Firstly, an aqueous solution of NaOH (322 mL, 15 M) was prepared in a bottle by magnetic stirring. There was tremendous heat produced when NaOH was mixed with deionized water (DI).

After the NaOH aqueous solution cooling down to the ambient temperature, $CuSO_4 \cdot 5H_2O$ (28 mL, 0.1 M) solution was dropped into the NaOH solution avoiding the formation of copper oxides. Then, ethylenediamine (EDA) (2.6 mL, 99 wt. %) were added with constant stirring for 10 min to form a stable and royal blue solution. After that, 469 μL of hydrazine (N_2H_4) (35 wt. %) was slowly added and a transparent solution was obtained after further10 min vigorously stirring. Subsequently, the bottle was sealed and left still in an oil bath at 65 °C for 4 hours. It is clear that a slice of Cu NWs floating over the reaction solution, as shown in **Figure 3.1**. Cu NWs were collected by centrifugation (8500 rpm for 10 min) and rinsed four times with deionized (DI) water and ethanol. Eventually, they were dried in a vacuum oven at 80 °C for 12 h.

3.2.2 Preparation of Cu NWs and MWCNTs suspension

The suspension of Cu NWs dispersed in isopropyl alcohol (IPA) with a concentration of 25 mg/mL was prepared by ultrasonication for 1 h. Concurrently, MWCNTs were dispersed in IPA (1 mg mL^{-1}) with ultrasonic treatment for 3 h. Subsequently, both MWCNTs and Cu NWs suspension were mixed by different weight ratios of MWCNTs and Cu NWs (MWCNTs: Cu NWs = 1:0, 1:1, 1:5, 1:10, 1:15, 1:50, and 0:1, w/w) with continuous stirring to achieve a homogenous suspension.

3.2.3 Fabrication of porous current collector

For the porous MWCNTs/Cu NWs-coated current collector, the as-prepared mixture was spin-coated onto the Cu foils (2 cm × 2 cm), which had been pre-sonicated in acetone and ethanol to remove impurities on the surface. The parameters for spin-

coating were set around 3000 rpm for 20 s. The desired layers of MWCNTs/Cu NWs on Cu foils were obtained by repeating spin-coating with different cycles. Between each spin-coating period, the substrates were dried in a vacuum oven at 80 °C for 10 min. Besides, pure Cu NWs and pure MWCNTs dispersed in IPA were respectively spin-coated on the Cu foils as the control groups following the same procedure (**Figure 3.2**).

3.2.4 Deposition of Si layer on MWCNTs/Cu NWs-coated Cu foils

The amorphous Si layer was deposited on the porous MWCNTs/Cu NWs-coated Cu foil by PECVD. During the deposition, the temperature was kept at 100 °C for 90 min under a flow of 35.5 sccm SiH_4 with the chamber pressure of 188 mTorr and RF power of 11 W. The mass loading of Si weighted between 0.12 and 0.18 mg cm^{-2}. Eventually, the as-prepared electrodes were annealed at 450 °C under 46 sccm H_2 flow (1.4 Torr) for four hours in low-pressure chemical vapor deposition (LPCVD), in order to reduce the copper oxide (produced during the preparation process) to copper.

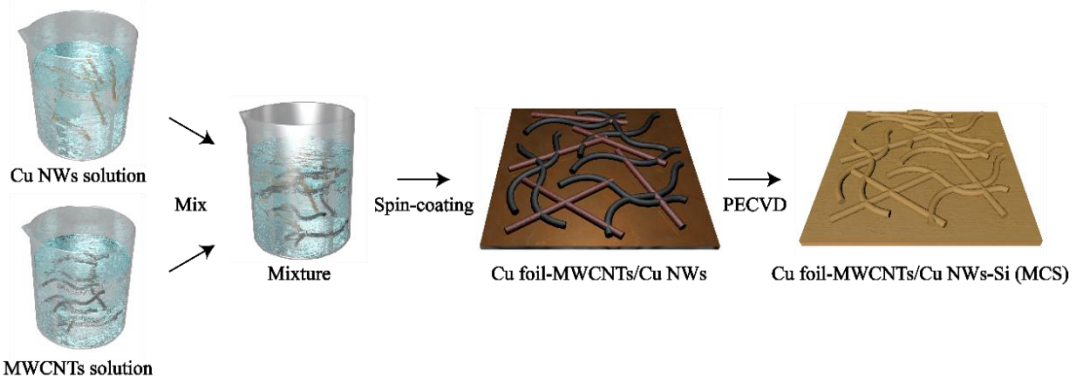

Figure 3.2 Schematic illustration showing the preparation procedure of the MWCNTs/Cu NWs/Si (MCS) composite electrode.

According to different pre-coating materials, the samples were labeled with different abbreviations. PCS and PMS represent pure Cu NWs/Si (MWCNTs: Cu NWs = 0:1) and pure MWCNTs/Si (MWCNTs: Cu NWs = 1:0) anodes. MCS1, MCS5, MCS10, MCS15, and MCS50 stand for the MWCNTs/Cu NWs/Si composites with 1:1, 1:5, 1:10, 1:15, and 1:50 different weight ratios of MWCNTs and Cu NWs, respectively.

3.3 Results and discussion

3.3.1 Characterization of pure Cu NWs/Si

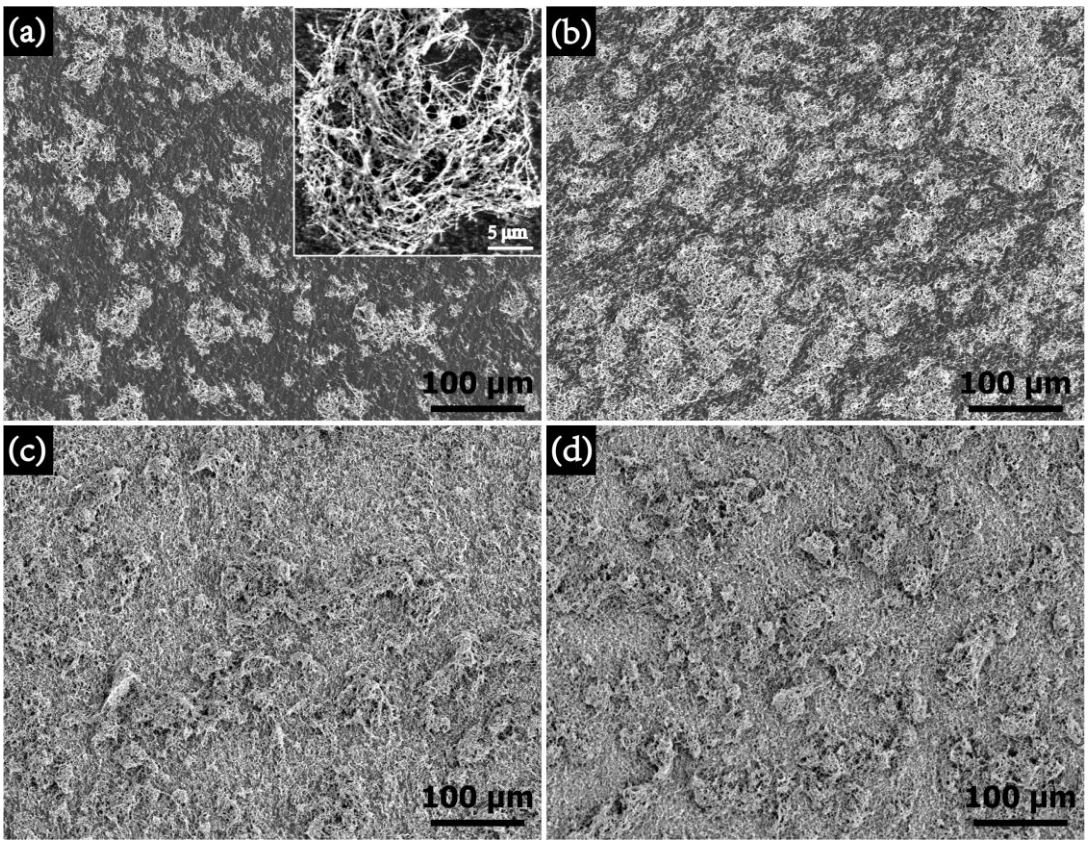

Figure 3.3 SEM images of pure Cu NWs-coated Cu foils as porous current collectors with 2 (a), 5 (b), 8 (c), and 12 (d) layers of Cu NWs by spin-coating.

To assess the optimal layer of Cu NWs coated on Cu foil, SEM images of Cu NWs with different layers by spin-coating are shown in **Figure 3.3a-d**, respectively. For the fewer layers, Cu NWs look like a nest in the insert image of **Figure 3.3a** and would be connected with increasing cycles of spin-coating. It is found that the abundant Cu NWs intertwine together, creating considerable internal void space for subsequently Si deposition. In **Figure 3.3a-b**, the Cu NWs nests have dispersed over the surface of Cu foil with some exposed area. By contrast, 8 and 12 layers of Cu NWs nearly cover the whole surface of Cu foils with more agglomerations, making the surface more uneven, as illustrated in **Figure 3.3c-d**.

3.3.2 Electrochemical performance of pure Cu NWs/Si

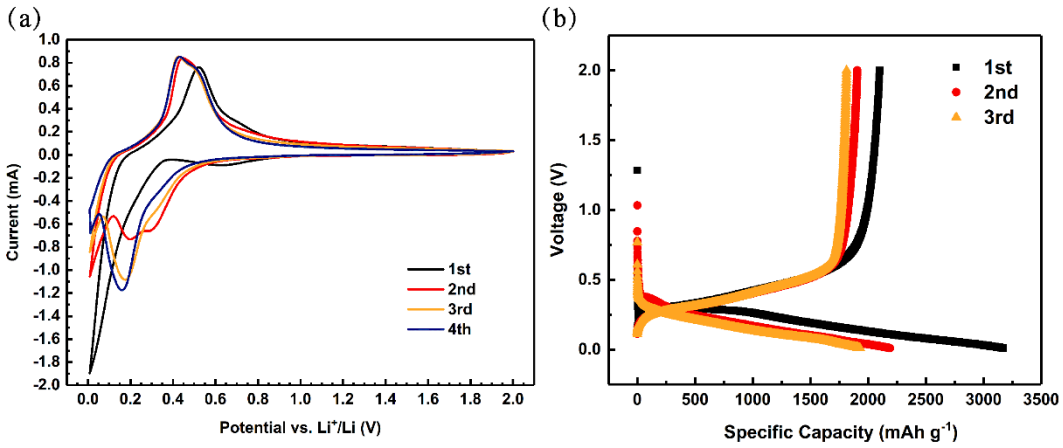

Figure 3.4 (a) Cyclic voltammetry curves for the first four cycles of PCS (pure Cu NWs/Si) composite electrode with 5 spin-coated layers of Cu NWs at a scan rate of 0.1 mV s^{-1} with the voltage range of 0.01-2.0 V. (b) Voltage profiles with initial three cycles of PCS composite electrode with 5 coating layers at a current density of 0.42 A g^{-1}.

The electrochemical performance of the PCS electrodes with different spin-coated layers was examined, as shown in **Figure 3.4 and Figure 3.5**. It shows the first four CV curves at a scan rate of 0.1 mV^{-1} with a potential window of 0.01-2.0 V (**Figure 3.4a**). There is a broad peak around 0.63 V during the first cathodic scan, which corresponds to the generation of SEI layers. The reaction is irreversible because this peak disappears in the following cycles, indicating that the initial formation of SEI layers might prevent the contact between the active materials and electrolyte and restrain the further decomposition of electrolyte [2, 3]. Two intensive reductive current peaks at 0.19 V and 0.03 V are attributed to the insertion of Li ions into a-Si-matrix, which causes the formation of amorphous Li_xSi alloy and crystalline $Li_{15}Si_4$ alloy. During the anodic scanning, two oxidation current peaks around 0.44 V and 0.52 V are consistent with the two-step dealloying process ($Li_{15}Si_4 \rightarrow Li_xSi \rightarrow Li$). A little variation is observed in the sequent scanning cycles, which indicates an entirely reversible and stable redox reaction of the electrode [4]. Particularly, the charge-discharge voltage profiles are exhibited in **Figure 3.4b**. The first three cycles at 0.42 A g^{-1} demonstrate the characteristic alloying/dealloying plateaus of the PCS anode. The discharge and charge capacities of the PCS electrode are 3173 and 2099 mAh g^{-1} with an initial Coulombic efficiency approaching 66.2 %. The large initial capacity loss is probably attributed to irreversible reactions, such as the formation of the SEI layer [5]. The SEI film is created when the organic electrolyte decomposes at the surface of anode materials [6]. Therefore, the generation of SEI film at the first cycle will prevent contact between the electrolyte and the surface of the anode, which leads to fewer irreversible

reactions and higher Coulombic efficiency at the following charge/discharge cycles.

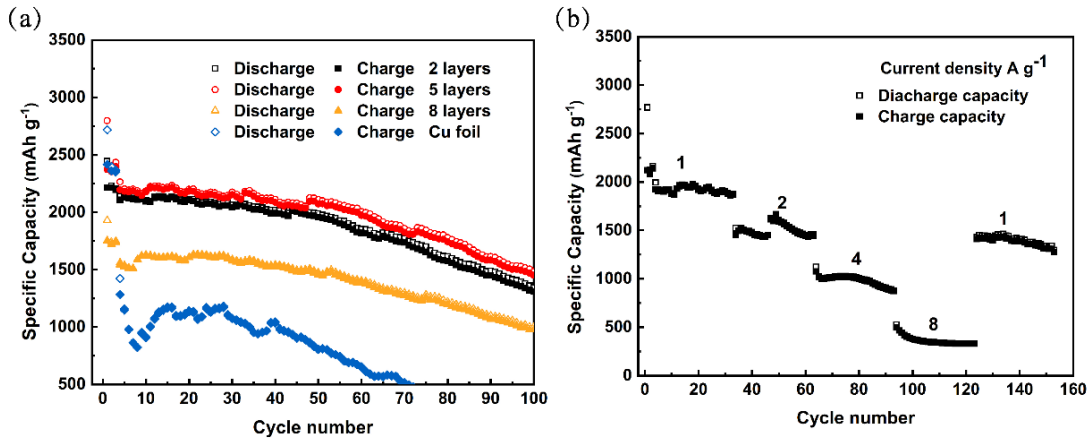

Figure 3.5 (a) Cycling performance of PCS composite electrodes with different spin-coated layers at 1 A g^{-1}. (b) Rate performance of the PCS composite electrode with 5 coating layers.

In **Figure 3.5a**, PCS electrodes with various layers of Cu NWs exhibit high cycling performance, which is superior to the electrode prepared by directly depositing Si film on the bare Cu foil (blue line). The planar Si/Cu foil electrode possesses a large initial capacity of around 2456 mAh g^{-1} but plummets to 500 mAh g^{-1} after only 70 cycles with a retention of 20 %. By contrast, the porous pure Cu NWs-coated current collector provides tremendous space to accommodate the huge volume expansion of Si during cycling. The staggered network structure is beneficial to the fast transmission of Li-ions. Hence, in comparison, the PCS composite could effectively mitigate the degradation of the Si-based LIBs. It is also noted that the PCS electrode with 5 spin-coated layers of Cu NWs has the best cycling performance among the electrodes. Interestingly, the PCS electrodes with increasing coating layers have a more compact surface, but the resulting cycling performance is unsatisfactory. The poor

electrochemical performance of PCS electrodes with 8 and 12 (not shown in **Figure 3.5**) coating layers may be attributed to the non-uniform deposition of Si by PECVD. When the thickness of Cu NWs increases with increasing the spin-coated layers, the Si tends to be deposited on the upper layers of Cu NWs, which leads to the uneven distribution of active materials. Besides, the thick Si on the upper layers would decrease the conductivity of the overall electrodes. These are probably the main reasons causing the low efficiency of electron transmission. **Figure 3.5d** exhibits the rate capability of the PCS composite with 5 coating layers. The LIBs were tested at the current densities from 1 to 8 A g^{-1}, showing the reversible discharge capacities of 1993, 1521, 1123, and 526 mAh g^{-1}, respectively. When the current density returns to 1 A g^{-1}, the electrode remains a capability of 1427 mAh g^{-1} with a retention of 72 %. However, the electrochemical performance of the PCS composite is unsatisfied since the capacity severely declines after 60 cycles. One possible reason is that the large strain might break the Cu NWs with very fine diameter during repeated cycling, which could be confirmed in the SEM image of the PCS electrode after 100 cycles (**Figure 3.16a**) [7]. To enhance the mechanical stability of the electrode, the robust MWCNTs were applied and cooperated with Cu NWs to form a stable and solid current collector.

3.3.3 Characterization of MWCNTs/Cu NWs/Si

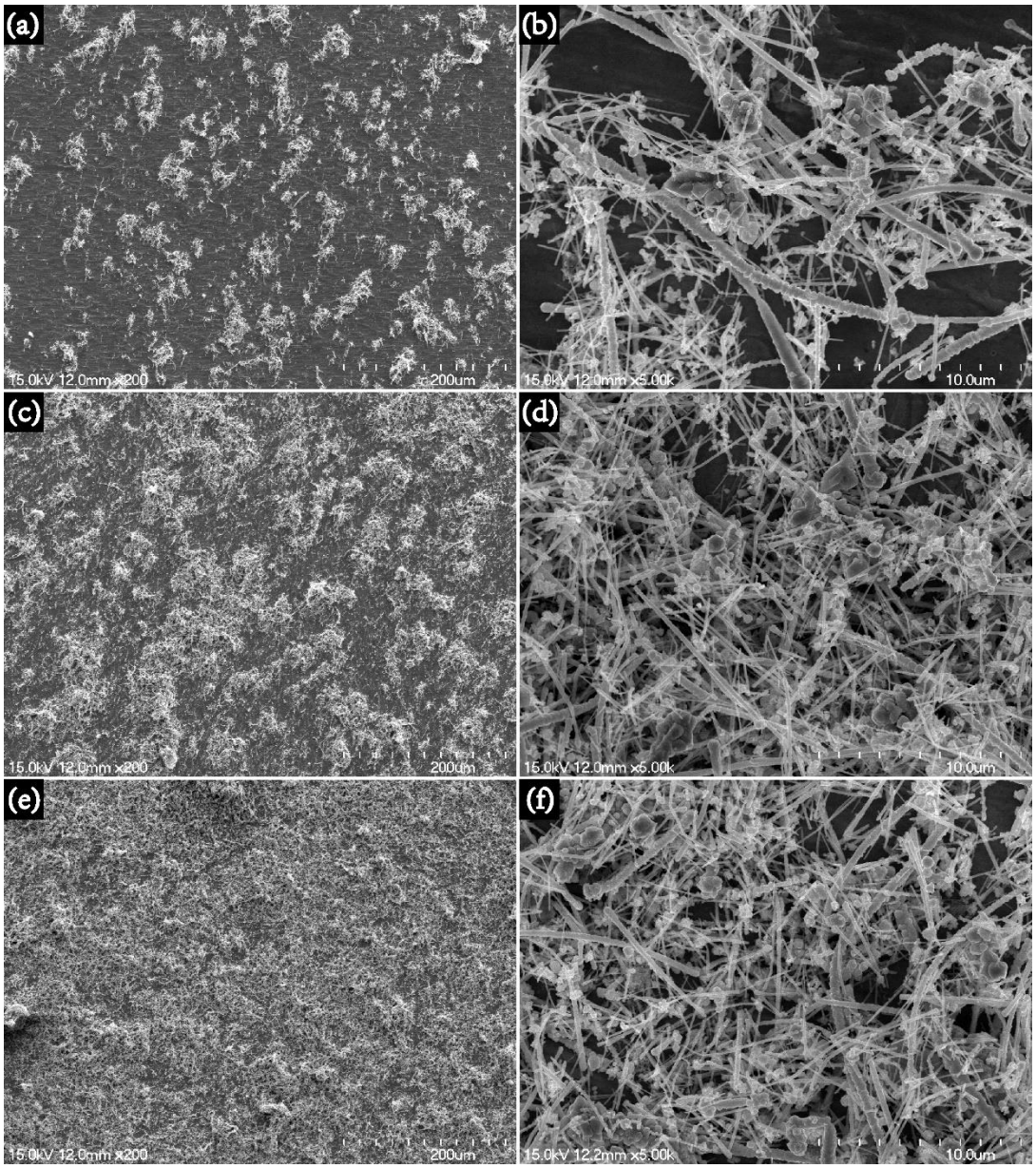

Figure 3.6 SEM images of MWCNTs/Cu NWs-coated Cu foils (MWCNTs: Cu NWs=1:10) with 2 (a-b), 5 (c-d), 8 (e-f) layers of spin-coating.

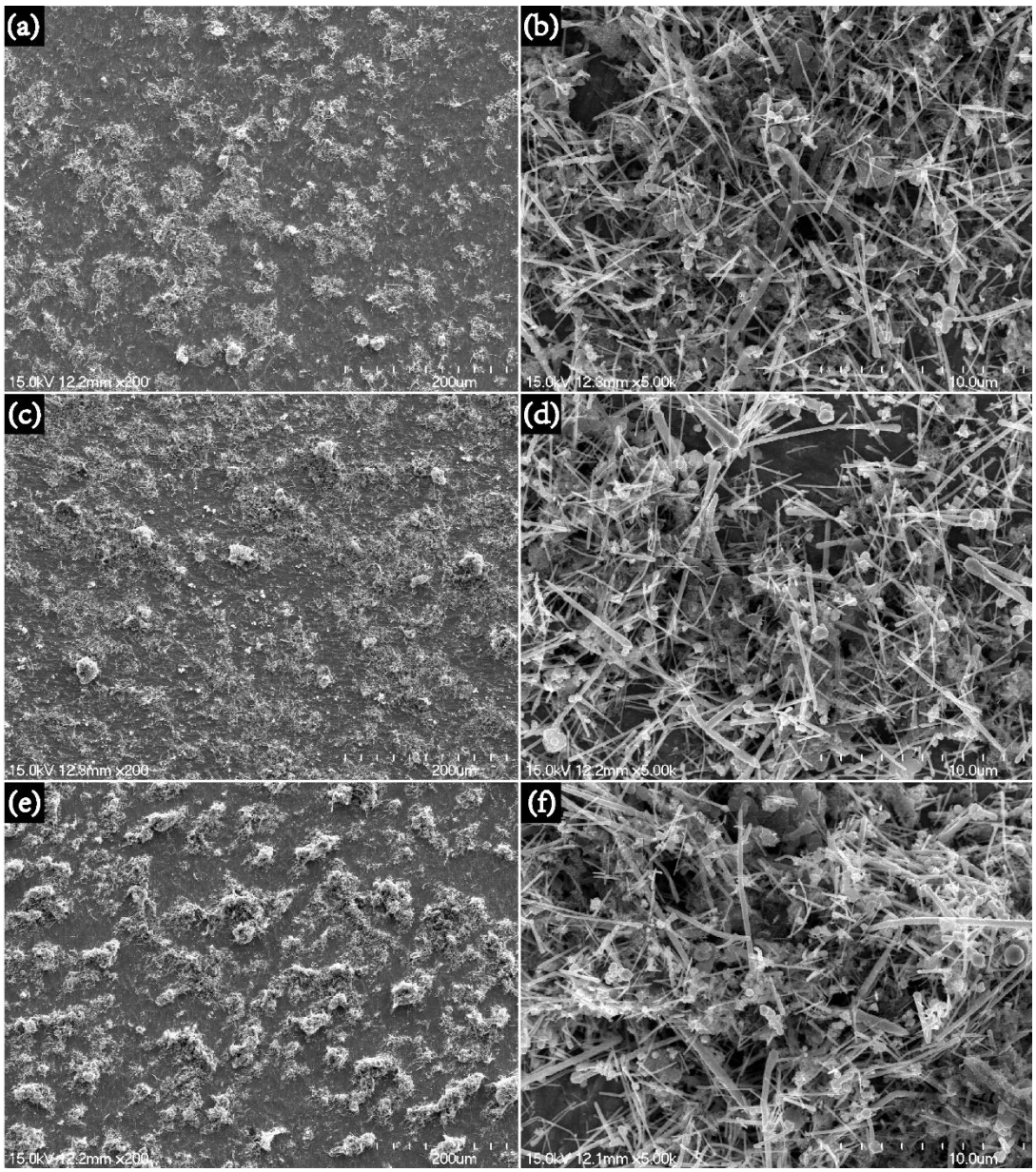

Figure 3.7 SEM images of MWCNTs/Cu NWs-coated Cu foils (MWCNTs: Cu NWs=1:1) with 2 (a-b), 5 (c-d), 8 (e-f) layers of spin-coating.

The mixed suspension of MWCNTs and Cu NWs with different weight ratios was spin-coated on the Cu foil to form the MWCNTs/Cu NWs-coated Cu foil, which serves as a 3D porous current collector. The corresponding SEM images of MWCNTs/Cu NWs-coated Cu foils (MWCNTs: Cu NWs=1:10 and 1:1) with different spin-coated layers were compared in **Figure 3.6** and **Figure 3.7,** respectively. For

MWCNTs: Cu NWs=1:10, as shown in **Figure 3.6**, it is clear that at low magnification, the SEM images of MWCNTs/Cu NWs-coated Cu foils are similar to that of pure Cu NWs-coated Cu foils (**Figure 3.3**). However, in **Figure 3.7e-f** for MWCNTs: Cu NWs=1:1, there is still some exposed Cu foil surface in the SEM images of MWCNTs/Cu NWs-coated Cu foils with 8 coating layers, which we attribute to the large portion of MWCNTs in the mixture aggregating together, ultimately resulting in nonuniform distribution on the Cu foil. It is indicated that the MWCNTs/Cu NWs-coated Cu foils (MWCNTs: Cu NWs=1:10) show the uniform spin-coating surface owing to the appropriate weight ratio of MWCNTs and Cu NWs.

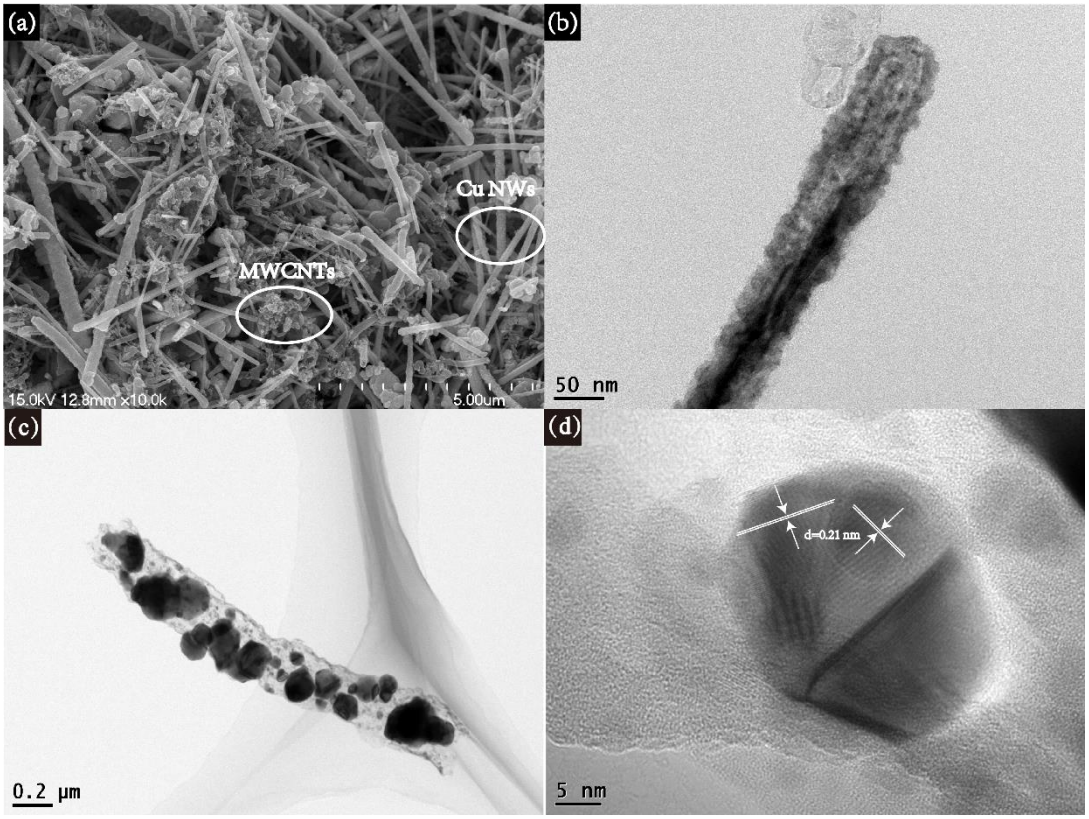

Figure 3.8 (a) SEM image of MCS1 (MWCNTs/Cu NWs/Si, MWCNTs: Cu NWs=1:1) composite electrode with 5 layers of MWCNTs/Cu NWs. (b) The TEM image of Cu NWs@Si core-shell structure before annealing. TEM images

of Cu NWs@Si after annealing (c) with the partially enlarged HRTEM views (d).

Figure 3.8a shows the SEM image of the MCS1 electrode with 5 layers of MWCNTs/Cu NWs (MWCNTs: Cu NWs = 1:1). Compared with the rigid Cu NWs, the MWCNTs with more flexible features tend to enwind around the Cu NWs. The straight Cu NWs interlinked with the tortuous MWCNTs are beneficial to enhance the connection between the Cu NWs, which creates a 3D conductive framework as an excellent current collector. However, it is also observed that MWCNTs agglomerate together (marked as the circle in **Figure 3.8a**) to form large clusters, losing the porosity of the electrode. Thus, it is significant to balance the weight ratio of MWCNTs and Cu NWs on the current collector. A single selected Cu/Si core-shell nanowire before annealing is shown in **Figure 3.8b**, where the grey shell encapsulates the black core. It could be estimated that the diameter of the original Cu NW is around 130 nm and the average thickness of the Si shell is in the range of 10-50 nm, according to **Figure 3.8b-c**. After annealing in the H_2 atmosphere, the Cu/Si core-shell structure involves space inside, as illustrated in **Figure 3.8c**. The hollow structure could be ascribed to a reduction from CuO to Cu, and the diffusion of Cu into the Si shell, as demonstrated in **Figure 3.8d** [8]. The lattice spacing of 0.21 nm at the black part corresponds to the (111) plane of Cu [4, 9], and the grey layer without lattice fringes represents the amorphous Si film, which is consistent with XRD results.

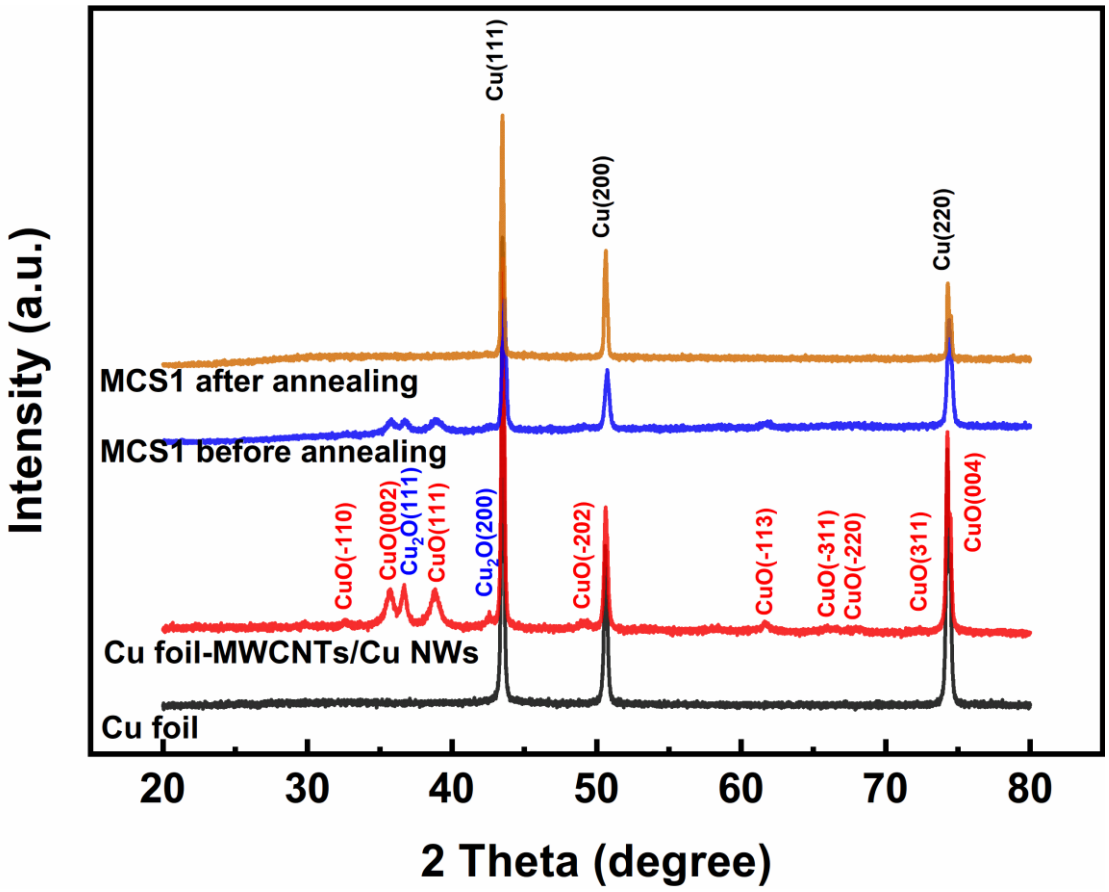

Figure 3.9 XRD patterns of the Cu foil (black), Cu foil coated by 5 layers of MWCNTs/Cu NWs (MWCNTs: Cu NWs=1:1) (red), MCS1 composite electrode before (blue) and after (brown) annealing.

To qualitatively characterize the phase composites of the prepared electrodes, XRD was conducted. The XRD patterns of a Cu foil (black), Cu foil coated with MWCNTs/Cu NWs (red), and MCS1 before (blue) and after (brown) annealing are shown in **Figure 3.9**. The patterns of all samples exhibit sharp and strong diffractions peaks emerging at 43.30°, 50.43°, and 74.13°, which are in good agreement to the face-centered cubic (fcc) Cu crystals (PDF#04-0836). For Cu foil coated with MWCNTs/Cu NWs and MCS1 before annealing, some minor peaks located at 35.54° and 38.71°are identified as CuO crystals (PDF#48-1548), and the peaks emerging at

36.42° and 42.30° are Cu_2O crystals (PDF#05-0667), respectively. The diffraction peaks of CuO and Cu_2O indicate that Cu NWs were partially oxidized during the fabrication process. It is clear that the intensity of copper oxide peaks decreases and disappears consequently after Si deposition and H_2 annealing. There are no prominent diffraction peaks associated with Si in the XRD patterns, suggesting the state of Si in the electrode is mainly amorphous. In an early report, Song *et al.* claimed the amorphous Si is more feasible to form crystallization alloy with Li-ions [10]. The existence of amorphous Si is in good accordance with TEM images (**Figure 3.8c-d**). The EDS elemental mapping not only shows the Si deposited on the porous MWCNTs/Cu NWs-coated Cu foil but also demonstrates the uniform distribution of all the elements in the MCS5 composite electrode as seen in **Figure 3.10**.

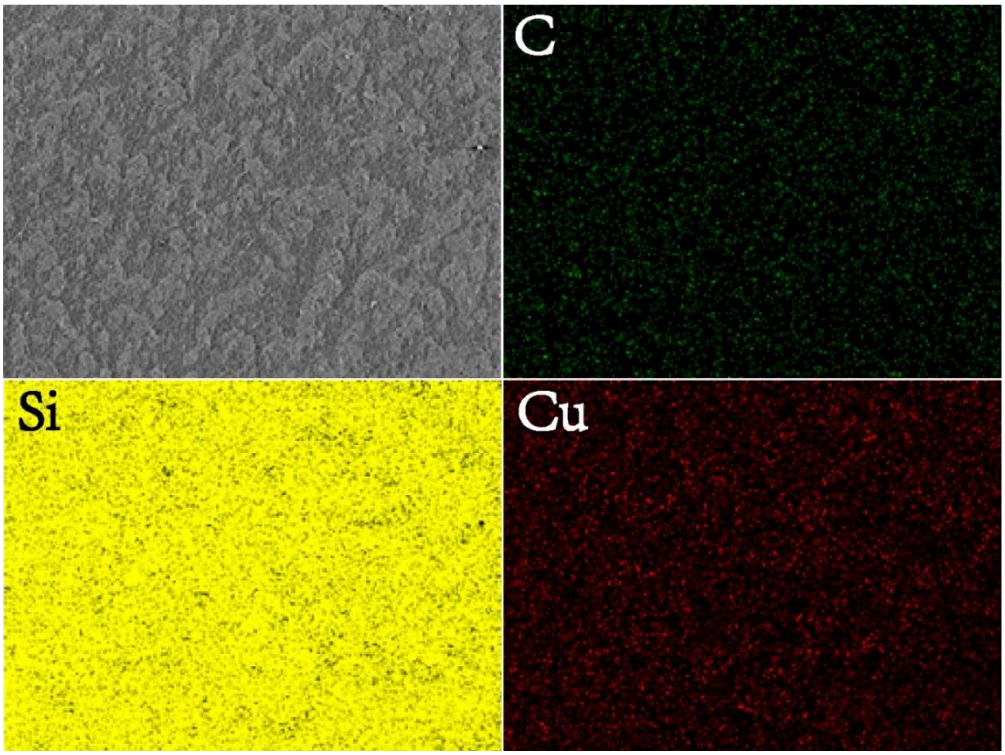

Figure 3.10 EDS elemental mappings of MCS5 composite electrode with 5 layers of MWCNTs/Cu NWs on Cu foils.

3.3.4 Electrochemical performance of MWCNTs/Cu NWs/Si

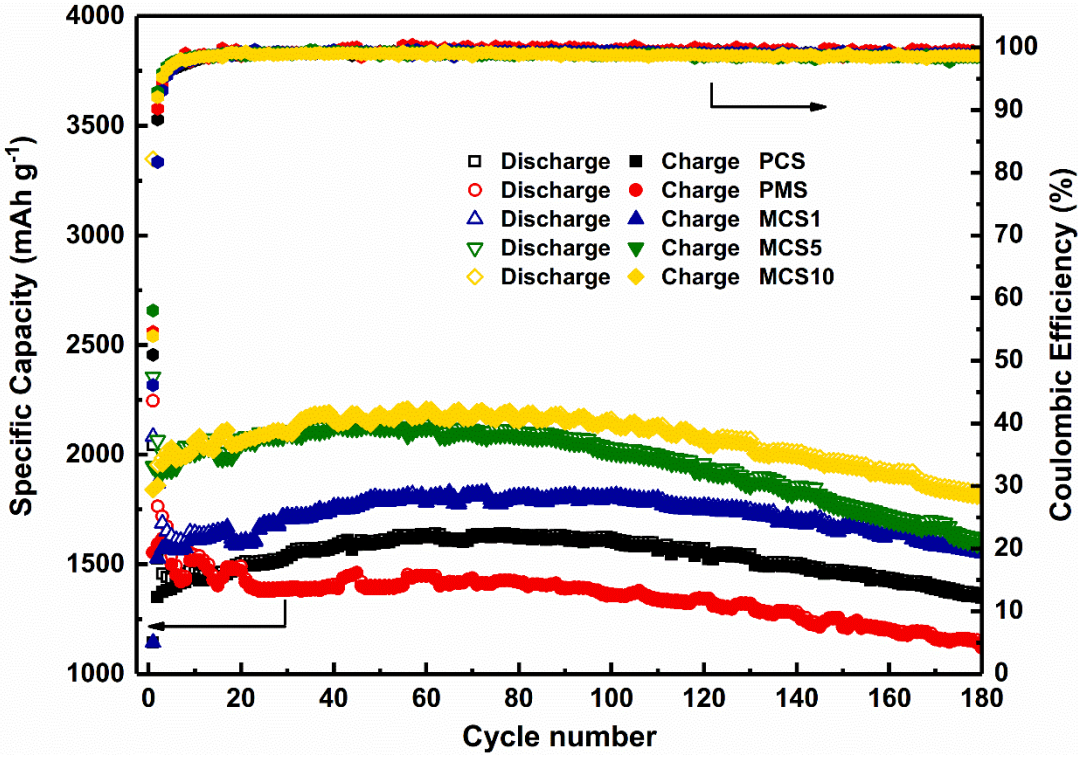

Figure 3.11 Cycling performance of PCS, PMS, and MCS composite electrodes with different weight ratios of MWCNTs and Cu NWs (with 5 layers of MWCNTs/Cu NWs) at 1 A g^{-1}

Figure 3.11 and **Figure 3.13** show the charge and discharge capacities versus cycle numbers for PCS (pure Cu NWs/Si), PMS (pure MWCNTs/Si), and MCS composite electrodes including MCS1 (MWCNTs: Cu NWs = 1:1), MCS5 (MWCNTs: Cu NWs = 1:5), and MCS10 (MWCNTs: Cu NWs = 1:10) scanned at 1 A g^{-1} and 3.5 A g^{-1}, respectively, as well as the correlative Coulombic efficiencies. The cycling performance in **Figure 3.11** was directly performed at 1 A g^{-1} without pre-cycling. Therefore, the first three Coulombic efficiencies of all electrodes are commonly lower than following efficiencies, which is related to the unstable and

inactivated electrochemical performance of the batteries. It is clear that the MCS10 electrode exhibits the highest reversible capacity of 1953 mAh g^{-1} and remains the largest capacity retention of 93.4 % after 180 cycles. Compared with the MCS10 electrode, the PCS, PMS, MCS1, and MCS5 electrodes present slightly lower reversible capacities at fourth cycle (1380, 1499, 1575, and 1953 mAh g^{-1}) and the correlative capacity retentions of 98.9 %, 76.1 %, 98.7 %, and 80.8 % after 176 cycles. It is worth noting that the PCS electrode in **Figure 3.11** shows a more stable cycling trend than that in **Figure 3.5a** because the dispersion agent of Cu NWs suspension was changed from DI water to IPA. Cu NWs disperse more evenly in IPA than DI water, resulting in a more uniform distribution of Cu NWs on Cu foils. In contrast with the PCS electrode, the PMS electrode has higher initial discharge and charge capacity but suffers a quick capacity drop to 900 mAh g^{-1} after 180 cycles. Although Cu NWs are inert for lithiation while MWCNTs are lithiation active materials with high capacitance, the MWCNTs coated on Cu foils contribute very little to the capacity due to the low weight (**Figure 3.12**). Besides, the MWCNTs have larger resistivity than Cu NWs, which consequently reduces the electrical contact between the active material and current collector and retards the rapid electron transmission. Thus, the concentration of MWCNTs in the MWCNTs/Cu NWs/Si composite electrodes has a crucial effect on the electrochemical performance. For example, in the MCS1 electrode, the MWCNTs account for 50 % weight of the spin-coating layer, which greatly decreases the electrical contact between active materials and Cu foils than PCS electrodes. Besides, the excessive flexible MWCNTs might fill up the pores created by cross-linked Cu NWs, leading to lower

porosity of the current collector. Therefore, Si tends to deposit on the surface rather than form the core-shell structure with nanowires and nanotubes. In other words, there is less space available to accommodate the volume expansion of Si [7]. Therefore, among MWCNTs/Cu NWs/Si electrodes, MCS1 has the lowest capacity.

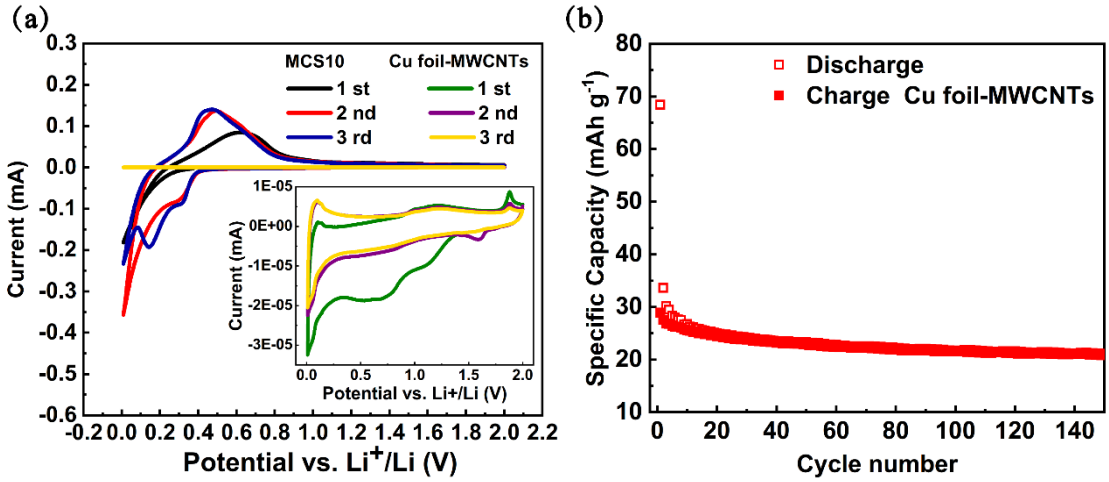

Figure 3.12 (a) Cyclic voltammetry curves for the first three cycles of MCS10 composite electrode with 5 layers of MWCNTs/Cu NWs. The inset image shows the CV curves of MWCNTs/Cu foil electrode with 5 layers of MWCNTs at a scan rate of 0.1 mV s^{-1} with the voltage range of 0.01-2.0 V; (b) cycling performance of MWCNTs/Cu foil electrode with 5 coating layers at 1 Ag^{-1}.

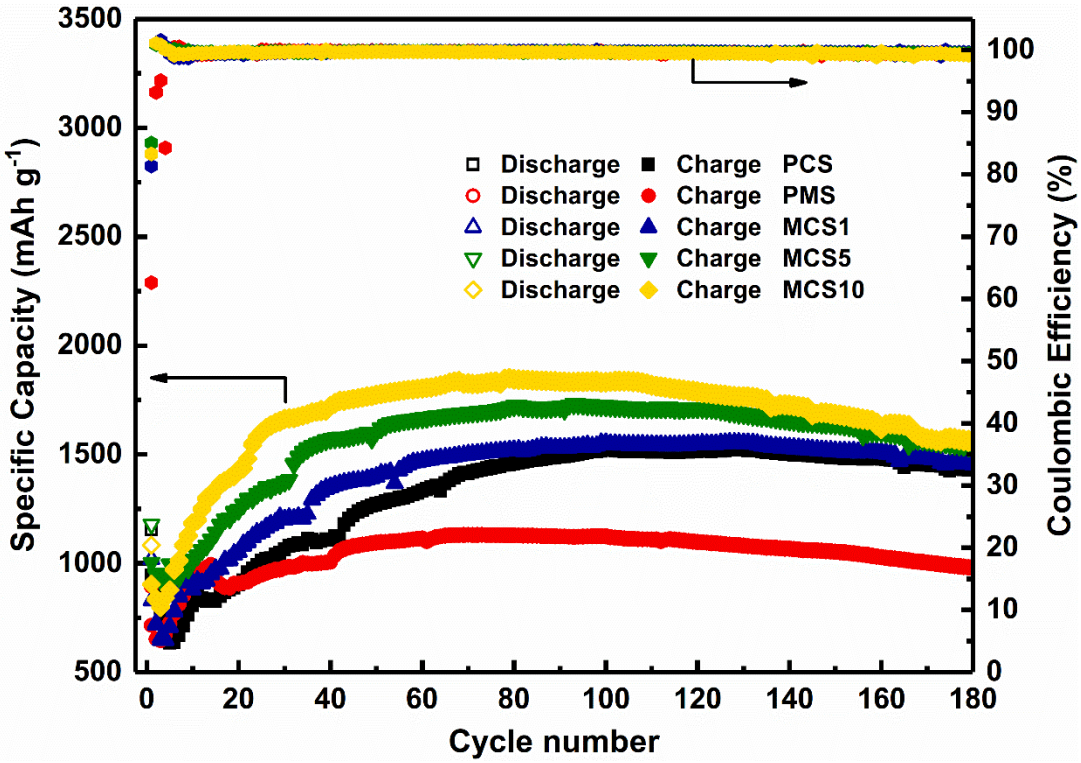

Figure 3.13 Cycling performance of PCS, PMS, and MCS composite electrodes with different weight ratios of MWCNTs and Cu NWs (with 5 layers of MWCNTs/Cu NWs) at 3.5 A g^{-1}.

To understand the cycling performance of these electrodes at a higher rate, the MCS electrodes were tested at 3.5 A g^{-1}, shown in **Figure 3.13**. Initially, the curves suddenly decrease to 633, 651, 676, 841, and 803 mAh g^{-1} in accordance with PCS, PMS, MCS1, MCS5, and MCS10 electrodes. There is an obvious increase of the capacity over the first 60 cycles, which is ascribed to the slow activation of the anode under large current density. Compared with Figure 3.12, the current rate in Figure 3.13 is 3.5 A g^{-1}, which indicates a larger amount of Li-ions diffusing to the anode and the faster charge/discharge speed. Commonly, the coin cells would stand by 24 h after assembling to improve the contact between the electrolyte and active materials.

However, only 24 h standing is not enough for a node to accept considerable Li-ions due to their insufficient contact with the electrolyte, which finally leads to the small capacities of all electrodes at the beginning. By contrast, there is only a small increase of capacity in Figure 3.12. After three or four cycles, the batteries tend to be stable and the specific capacity starts to increase gradually until achieving a full Li-ions storage capacity [11]. The highest reversible capacities for each electrode (PCS, PMS, MCS1, MCS5, and MCS10) are 1523, 1128, 1521, 1719, and 1845 mAh g^{-1} with corresponding capacity retentions of 93.9 %, 87.7 %, 96.3 %, 89.9 %, and 85.1 %, respectively. Likewise, the MCS10 electrode has the lowest capacity retention, and it possesses the highest charge and discharge capacity during 180 cycles.

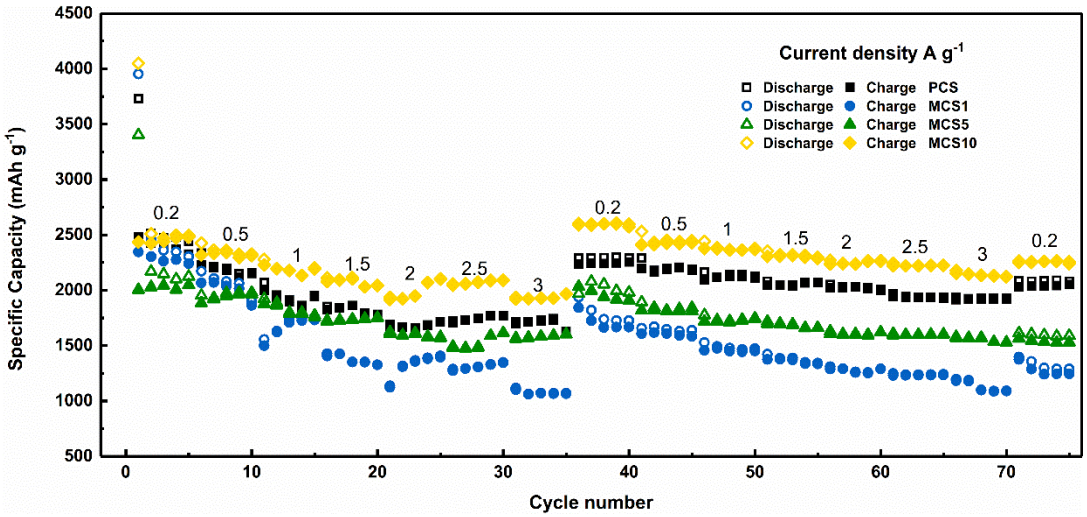

Figure 3.14 Rate performance of the MCS composite electrodes.

To assess the rate capability of the MCS electrodes, the batteries were tested with increasing current densities by a step of 0.2, 0.5, 1, 1.5, 2, 2.5, to 3 A g^{-1} and repeated steps, as illustrated in **Figure 3.14**. The composites (MCS1 and MCS5) show lower

capacities than that of the PCS electrode. However, the MCS10 electrode remains the highest reversible capacity due to the high concentration of conductive Cu NWs in the electrode. The little fluctuation observed during the first seven rates disappears in the next seven rates, which is ascribed to the instability and inactivation of the batteries at the beginning of the test. When the current density first returns to 0.2 A g^{-1}, the PCS, MCS1, MCS5, and MCS10 composite deliver capacities of 2289, 1841, 2031, and 2589 mAh $g^{-1,}$ respectively that are very approaching the initial discharge capacity. Meanwhile, the capacity of the MCS10 electrode even exceeds the initial value. Inspiringly, when the current density backs to 0.2 A g^{-1} again, the discharge capacities achieve 2081, 1374, 1563, and 2251 mAh g^{-1} for the PCS, MCS1, MCS5, and MCS10 composites with retentions of 90.9 %, 74.6 %, 77.0 %, and 86.9 %, respectively. The excellent capacity retentions indicate good stability of the electrode after high-rate discharge-charge cycles, which can highlight the excellent Li-ion storage reversibility. Further experiments were conducted to compare the rate performance of MCS10, MCS15, and MCS50, as shown in **Figure 3.15**, in which the electrochemical performance decreases when the weight ratio of MWCNTs and Cu NWs decreases from 1:10 to 1:50. Therefore, among the MWCNTs/Cu NWs/Si composite electrodes, the optimal ratio of MWCNTs and Cu NWs is found to be 1:10.

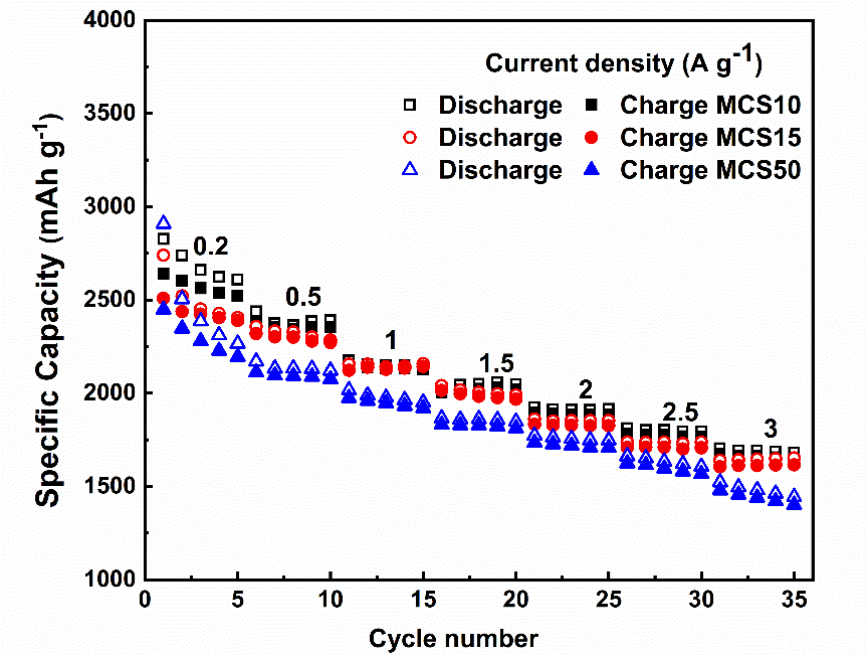

Figure 3.15 Rate performance of MCS10, MCS15, and MCS50 composite electrodes with 5 layers of MWCNTs/Cu NWs.

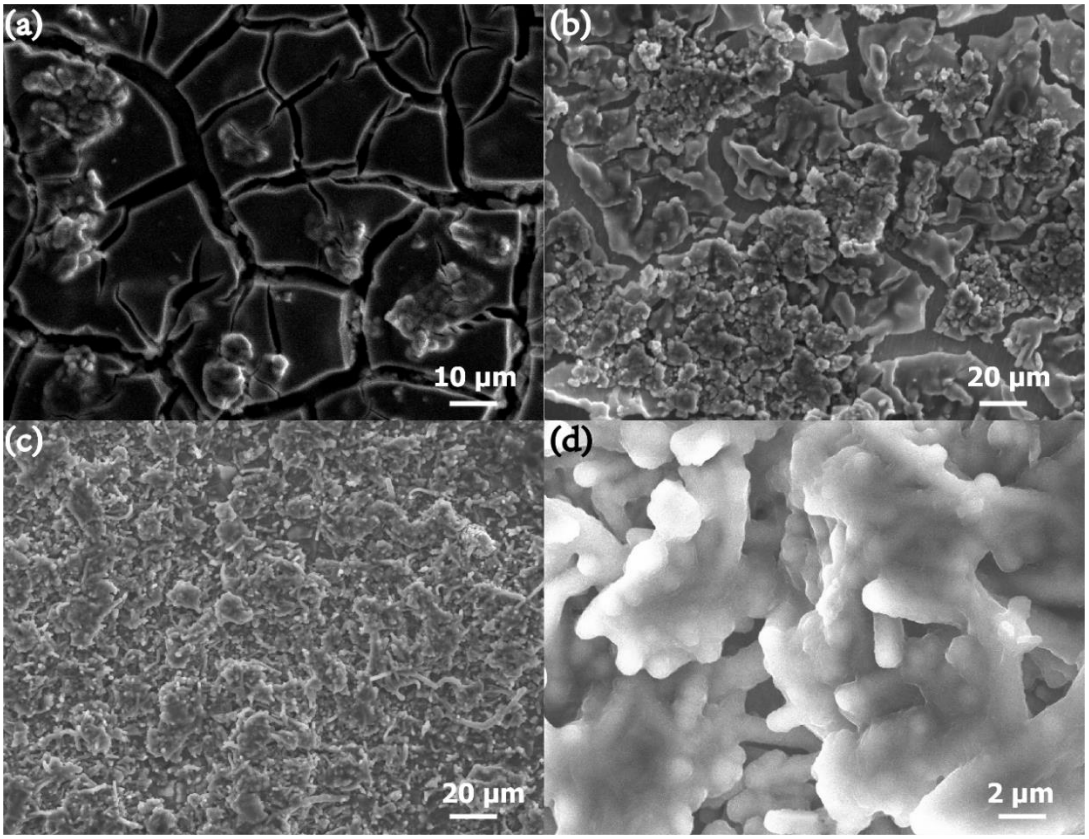

Figure 3.16 SEM images of 3D-structured PCS (a), PMS (b), and MCS10 (c-d) composite electrodes with 5 spin-coated layers after 100 cycles.

To further investigate the stable cycling performance of 3D composite electrodes, the PCS, PMS, and MCS10 anodes after 100 charge/discharge cycles were characterized by SEM in **Figure 3.16** (the corresponding SEM images before cycling are shown in **Figure 3.17**). As presented in **Figure 3.16a**, the PCS composite generates huge cracks, of which the width is approximately several micrometers. The exfoliation of active materials from the current collector indicates the electrical contact loss, which explains the rapid attenuation in the capacity of anodes after 100 cycles. By comparison, there are similar cracks on the PMS electrodes, but no obvious exfoliation is discovered in **Figure 3.16b**, which is attributed to the robust MWCNTs stabilizing the 3D structure of the electrode. Among these three 3D-structure electrodes, MCS10 maintains the original integrity and stability without significant deformation or breakages (**Figure 3.16c**). The partial enlarge view in **Figure 3.16d** demonstrates the stability of MWCNTs/Cu NWs/Si structure, indicating its efficiency to buffer the volume expansion of silicon.

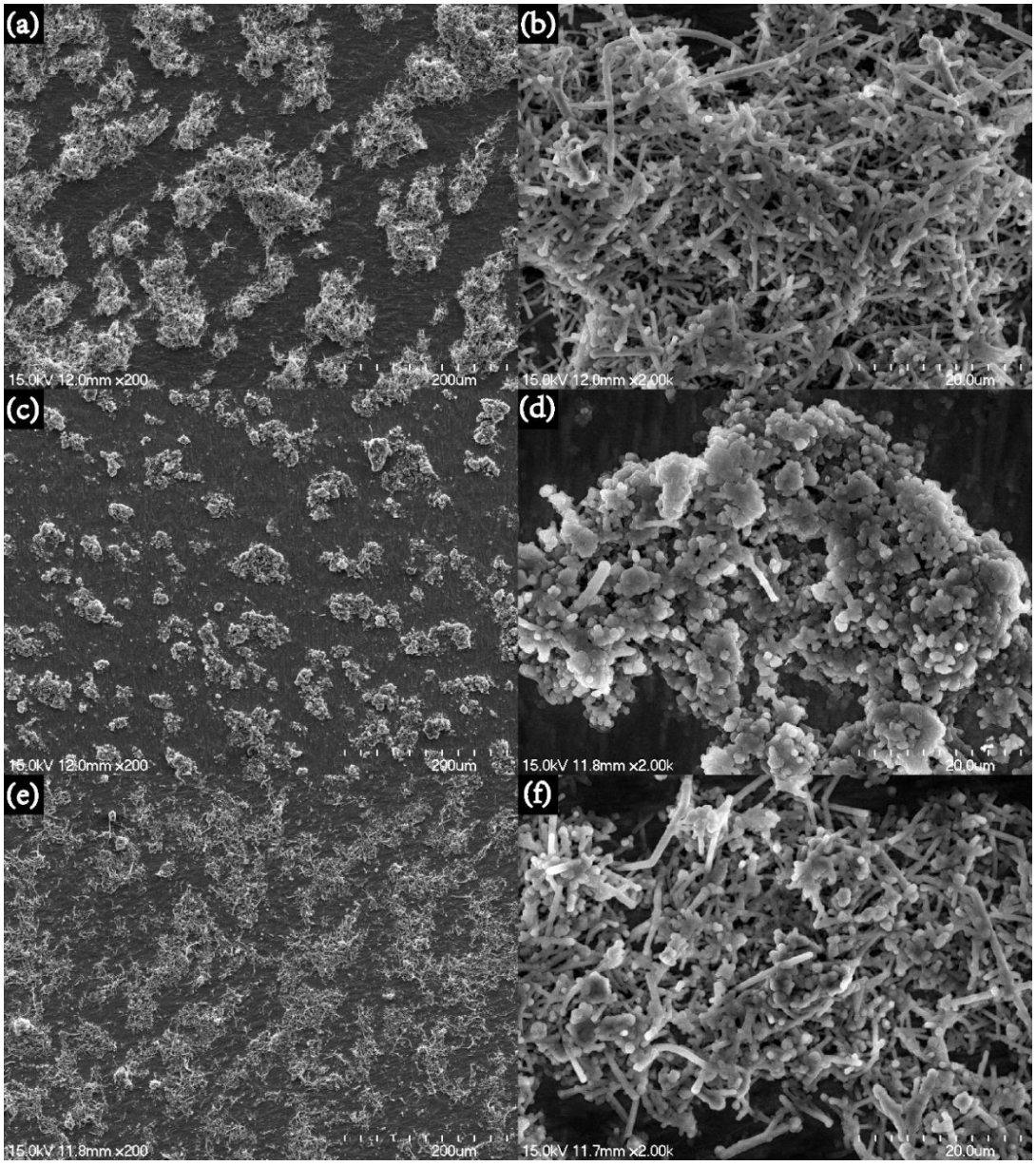

Figure 3.17 SEM images of 3D-structured PCS (a-b), PMS (c-d), and MCS10 (e-f) composite electrodes with 5 spin-coated layers at low and high magnification.

In general, the robust MWCNTs could strengthen the stability of the composite electrode; on the other hand, the superior conductivity of Cu NWs increases the specific capacity to a large extent. In addition, the concentration of MWCNTs is associated with the porosity factor of the current collector for Si deposition, which is critical for the

cyclic stability performance of the electrode. Among all electrodes with different weight ratios, the MCS10 electrode shows the best electrochemical performance, implying that the ratio of MWCNTs and Cu NWs achieves the optimized balance.

3.1 Conclusion

In conclusion, MWCNTs/Cu NWs/Si composites have been successfully fabricated by spin-coating and PECVD. The 3D MWCNTs/Cu NWs coated on the current collector serve as a matrix for Si deposition accommodating the volume change of Si during charge/discharge cycles and accelerating the transmission of Li ions between electrodes. The MWCNTs/Si and Cu/Si core-shell presents remarkable structural features with enhanced conductivity, shortened the Li-ions diffusion distance, and more active area for electrochemical reactions. As a consequence, MWCNTs/Cu NWs/Si composite electrode exhibits improved lithium storage properties in terms of high capacity, long cycle life, and excellent rate performance. All these results highlight that the rational selection and design of the MWCNTs/Cu NWs/Si composite electrode might allow it to be developed as an advanced anode material for LIBs.

3.2 References

[1] Y. Chang, M. L. Lye, and H. C. Zeng, "Large-Scale Synthesis of High-Quality Ultralong Copper Nanowires," *Langmuir,* vol. 21, no. 9, pp. 3746-3748, 2005.

[2] L. Lin, Y. Ma, Q. Xie, L. Wang, Q. Zhang, and D. Peng, "Copper-Nanoparticle-Induced Porous Si/Cu Composite Films as an Anode for Lithium Ion Batteries," *ACS Nano,* vol. 11, no. 7, pp. 6893-6903, 2017.

[3] D. B. Polat, O. Keles, and K. Amine, "Well-aligned, ordered, nanocolumnar, Cu–Si thin film as anode material for lithium-ion batteries," *Journal of Power Sources,* vol. 270, pp. 238-247, 2014.

[4] H. Wang, H. Song, Z. Lin, X. Jiang, X. Zhang, L. Yu, J. Xu, L. Pan, J. Wang, M. Zheng, Y. Shi, and K. Chen, "Highly Cross-Linked Cu/a-Si Core-Shell Nanowires for Ultra-Long Cycle Life and High Rate Lithium Batteries," *Nanoscale,* vol. 8, no. 5, pp. 2613-2619, 2016.

[5] H. Zhang, S. Jing, Y. Hu, H. Jiang, and C. Li, "A Flexible Freestanding Si/rGO Hybrid Film Anode for Stable Li-Ion Batteries," *Journal of Power Sources,* vol. 307, pp. 214-219, 2016.

[6] H. Wu and Y. Cui, "Designing Nanostructured Si Anodes for High Energy Lithium Ion Batteries," *Nano Today,* vol. 7, no. 5, pp. 414-429, 2012.

[7] Z. Yin, S. Cho, D. J. You, Y. k. Ahn, J. Yoo, and Y. S. Kim, "Copper Nanowire/Multi-Walled Carbon Nanotube Composites as All-Nanowire Flexible Electrode for Fast-Charging/Discharging Lithium-Ion Battery," *Nano Research,* vol. 11, no. 2, pp. 769-779, 2017.

[8] H. Wu, N. Du, H. Zhang, and D. Yang, "Voltage-Controlled Synthesis of Cu-Li_2O@Si Core-Shell Nanorod Arrays as High-Performance Anodes for Lithium-Ion Batteries," *Journal of Materials Chemistry A,* vol. 2, no. 48, pp. 20510-20514, 2014.

[9] Q. Zhang, H. Chen, L. Luo, B. Zhao, H. Luo, X. Han, J. Wang, C. Wang, Y. Yang, T. Zhu, and M. Liu, "Harnessing the Concurrent Reaction Dynamics in Active Si and Ge to Achieve High Performance Lithium-Ion Batteries," *Energy*

& Environmental Science, vol. 11, no. 3, pp. 669-681, 2018.

[10] H. Song, H. X. Wang, Z. Lin, X. Jiang, L. Yu, J. Xu, Z. Yu, X. Zhang, Y. Liu, P. He, L. Pan, Y. Shi, H. Zhou, and K. Chen, "Highly Connected Silicon–Copper Alloy Mixture Nanotubes as High-Rate and Durable Anode Materials for Lithium-Ion Batteries," *Advanced Functional Materials,* vol. 26, no. 4, pp. 524-531, 2016.

[11] M. Liu, X. Deng, Y. Ma, W. Xie, X. Hou, Y. Fu, and D. He, "Well-Designed Hierarchical Co_3O_4 Architecture as a Long-Life and Ultrahigh Rate Capacity Anode for Advanced Lithium-Ion Batteries," *Advanced Materials Interfaces,* vol. 4, no. 19, p. 1700553, 2017.

Chapter 4: Cu NWs/Si NPs@C as an anode material for lithium-ion batteries

4.1 Introduction

The one-dimensional Cu NWs have attracted significant attention in the field of energy storage for its high conductivity. In Chapter 3, it was demonstrated that the highly conductive Cu NWs applied in the electrode of Si-based LIBs could enhance the cycling performance by increasing the electrons diffusion efficiency. Besides, the porous structure of the current collector built by interlaced Cu NWs and MWCNTs can accommodate the huge volume change of the Si. Therefore, in Chapter 4, the further application of Cu NWs in the Si-based anode of LIBs has been investigated.

Here, Cu NWs were introduced to build a 3D conductive framework to support the Si NPs with carbon outer layers as a free-standing anode for LIBs. The Cu NWs/Si NPs@C composite electrode was obtained by annealing the Cu NWs/Si NPs@PVP hydrogel, which was prepared through freeze-drying the composite mixture, under H_2/Ar mixed gases. Concerning roles that Cu NWs play in the composite electrode, it could be concluded as follows: (1) 3D framework created by the intertwined Cu NWs accompanying the thin-film carbon shell not only allows the Si NPs to distribute uniformly but also provides efficient transmission pathway for electrons and ions. (2) The considerable interspace within the 3D structure can relieve the stress produced by the vast volume expansion of

Si NPs. In addition, the Cu NWs@C core-shell structure strengthens the stability of the 3D framework. Meanwhile, the carbon layer encapsulating Si NPs along Cu NWs enhances the contact between the Si NPs and Cu NWs, leading to excellent electrochemical performance of the Cu NWs/Si NPs@C composite electrode. As a result, the Cu NWs/Si NPs@C composite as an anode for LIBs exhibits a capacity of 2193 mAh g^{-1}. It remains 35% capacity after 80 charge and discharge cycles, which indicates the broad application potential of Cu NWs in the electrodes for LIBs.

4.2 Experimental section

4.2.1 Synthesis of Cu NWs

The synthesis of Cu NWs is similar to that in Chapter 3. 480 g NaOH, 1.6 g $CuSO_4 \cdot 5H_2O$, 6 mL EDA, and 1.072 mL N_2H_4 were mixed in a bottle glass bottle with 768 mL DI water in sequence. The mixture was stirred until a transparent and light blue solution was obtained. Subsequently, the bottle was sealed and left standing at 65 °C in an oil bath for 4 h, after which a slice of Cu NWs floating over the reaction solution. Eventually, the Cu NWs were collected and washed with deionized water and ethanol by centrifugation at 8500 rpm for 10 min. The average weight of the obtained Cu NWs, which had been dried in a vacuum oven at 80 °C for 12 h, was approximately 300 mg.

4.2.2 Fabrication of the Cu NWs/Si NPs @C aerogels

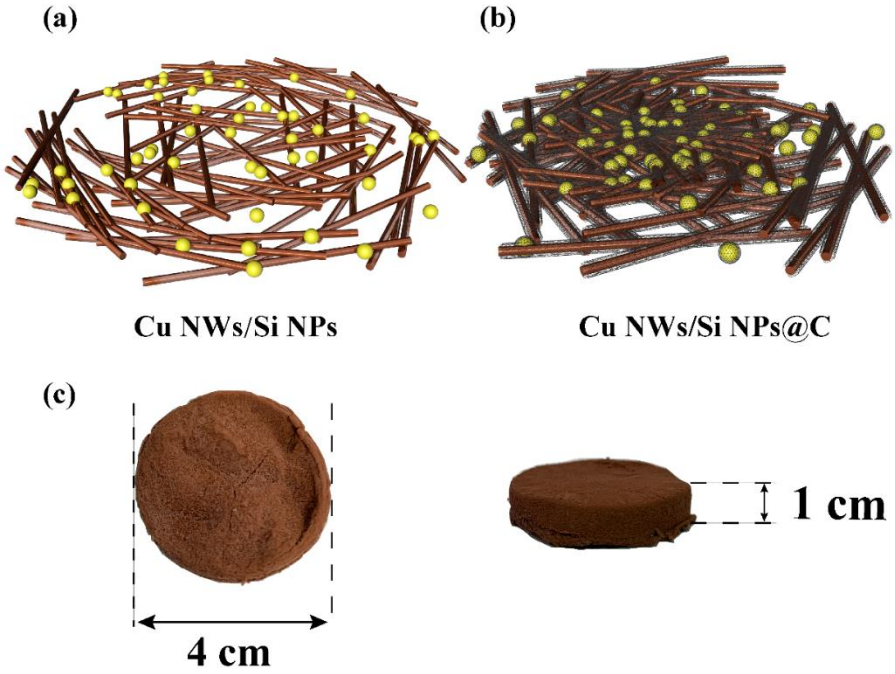

Figure 4.1 Scheme of making Cu NWs/Si NPs@C (Cu NWs: Si NPs=4/1) composite electrodes.

To fabricate the Cu NWs/Si NPs@C aerogels, the Cu NWs/Si NPs@PVP hydrogel was prepared in advance. 300 mg purified Cu NWs in ethanol (total volume of 4 mL) were mixed with 30 mL DI water to form a uniform suspension solution. Then, 75 mg Si powder with a diameter of 20-60 nm and 7.5 mL polyvinyl pyrrolidone (PVP, MW=130000) (25 mg/mL) were added into the above suspension with a further 24 h stirring to generate a homogeneous Cu NWs/Si NPs suspension. Each 12.5 mL mixed suspension was poured into a cylindrical silicone rubber mold (diameter=2 cm, height= 1 cm) and quickly frozen by liquid nitrogen. Then, the mold was transferred to a lyophilizer for freeze-drying about 24 h. The dried Cu NWs/Si NPs@PVP sample

remained the shape of the freeze-dried mold (**Figure 4.1c**). Finally, the dried cylindrical Cu NWs/Si NPs@PVP was annealed at 600 °C for 10 min under 1 slm of H_2/Ar (1:9) mixed atmosphere in a tube furnace. As a result, the Cu NWs/Si NPs@C aerogels were obtained, as shown in **Figure 4.1**. In addition, the samples with different mass ratios of Cu NWs and Si NPs, such as 1:4, 1:8, 1:10, 1:12, and 1:15, respectively, were prepared. Cu NWs@C aerogels were also fabricated as a control group.

4.3 Results and discussion

4.3.1 Characterization of Cu NWs/Si NPs@C

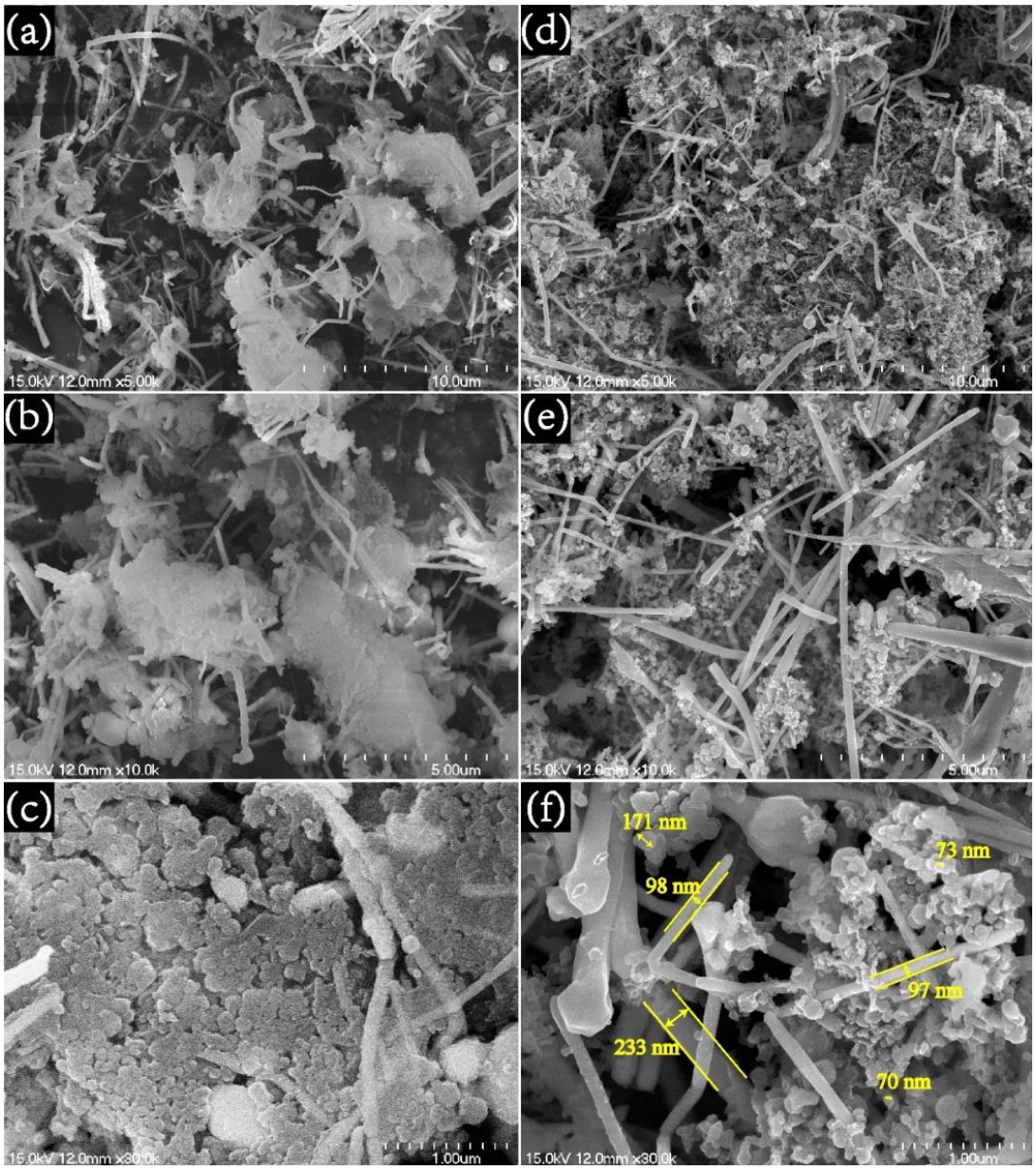

Figure 4.2 SEM images of Cu NWs/Si NPs@PVP (Cu NWs: Si NPs=4/1) (a-c) and Cu NWs/Si NPs@C (d-f) at various magnifications.

Figure 4.2 displays the SEM images of the Cu NWs/Si NPs@PVP and Cu NWs/Si NPs@C samples with Cu NWs: Si NPs=4/1. It is worth noting that the

Cu NWs/Si NPs@C composite was obtained by annealing the Cu NWs/Si NPs@PVP at 600 °C for 10 min under the atmosphere of H_2/Ar (1:9) in a tube furnace. In **Figure 4.2a-c**, it is found that Si NPs are encapsulated by the PVP in clusters without a precise outline. However, Cu NWs with high conductivity can be emerged in the SEM images, in which Cu NWs interlude within the cluster of PVP. After annealing in the mixed atmosphere of H_2 and Ar, the clusters disappeared, indicating that the polymer PVP was evaporated and partially transformed into a carbon thin film, which is inconspicuous in the SEM images. As displayed in **Figure 4.2d-f**, Si NPs are distributed within the 3D framework constructed by the Cu NWs. In **Figure 4.2f**, the diameter of the Cu NWs is mainly concentrated around 100 nm. By contrast, Si NPs have a diameter of ~70 nm. Due to the method of freeze-drying, the Cu NWs/Si NPs@PVP aerogels could retain the shape before drying as well as the shape after annealing (Cu NWs/Si NPs@C). Therefore, there is considerable interspace with the size ranging from 50 nm to 4 μm created by the interconnection of Cu NWs and Si NPs. The abundant interspace could be effectively used to accommodate the severe volume change of the Si active materials.

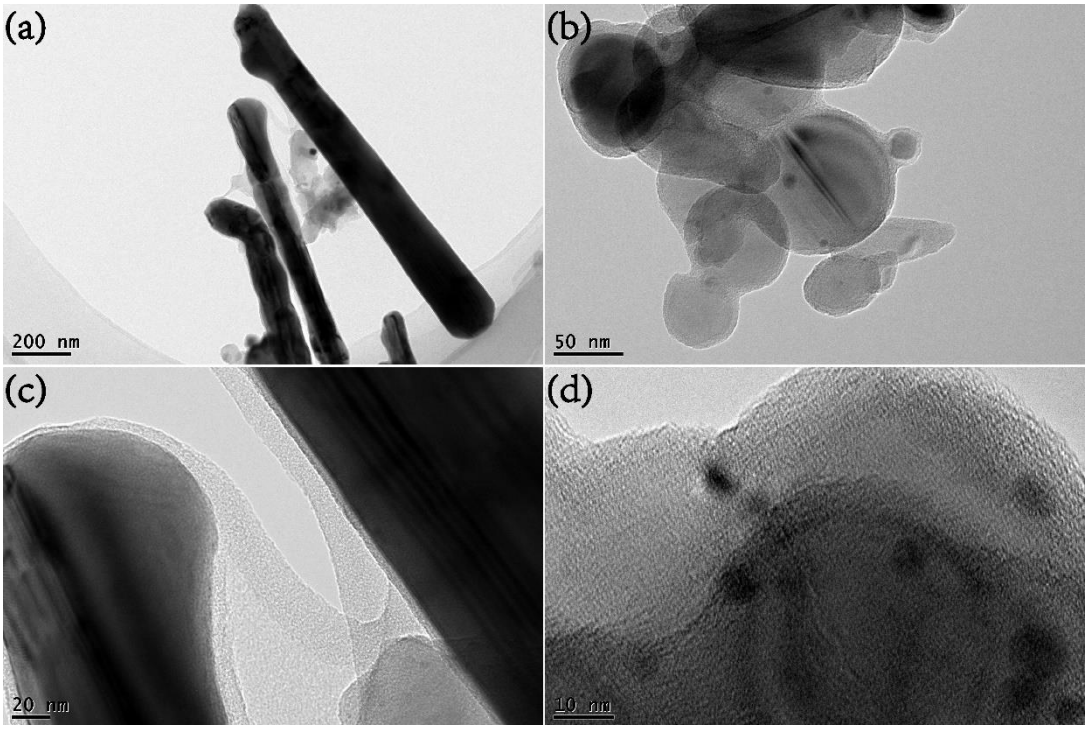

Figure 4.3 TEM images of the Cu NWs/Si NPs@C (Cu NWs: Si NPs=4/1, by weight) with different magnifications.

By comparison, the illustration of Cu NWs and Si NPs in the TEM is consistent with that in SEM images. Besides, the shape of Si NPs (20-60 nm diameter) becomes more apparent and is in coincidence with the product description (**Figure 4.3b**). If the Cu NWs/Si NPs@C samples are characterized by TEM images with larger magnification, the transform of PVP to carbon can be found. In **Figure 4.3c-d**, it is clear that a thin film encapsulates the Si NPs and Cu NWs at the same time. The thickness of the carbon thin film is estimated to 5-20 nm. In the Cu NWs/Si NPs@C composite, Cu NWs not only build the 3D framework to support the active materials but also increase the electrical conductivity of the whole electrode. The carbon thin-film shell functions as a coating layer encapsulating both the Si NPs and Cu NWs to strengthen the firmness of the 3D structure. Moreover, it plays a role in fixing the

Si NPs along the Cu NWs, by which Si NPs can uniformly distribute around the highly conductive Cu NWs. More importantly, the coating carbon layer with a thin thickness is beneficial to the diffusion efficiency of Li^+ in the composite electrode [1]. In **Figure 4.3c,** the carbon thin-film coats the surface of Cu NWs as well as connects the separated Cu NWs. In other words, the carbon thin film acts as a bridge for the electrons transferring between independent Cu NWs, which enhances the transmission efficiency of the electrons in the electrode.

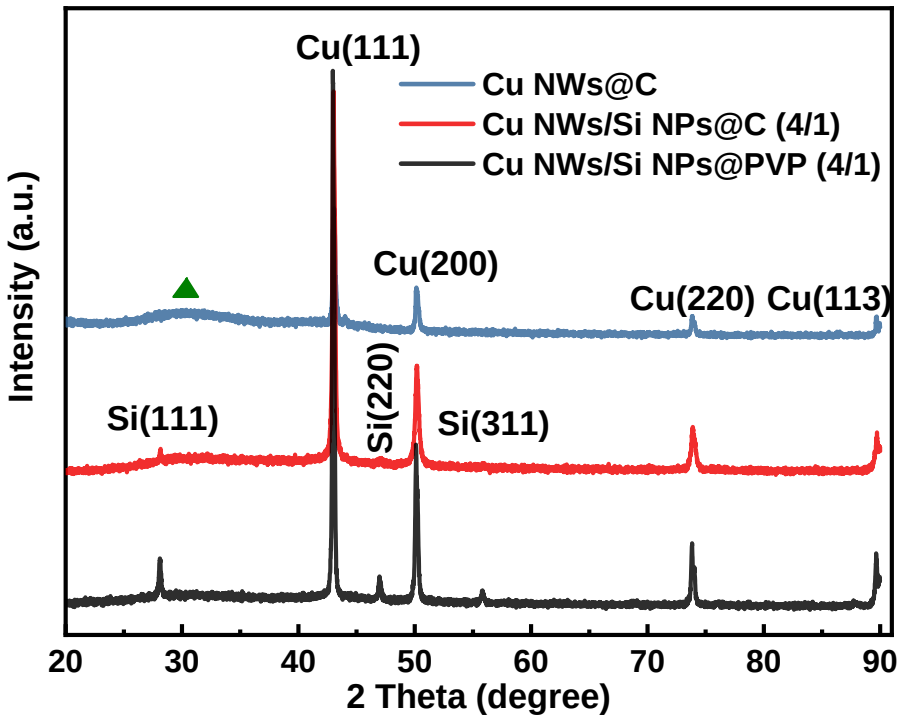

Figure 4.4 XRD patterns Cu NWs@C, Cu NWs/Si NPs@C (Cu NWs:Si NPs=4/1, by weight) , and Cu NWs/Si NPs@PVP (4/1).

XRD was conducted to characterize the crystal structure of the materials. **Figure 4.4** exhibits the XRD patterns of Cu NWs@C, Cu NWs/Si NPs@C, and Cu NWs/Si NPs@PVP with the mass ratio of Cu NWs and Si NPs as 4/1. The

Cu NWs@C sample was prepared by annealing the Cu NWs@PVP in the mixture gases (H_2/Ar). The dominant characteristic diffraction peaks around 43.00°, 50.13°, 73.89°, and 89.74° correspond to the (111), (200), (220), and (311) planes of Cu (PDF No. 04-0836), respectively [2]. The crystalline structure of Cu NWs maintains unchanged before or after the annealing process. Furthermore, there is a broad peak locating at 25-35°, which is ascribed to the formation of the carbon thin film transferred from the polymer PVP [3]. A similar phenomenon also occurs in the XRD pattern of Cu NWs/Si NPs@C. In addition, three distinct peaks related to Si are shown at 28.15°, 47.11°, and 55.90° that are consistent with the (111), (220), and (311) lattice planes of cubic Si (PDF No.27-1402) [4], which indicates the Si powder is crystalline.

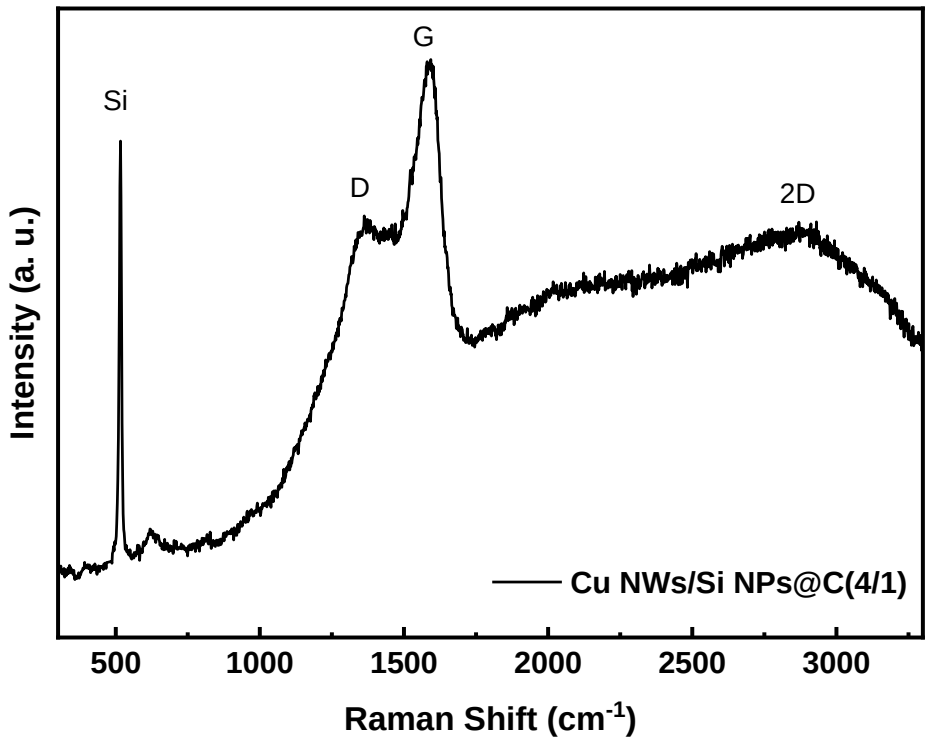

Figure 4.5 Raman spectra of Cu NWs/Si NPs@C (Cu NWs/Si NPs=4/1, by weight) composite electrode.

The Raman spectra of Cu NWs/Si NPs@C (Cu NWs/Si NPs=4/1, by weight) composite consists of two categories bands corresponding to silicon and carbon, respectively. For instance, the band at 516.54 cm^{-1} is associated with the Raman scattering of the photon from the Si-Si stretching vibrations [4, 5]. Moreover, a G band emerges at 1593 cm^{-1}, and a broad 2D band is observed at 2750-3250 cm^{-1}, which can be regarded as the representative bands demonstrating the graphitic outer layers. The G band is attributed to the C-C stretching [6], while the 2D band is a symbol indicating the graphitic sp^2 materials [7]. It is usually used to probe the number of layers of graphene. The low intensity of the 2D band indicates bulk graphite, which has multilayers of graphene [8]. Besides, the disorder of sp^2-hybridized carbon gives rise to a D band at 1362.29 cm^{-1}. Hence, the intensity of the D band correlates to the defects in the graphitic materials.

4.3.2 Electrochemical performance of Cu NWs/Si NPs@C

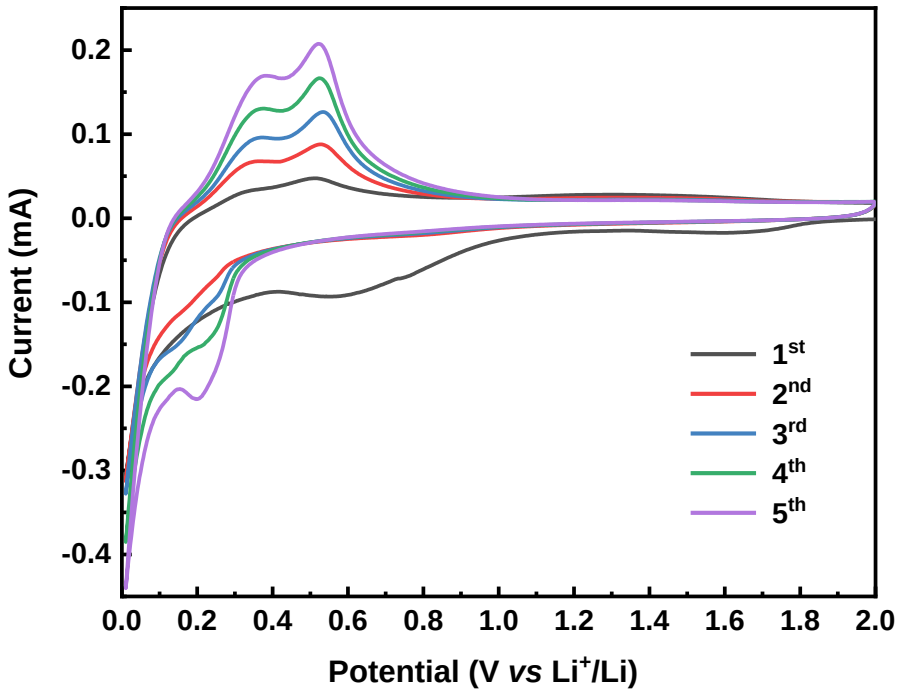

Figure 4.6 Cyclic voltammetry (CV) curves of Cu NWs/Si NPs@C (Cu NWs: Si NPs=4/1, by weight) with the initial five cycles.

The CV of the Cu NWs/Si NPs@C composite electrode was conducted to investigate the electrochemical reaction during the discharge and charge processes, as shown in **Figure 4.6**. The CV curves of the initial five cycles were obtained by testing the as-prepared coin cell at a scan rate of 0.1 mV s^{-1} with a scanning voltage range of 0.001-2 V. During the first cathodic scan, a broad peak occurs at the 0.5-0.8 V, which arises from the decomposition of electrolyte and the formation of SEI layers on the surface of active material. The peak disappears at the following cycles revealing the irreversible reaction. Then, a broad peak around 0.03 V is ascribed to the lithiation of the crystalline Si, accompanying the transmission of Si structure to amorphous Li_xSi and further crystalline $Li_{15}Si_4$. At the following cathodic scans, two distinct peaks at

0.2 and 0.03 V are attributed to the lithiation process of amorphous Si, into which Li^+ insert forming the amorphous Li_xSi and crystalline $Li_{15}Si_4$ by step. On the contrary, during the first anodic scan, there are also two peaks at 0.44 and 0.52 V, which correspond to the oxidation of $Li_{15}Si_4$ to Li_xSi and the further dealloying Li_xSi to amorphous Si instead of crystalline Si. Concerning both cathodic and anodic scan, the intensity of peaks is enlarged for the following cycles due to the enhanced alloying and de-alloying level [1].

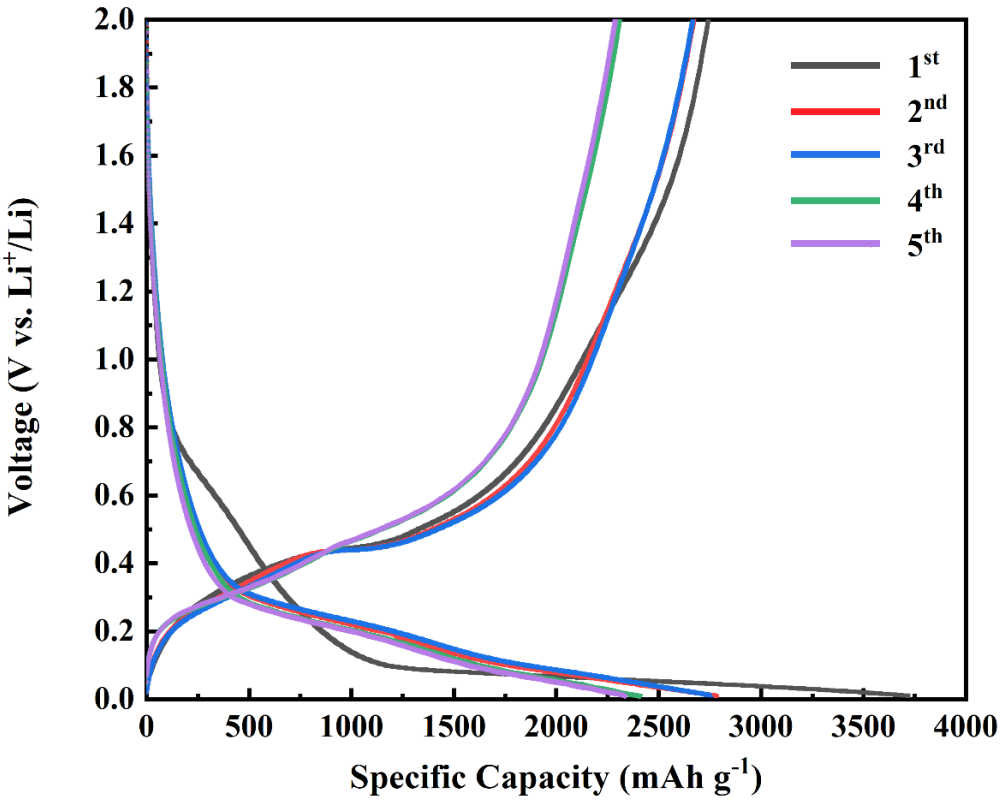

Figure 4.7 Charge/discharge profiles of Cu NWs/Si NPs@C (Cu NWs: Si NPs=15/1, by weight) composite electrode with the initial three cycles at the current density of 0.05 C and following two cycles at the current density of 0.2 C (C=4200 mA g^{-1}).

The charge/discharge voltage profiles of Cu NWs/Si NPs@C composite electrode with the mass ratio of Cu NWs: Si NPs=15/1 were exhibited in **Figure 4.7**. The working potentials for redox reactions at different stages are consistent with that shown in CV curves (Figure 4.8). During the first discharge process, a steady working plateau is in the range of 0.08-0.01 V, indicating the lithiation of crystalline Si [9]. During the following discharge processes, the working potential separates into two stages, around ~0.2 and 0.03 V, due to the amorphization of crystalline Si during the first discharging process. By comparison, during the charging process, the apparent working voltages locating at ~0.4 and 0.55 V corresponds to the delithiation processes, where the crystalline $Li_{15}Si_4$ changes to Li_xSi and finally products amorphous Si. Moreover, the charge/discharge profiles exhibit the initial discharge and charge capacities of 3718 and 2740 mAh g^{-1}, respectively, implying the initial Coulombic efficiency of 74 %. The capacity loss is attributed to the decomposition of electrolyte and the generation of SEI films on the surface of the composite electrode.

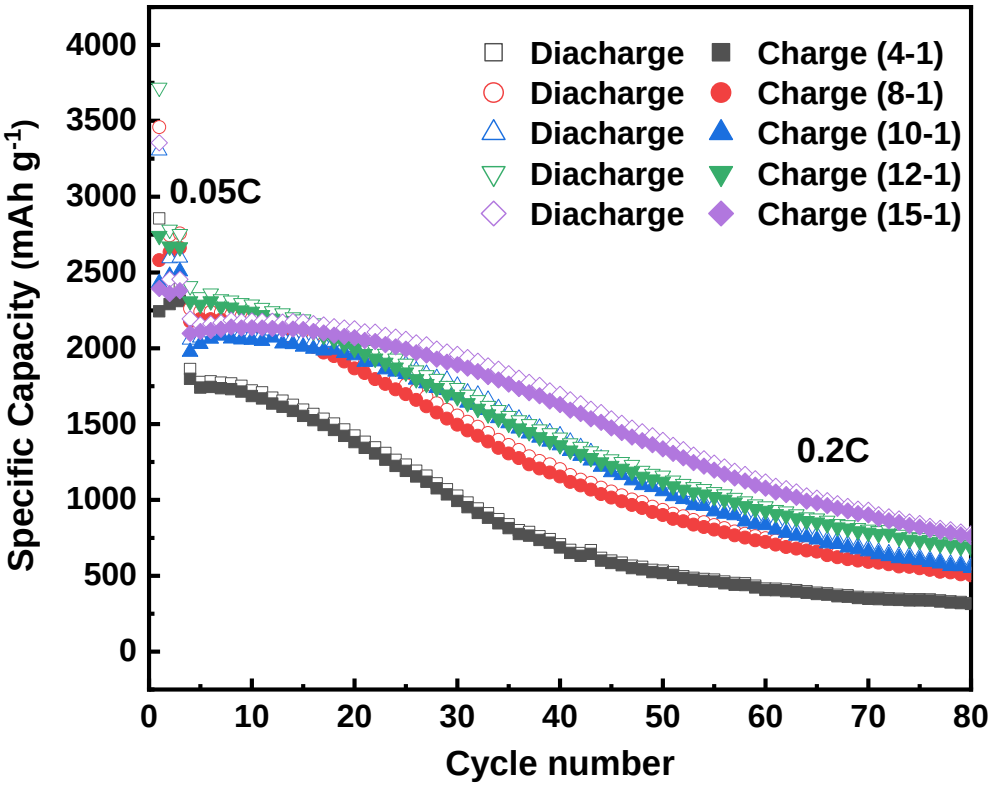

Figure 4.8 Cycling performance Cu NWs/Si NPs@C composite electrode with the mass ratio of Cu NWs/Si NPs=4:1, 8:1, 10:1, 12:1, and 15:1 at the current density of 0.2 C with three initial cycles at the current density of 0.05 C (C=4200 mA g^{-1}).

Figure 4.8 compares the cycling performance of the Cu NWs/Si NPs@C composite electrode with the different mass ratios of Cu NWs and Si NPs, such as Cu NWs/Si NPs =4:1, 8:1, 10:1, 12:1, and 15:1. The average mass loading of the active materials of the Cu NWs/Si NPs@C composite electrode with different concentrations distributes in the range of 0.9-1.2 mg cm^{-2}. Interesting, the cycling performance is enhanced when the content of active materials is reduced in the whole electrode. For instance, the Cu NWs/Si NPs@C composite electrode (Cu NWs/Si NPs=15:1) exhibits a specific capacity of 2193 mAh g^{-1} at the fourth cycle after the pre-cycling while the

Cu NWs/Si NPs@C composite electrode (Cu NWs/Si NPs=4:1) shows a lower capacity around 1862 mAh g^{-1}. Until the 80^{th} cycle, two electrodes remain 35 % and 17 % capacity, respectively. The faster capacity fading of the Cu NWs/Si NPs@C with a higher mass ratio of Cu NWs and Si NPs reveals that the large mass of active materials loaded along the Cu NWs causes the unstable structure of the whole electrode. Besides, the large number of active materials leading to tremendous strain among the Si NP, which leads to the considerable volume change of the entire electrode. Similarly, it is possible for the poles created by Cu NWs to be filled up by a more massive amount of Si NPs, which presumes that there is interspace to accommodate the volume change of the active materials. Therefore, the Cu NWs/Si NPs@C composite electrodes with the larger mass ratios of Cu NWs and Si NPs exhibit inferior cycling performance.

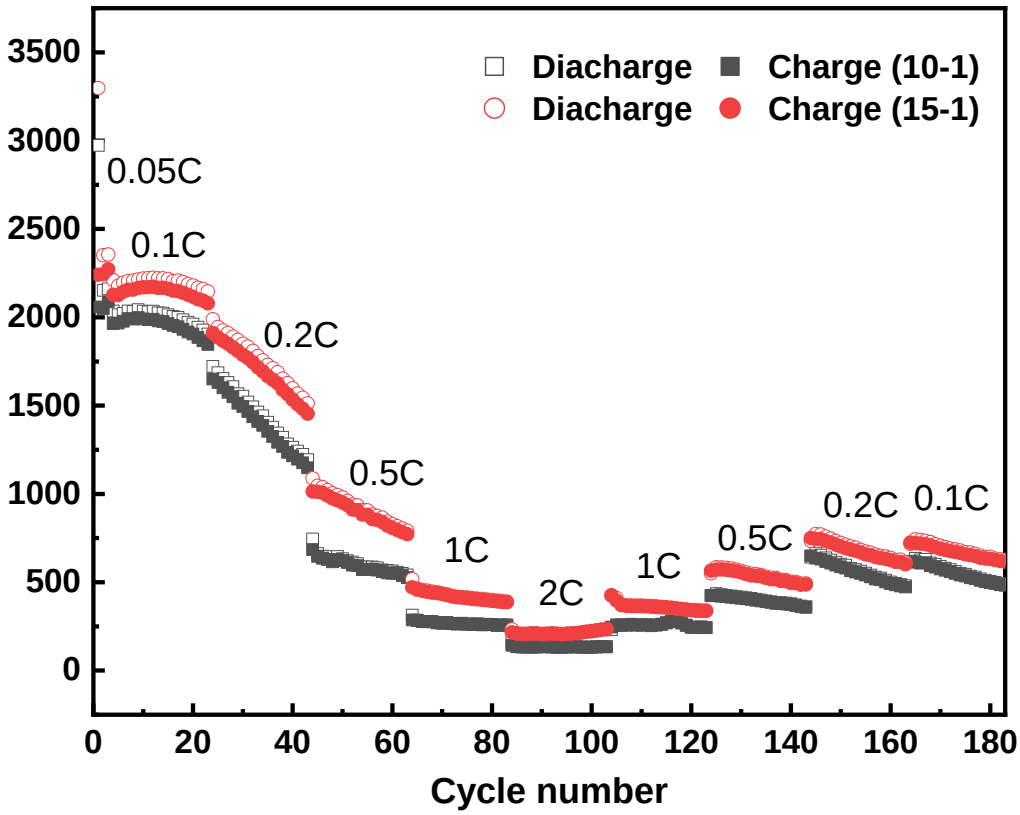

Figure 4.9 Rate capability of the Cu NWs/Si NPs@C composite electrode with the mass ratio of Cu NWs/Si NPs=10:1 and 15:1 at the current densities.

The rate capability of the Cu NWs/Si NPs@C composite electrode with the mass ratio of Cu NWs/Si NPs=10:1 and 15:1 at the various current densities was conducted. The current density started from 0.05 C for three pre-cycles and was set as 0.2 C, 0.5 C, 1 C, and 2 C (20 cycles for each stage). Then, the current density returned to 0.1 C with reverse stages. Compared with the Cu NWs/Si NPs@C composite electrode with the mass ratio of Cu NWs/Si NPs=10:1, one with the mass ratio of Cu NWs/Si NPs =15:1 exhibits the superior specific capacities corresponding to each current density and higher capacity retention. The main reason causing the better rate performance is the larger content of Cu NWs in the Cu NWs/Si NPs@C composite, which increases the

electrical conductivity of the whole electrode. On the other hand, the smaller concentration of Si NPs in the composite has little effect on the diffusion efficiency of Li^+ in the electrodes. Therefore, the Cu NWs/Si NPs@C composite electrode (Cu NWs/Si NPs=15:1) exhibits a higher capacity at larger current densities.

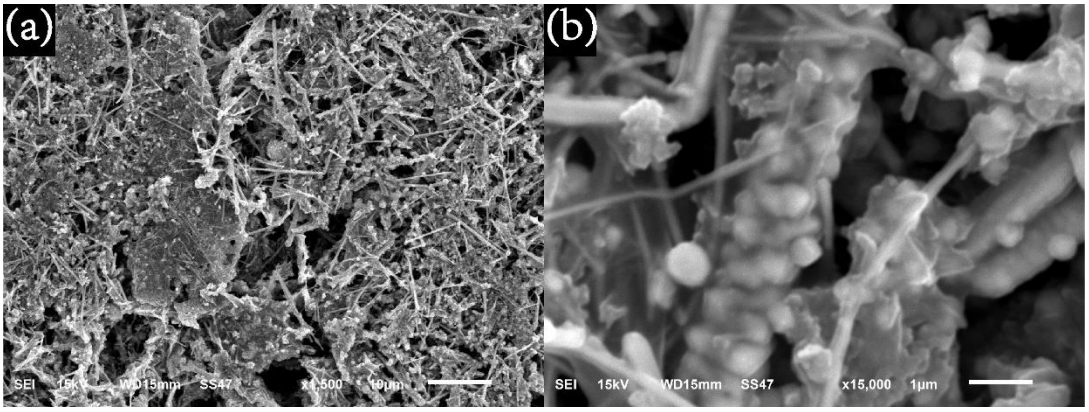

Figure 4.10 (a-b) SEM images of the Cu NWs/Si NPs@C composite electrode with the mass ratio of Cu NWs/Si NPs= 15:1 after 100 cycles with different magnifications.

Commonly, the morphology and structure of the electrode after long-term cycling are characterized by SEM to investigate the structural stability of the electrode. Thus, after cycling, the coin-cell was dismantled in the gloves box under the atmosphere. The composite electrode was washed by DMC and dried in the gloves box for 24 hours. **Figure 4.10** displays the morphology of the Cu NWs/Si NPs@C composite electrode (Cu NWs/Si NPs= 15:1) after 100 cycles at the current of 0.2 C. It is worth noting that the SEI layers were observed covering the surface of the composite materials. Under larger magnification, it is clear to find that considerable Si NPs still attach the continuous Cu NWs, which indicate the stable structure of the composite electrode.

4.4 Conclusion

To summarize, the Cu NWs/Si NPs@C composite electrode prepared by freeze-drying and annealing the Cu NWs/Si NPs@PVP hydrogel. The free-standing electrode is supported by a 3D highly conductive framework consisting of the intertwined Cu NWs and the thin carbon shell, which encapsulates Si NPs along the Cu NWs. Both Cu NWs and the carbon layer enhance the electrical conductivity of the electrode, bringing about an excellent rate capability. The interspace created by the Cu NWs accompanying the protection of carbon shell accommodates the vast volume change of the active materials, leading to stable cycling performance.

4.5 References

[1] X. Ding, H. Wang, X. Liu, Z. Gao, Y. Huang, D. Lv, P. He, and Y. Huang, "Advanced Anodes Composed of Graphene Encapsulated Nano-Silicon in a Carbon Nanotube Network," *RSC Advances,* vol. 7, no. 26, pp. 15694-15701, 2017.

[2] Y. Chang, M. L. Lye, and H. C. Zeng, "Large-Scale Synthesis of High-Quality Ultralong Copper Nanowires," *Langmuir,* vol. 21, no. 9, pp. 3746-3748, 2005.

[3] S. Wu, L. Yang, M. Zou, Y. Yang, M. Du, W. Xu, L. Yang, Y. Fang, and A. Cao, "Blown-Bubble Assembly and in Situ Fabrication of Sausage-like Graphene Nanotubes Containing Copper Nanoblocks," *Nano Letters,* vol. 16, no. 8, pp. 4917-4924, 2016.

[4] N. Lin, Y. Han, J. Zhou, K. Zhang, T. Xu, Y. Zhu, and Y. Qian, "A Low Temperature Molten Salt Process for Aluminothermic Reduction of Silicon Oxides to Crystalline Si for Li-Ion Batteries," *Energy & Environmental Science,* vol. 8, no. 11, pp. 3187-3191, 2015.

[5] J. Zi, H. Büscher, C. Falter, W. Ludwig, K. Zhang, and X. Xie, "Raman Shifts in Si Nanocrystals," *Applied Physics Letters,* vol. 69, no. 2, pp. 200-202, 1996.

[6] Z. H. Ni, T. Yu, Y. H. Lu, Y. Y. Wang, Y. P. Feng, and Z. X. Shen, "Uniaxial Strain on Graphene: Raman Spectroscopy Study and Band-Gap Opening," *ACS Nano,* vol. 2, no. 11, pp. 2301-2305, 2008.

[7] M. S. Dresselhaus, A. Jorio, M. Hofmann, G. Dresselhaus, and R. Saito, "Perspectives on Carbon Nanotubes and Graphene Raman Spectroscopy," *Nano Letters,* vol. 10, no. 3, pp. 751-758, 2010.

[8] A. C. Ferrari, "Raman Spectroscopy of Graphene and Graphite: Disorder, Electron–Phonon Coupling, Doping and Nonadiabatic Effects," *Solid State Communications,* vol. 143, no. 1, pp. 47-57, 2007.

[9] L. F. Cui, R. Ruffo, C. K. Chan, H. Peng, and Y. Cui, "Crystalline-Amorphous Core-Shell Silicon Nanowires for High Capacity and High Current Battery Electrodes," *Nano Lett,* vol. 9, no. 1, pp. 491-5, 2009.

Chapter 5: Co_3O_4/MXene as anode materials for lithium-ion batteries

5.1 Introduction

In Chapter 5, MXenes were used to improve the electrochemical performance of anodes for LIBs. An analog as graphene, this two-dimensional (2D) layered material with the structure of transition metal carbides or nitrides exhibits superior electronic conductivity, large interlayer spacing for highly efficient lithium ions diffusion pathways and environmental benignity, making it useful as energy storage material. However, the inferior capability to store lithium ions impedes its wide application as active materials in lithium-ion batteries. Therefore, Feng et al. fabricated a flexible and free-standing electrode of Si/MXene composite, which exhibited superior electrochemical performance with a specific capacity of 1672 mAh g^{-1} at 1 A g^{-1} after 200 cycles [1]. In Chapter 5, MXene has been chosen to construct a 3D highly conductive framework to support active materials (Co_3O_4). Compared with Chapter 3 and Chapter 4, in which one-dimensional (1D) highly conductive Cu NWs cooperating with carbon materials to enhances the electrochemical performance of anodes for LIBs, 2D high conductive MXene nanosheets have an advantage in a more strengthened structure for the anode in Chapter 5. Moreover, Co_3O_4 nanoparticles were used as active materials and prepared by a controllable preparation process.

Therefore, a facile strategy for preparing Co_3O_4 nanoparticles incorporated with MXene nanosheets on Ni foams has been developed. Four distinguishing features were

achieved for this Co_3O_4/MXene composite electrode: (i) The large interlayer spacing of MXene nanosheets allows the Co_3O_4 nanoparticles to distribute uniformly, functioning as a flexible buffer to restrain the volume expansion. (ii) The intercalation of Co_3O_4 in MXene nanosheets prevents not only the agglomeration of Co_3O_4 nanoparticles but also the stacking of MXene nanosheets. (iii) The MXene provides a 3D framework to enhance electrons and Li^+ transmission efficiency. (iv) The mass loading of anode materials on Ni foam increases significantly due to the considerable Co_3O_4 nanoparticles attached to the MXene nanosheets, which offers a large surface area in the nanoscale. As a result, the Co_3O_4/MXene composite as an anode for LIBs delivered 1005 mAh g^{-1} capacity after 300 cycles at the current density of 1 C and remained a stable capacity of 307 mAh g^{-1} at the current density of 5 C after 1000 cycles, displaying outstanding electrochemical performance with superior reversible capacity and excellent cycling stability and rate capability.

5.2 Experimental section

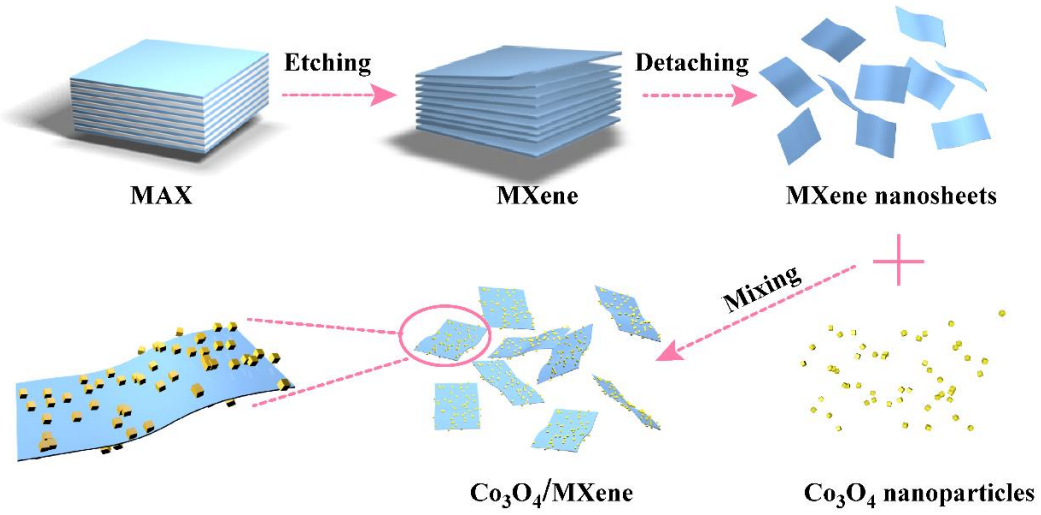

Figure 5.1 Schematic illustration for the synthesis procedure of Co_3O_4/MXene composite.

5.2.1 Delamination of MXene

To prepare a homogeneous delaminated $Ti_3C_2T_x$ suspension, 2 g Ti_3AlC_2 powders (200 mesh, 11 Technology Co., Ltd) were slowly added to the prepared suspension in which 2 g LiF mixed with 40 mL HCl (9 M) in a Teflon beaker with stirring for 30 min [2]. Then, the above suspension was kept at 35 ℃ under magnetic stirring for 24 h. The resultant suspension was washed using distilled water accompanied by sonication for 10 min and centrifugation (3500 rpm, 10 min) for many times to remove the residual impurities and HF until the pH of supernatant approaching 6. Then, the sediment was dispersed in ethanol that functioned as an intercalation agent and sonicated for 1.5 h followed by centrifugation (10000 rpm, 10 min). Finally, the homogeneous delaminated $Ti_3C_2T_x$ suspension was prepared by repeatedly collecting the supernatant

after centrifugation (3500 rpm,10 min) in which the above sediment was mixed with 20 mL DI water under sonication for 20 min.

5.2.2 Synthesis of Co_3O_4 nanoparticles

The Co_3O_4 nanoparticles were synthesized with reference to Prof. Peng's method [3]. 797 mg $Co(CH_3COO)_2 \cdot 4H_2O$ (Aladdin Industrial Corporation, China) was dissolved in 16 mL DI water followed by stirring, which afterward was slowly dropped into the 160 mL ethanol and stirred for 2 h. The uniform mixture was poured into a 200 mL Teflon-line steel autoclave and heated at 120 ℃ in a muffle furnace for 8 h. The black precipitate was centrifuged four times using ethanol dispersant. Eventually, Co_3O_4 nanoparticles were sent into a vacuum oven and kept at 80 ℃ for 12 h.

5.2.3 Fabrication of Co_3O_4/MXene composite electrodes

50 mg as-prepared Co_3O_4 nanoparticles were dispersed in 5 mL ethanol under sonication for 20 min. Then, 5 mL MXene suspension (10 mg/mL) was added into the above suspension, which was stirred for 6 h subsequently. The Co_3O_4/MXene composite electrodes were fabricated by dropping the uniform Co_3O_4/MXene suspension onto the Ni foams (13 mm diameter). In order to obtain the composite electrodes with different mass loading, the above steps were repeated at different times. The composite electrodes were dried in vacuum at 60 ℃ for 12 h and at 120 ℃ for 3 h. After cooling down to room temperature, these electrodes were sent to the glove box to be assembled into the coin cells. To investigate the effect of different ratios of Co_3O_4 and MXene on the electrochemical performance of LIBs, the ratio was designed,

including Co_3O_4/MXene =1:2, 1:1, 2:1, and 4:1, labeled as COMX0.5, COMX1, COMX2, and COMX4, respectively. Besides, the control groups were obtained by individually dropping the pure Co_3O_4 and pure MXene suspension on the Ni foams.

5.3 Results and discussion

5.3.1 Characterization of Co_3O_4/MXene composite

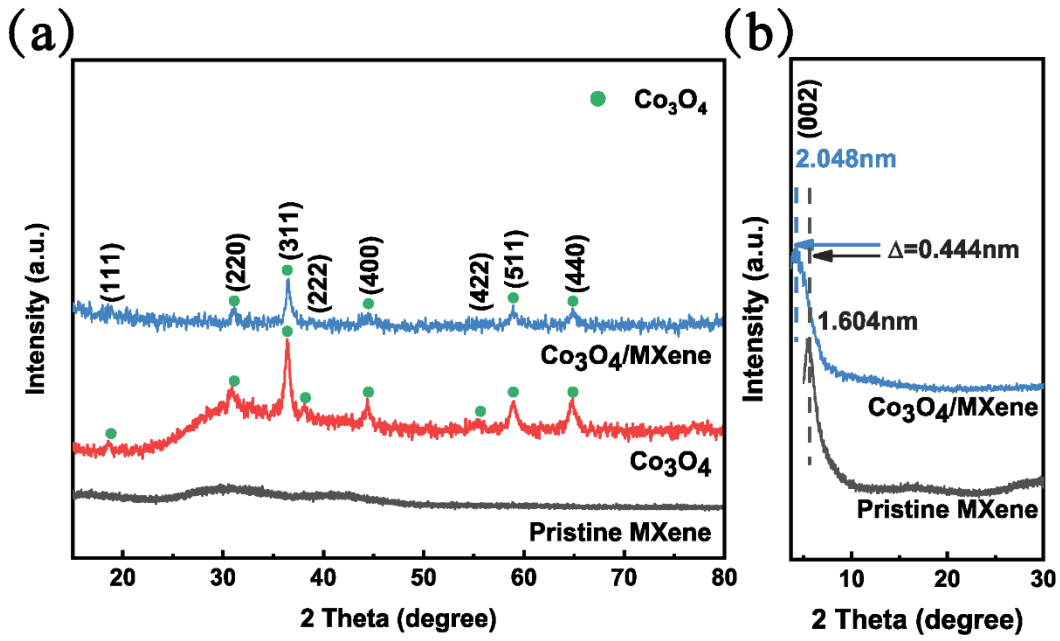

Figure 5.2 (a) XRD patterns of Co_3O_4/MXene composite with the ratio of Co_3O_4/MXene=2:1 (COMX2), Co_3O_4 nanoparticles, and MXene nanosheets. (b) XRD patterns of COMX2 and MXene nanosheets.

To further illustrate the crystal structure and morphology of the samples, the XRD patterns of Co_3O_4/MXene composite, Co_3O_4 nanoparticles, and MXene nanosheets, are presented in **Figure 5.2a**. The prominent diffraction peaks at 18.9°, 31.2°, 36.8°, 38.5°, 44.9°, 55.6°, 59.5°, and 65.3° are respectively indexed to the (111), (220), (311), (222),

(400), (422), (511), and (440) planes of Co_3O_4 nanoparticles (PDF No. 43-1003). A prominent peak at 5.504° is associated with the MXene phase (002) [1], authenticating the successful delamination of MXene nanosheets, as shown in **Figure 5.2b** [4, 5]. The characteristic peaks of both Co_3O_4 and MXene are exhibited in the XRD pattern of Co_3O_4/MXene composite. Interestingly, the main peak (002) of MXene down-shifts to a smaller angle of 2θ=4.31°, indicating the expansion of the MXene nanosheets along the c-axis with the increased interlayer spacing of 2.05 nm according to Bragg's equation [6-8]. Both the intensity weakening and down-shift of (002) peak are attributed to the intercalation of Co_3O_4 nanoparticles between the MXene interlayers. The resultant larger MXene interlayer spacing is beneficial for not only accommodating the huge volume change of Co_3O_4 nanoparticles but also improving the Li^+ diffusion efficiency with more electrolyte reaching Co_3O_4 nanoparticles [9].

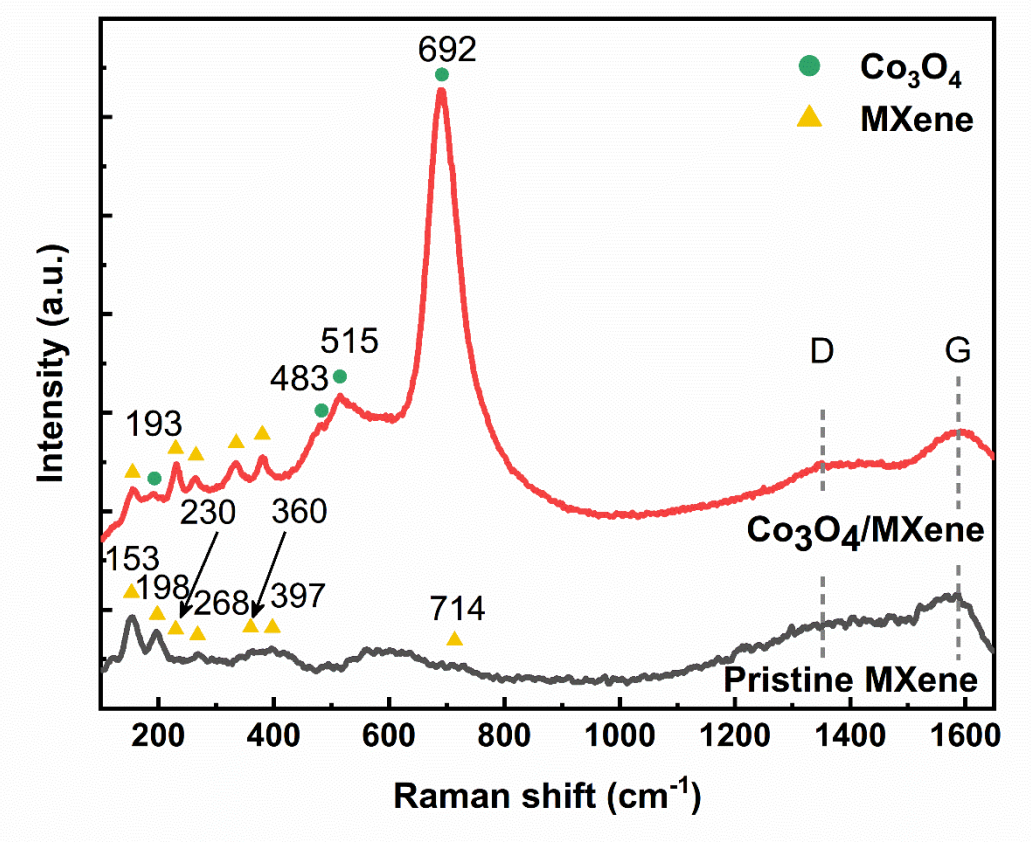

Figure 5.3 Raman spectra of COMX2 and MXene nanosheets.

Raman spectra (**Figure 5.3**) provides additional information about the surface structure of the Co_3O_4/MXene composite. The characteristic bands of both Co_3O_4 nanoparticles and MXene nanosheets were exhibited in the composite. There are two board peaks around 1350 cm^{-1} (D band) and 1585 cm^{-1} (G band) for graphitic carbon. The I_D/I_G ratio for Co_3O_4/MXene composite about 0.73 is slightly larger than that of pristine MXene nanosheets, implying the attenuated graphitization degree of carbon due to the incorporation of Co_3O_4 nanoparticles [10, 11]. Four peaks around 193, 483, 515, and 692 cm^{-1} (labeled with green circles) in the spectrum of the composite are respectively indexed to the F_{2g}, E_g, F^1_{2g}, and A_{1g} Raman-active modes of the crystalline Co_3O_4 [12-14]. By comparison, the characteristic peaks corresponding to MXene are

labeled with yellow triangles. The band at 153 cm^{-1} is related to the Ti-O stretching vibration indicating the oxidation of MXene [15, 16]. In addition, the peaks located at 198 and 714 cm^{-1} correspond to A_{1g} symmetry out-of-plane oscillations of Ti and C atoms, while the peaks around 268, 397, and 605 cm^{-1} resulting from the oscillations of E_g group, including in-plane (shear) modes of Ti, C, and surface functional group atoms [11], [17, 18].

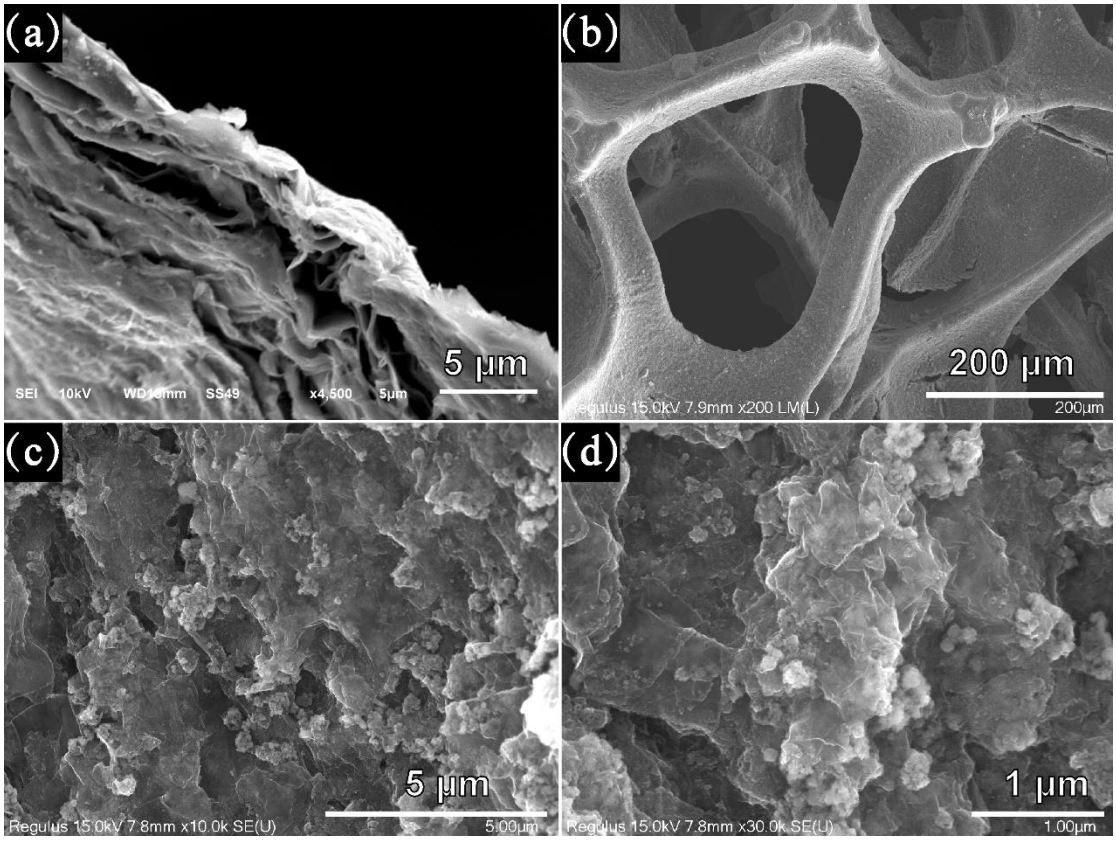

Figure 5.4 SEM of (a) MXene nanosheets and (b-d) Co_3O_4/MXene composite on Ni foam with the ratio of Co_3O_4/MXene=1:1 (COMX1) with various magnifications.

Figure 5.4 shows the morphology of the pure MXene nanosheets and the Co_3O_4/MXene composite on Ni foams. As displayed in **Figure 5.4a**, MXene nanosheets are stacked together with a fluctuant plane, revealing that the flexible MXene could release the strain caused by the volume expansion of Co_3O_4 nanoparticles during the lithiation process. Moreover, the distinct interlayer spacing demonstrates the successful delamination of the MXene nanosheets. The large interlayer spacing is desired to increase the mass loading of active materials and provide more room to accommodate the expansion of active materials. The composite electrode was prepared by coating the Co_3O_4/MXene mixture on Ni foam, as shown in **Figure 5.4b**. The Co_3O_4/MXene mixture covers the surface of Ni foam along with the skeleton as well as partially fills the hole enclosed by the frames, which implies the sufficient contact between the active material with the current collector. In the larger magnification (**Figure 5.4c-d**), Co_3O_4 nanoparticles are uniformly distributed within the MXene nanosheets. On the other hand, Co_3O_4 nanoparticles can be considered as encapsulated by the MXene nanosheets. In comparison with COMX1, there are more agglomerations for COMX4 due to the higher percentage of the Co_3O_4 nanoparticles leading to the ununiform distribution, as displayed in **Figure 5.5**.

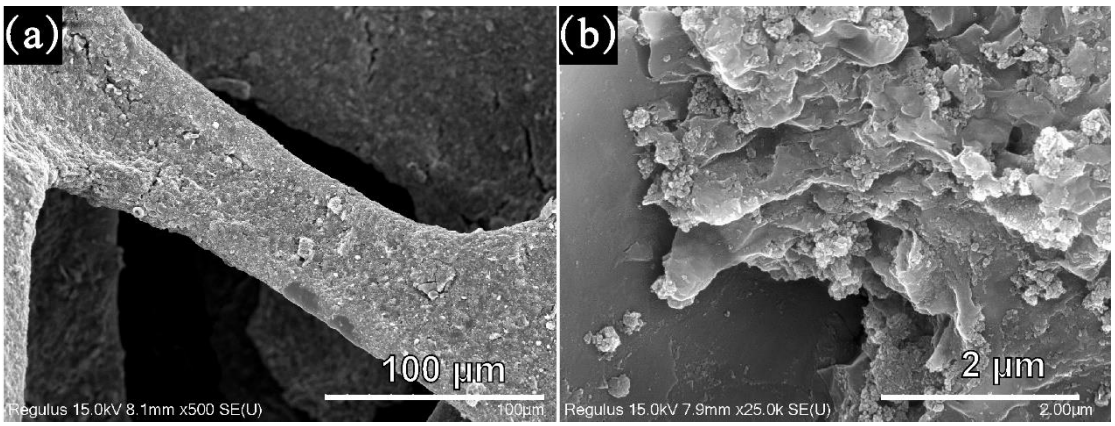

Figure 5.5 (a-b) SEM images of Co_3O_4/MXene composite on Ni foam with the ratio of Co3O4/MXene=4:1 (COMX4) with various magnification.

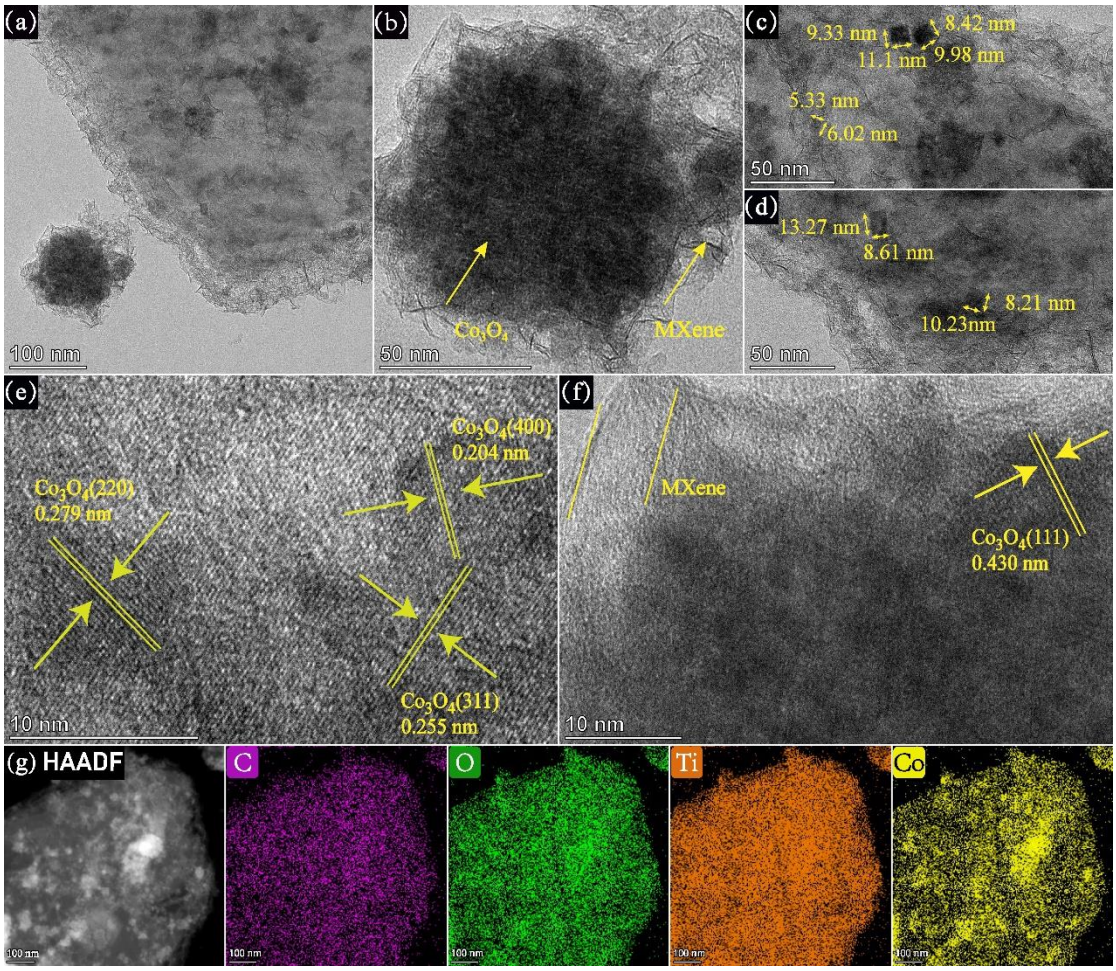

Figure 5.6 (a-d) High-magnification TEM and (e-f) HRTEM images of Co_3O_4/MXene composite with the ratio of Co_3O_4/MXene=1:1 (COMX1). (g) EDS mapping of the as-obtained COMX1 sample.

Figure 5.6 displays the TEM images of Co_3O_4/MXene composite with the ratio of Co_3O_4/MXene=1:1 (COMX1). Corresponding to the SEM images, the high-magnification TEM images in **Figure 5.6a-b** also show the Co_3O_4 nanoparticles encapsulated by MXene nanosheets and demonstrate the uniform distribution of Co_3O_4 nanoparticles within the MXene nanosheets. In **Figure 5.6c-d**, the discernable shape of the Co_3O_4 nanoparticles seems to be diamonds with an ultra-small size of 5~15 nm.

Co_3O_4 nanoparticles with tiny sizes are beneficial for the efficient diffusion of Li-ion through electrodes and the smaller relative swelling stress created during the lithiation process. In addition, the ultrathin MXene nanosheets are approaching transparent in TEM images suggesting the few-layers of MXene. Meanwhile, these MXene nanosheets are flexible with clearly visible wrinkles on the surface. Observed by the high-resolution TEM (HRTEM), the lattice fringe spacings of different crystals were calculated in **Figure 5.6e-f**. The lattice fringe spacings of 0.430, 0.279, 0.255, and 0.204 nm are assigned to the (111), (220), (311), and (400) planes of Co_3O_4, respectively, which is consistent with the characteristic peaks in XRD patterns of Co_3O_4/MXene composite. The EDS element mapping (**Figure 5.6g**) was conducted to investigate the element distribution in the Co_3O_4/MXene composite. The Co_3O_4 nanoparticles are confirmed by the element O and Co while the element C and Ti demonstrate the existence of MXene nanosheets. It is observed that Co and Ti elements overlap and match well, strongly authenticating a homogeneous distribution of Co_3O_4 nanoparticles within MXene nanosheets. To obtain a high-performance composite electrode, the MXene nanosheets are applied to not only relieve the volume expansion of active materials but also increase the electronic and ionic conductivity of the whole electrode by facilitating the transportation of electrons and reducing the Li^+ diffusion barrier. Hence, the excellent distribution of Co_3O_4 nanoparticles within MXene nanosheets indicates the high-performance of the composite electrode.

5.3.2 Electrochemical performance of Co_3O_4/MXene composite

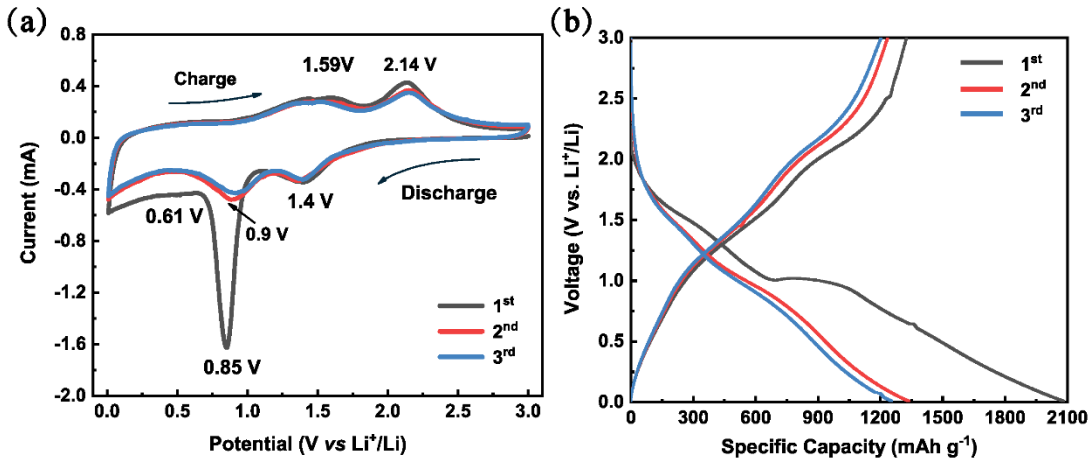

Figure 5.7 (a) Cyclic voltammetry curves for the initial three cycles for the Co_3O_4/MXene composite electrode (COMX1). (b) Charge/discharge profiles of the COMX1 electrode with the initial three cycles at the current density of C/20 (C=890 mA g^{-1}).

To investigate the electrochemical performance of the Co_3O_4/MXene composite electrodes, the cyclic voltammetry (CV) was conducted at a scan rate of 0.1 mV s^{-1} over a potential range of 0.01-3 V (*vs.* Li/Li^+), as shown in **Figure 5.7a**. According to the CV profiles, the lithiation and delithiation processes of Co_3O_4 show a multiple electrochemical reaction behavior [12]. During the first cathodic scan, there is a shoulder peak around 1.4 V corresponding to the reduction procedure from Co_3O_4 to CoO accompanying the production of Li_2O (Equation (14)). After that, a strong and sharp peak appearing at 0.85 V is attributed to the reduction of Co^{2+} to Co^0 and the formation of solid electrolyte interphase (SEI) films (Equation (15)). This reduction peak shifts right to 0.90 V in the following cycles, which indicates not only the

irreversible formation of most SEI films but also the activation process of the electrode leading to the more uniform distribution of Co in the Li_2O matrix and higher transmission efficiency of Li-ions [12, 18]. Besides, there is a small and broad peak near 0.61 V that is ascribed to the insertion of Li^+ in the MXene nanosheets following Equation (16). It is more clear to find this reaction peak in the CV curves of the pristine MXene electrode in **Figure 5.8a**. During the anodic scan, two distinct peaks are locating at 1.59 and 2.14 V, which are related to the oxidation transformation from metallic Co to Co_3O_4 by two steps, respectively. The subsequent CV plots maintain an almost identical shape that reveals the distinguished reversibility of the electrode.

$$Co_3O_4 + 2Li^+ + 2e^- \leftrightarrow 3CoO + Li_2O \quad (14)$$

$$3CoO + 6Li^+ + 6e^- \leftrightarrow 3Co + 3Li_2O \quad (15)$$

$$Ti_3C_2T_x + xLi^+ + xe^- \leftrightarrow Li_xTi_3C_2T_x \quad (16)$$

It is also in good agreement of the galvanostatic charge-discharge (GCD) profiles of the Co_3O_4/MXene composite electrode for the initial three cycles at C/20 in **Figure 5.7b**. In the first discharge profile, two conspicuous discharge plateaus are observed at ~1.54 and 1.01 V corresponding to the reduction of Co_3O_4 to metallic Co and the formation of Li_2O, while two broad peaks appearing at 1.57-1.73 V and 2.1-2.3 V in the first charge profile are associated with the oxidation of the metallic Co accompanying the decomposition of Li_2O to Li. Subsequently, the following cycles exhibit the discharge plateaus with higher voltages, which is consistent with the right shift of the reduction peak in the CV profiles. Moreover, as observed in **Figure 5.7b**,

the first discharge capacity approaches 2082 mAh g^{-1} and a charge capacity is around 1326 mAh g^{-1}, which results in an initial coulomb efficiency of ~63.7 %. On the other hand, the irreversible capacity loss accounts for 36.3 %, mainly caused by the formation of SEI films, the irrecoverable conversion of Co_3O_4, and the partial residual Li^+ in the active materials. Nevertheless, the following cycles exhibit both discharge and charge capacity exceeding the theoretical capacity of 890 mAh g^{-1}. The larger capacity can be ascribed to small contributions from the MXene nanosheets, as shown in **Figure 5.8b**. More importantly, the extra Li-ion storage is attributed to the increased interfacial bonds acting as active sites, which are supplied by the grain boundaries of Li_2O and Co generated during the discharge process [12].

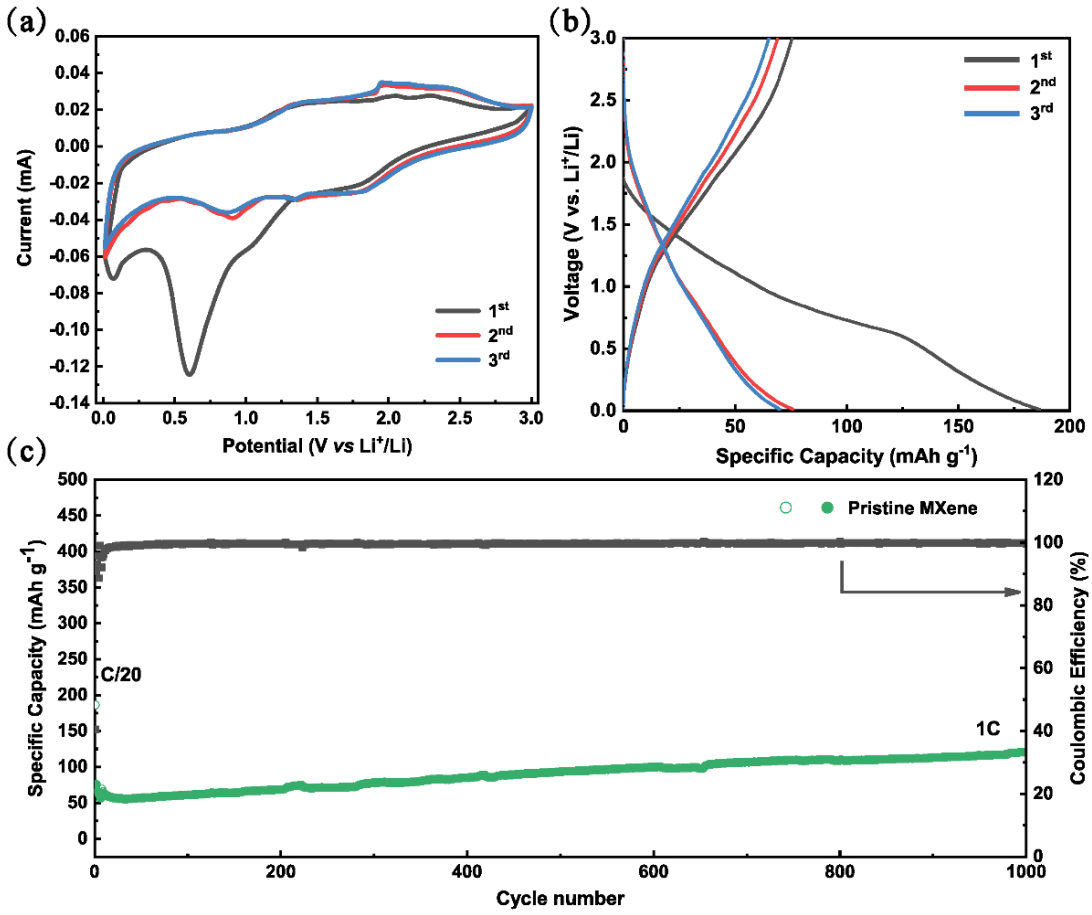

Figure 5.8 (a) Cyclic voltammetry curves for the initial three cycles for the pristine MXene electrode. (b) Charge/discharge profiles of the pristine MXene electrode with the initial three cycles at the current density of C/20. (c) Cycling performance of pristine MXene on Ni foam at the current density of 1 C with three initial cycles at C/20 (C=448 mA g^{-1}).

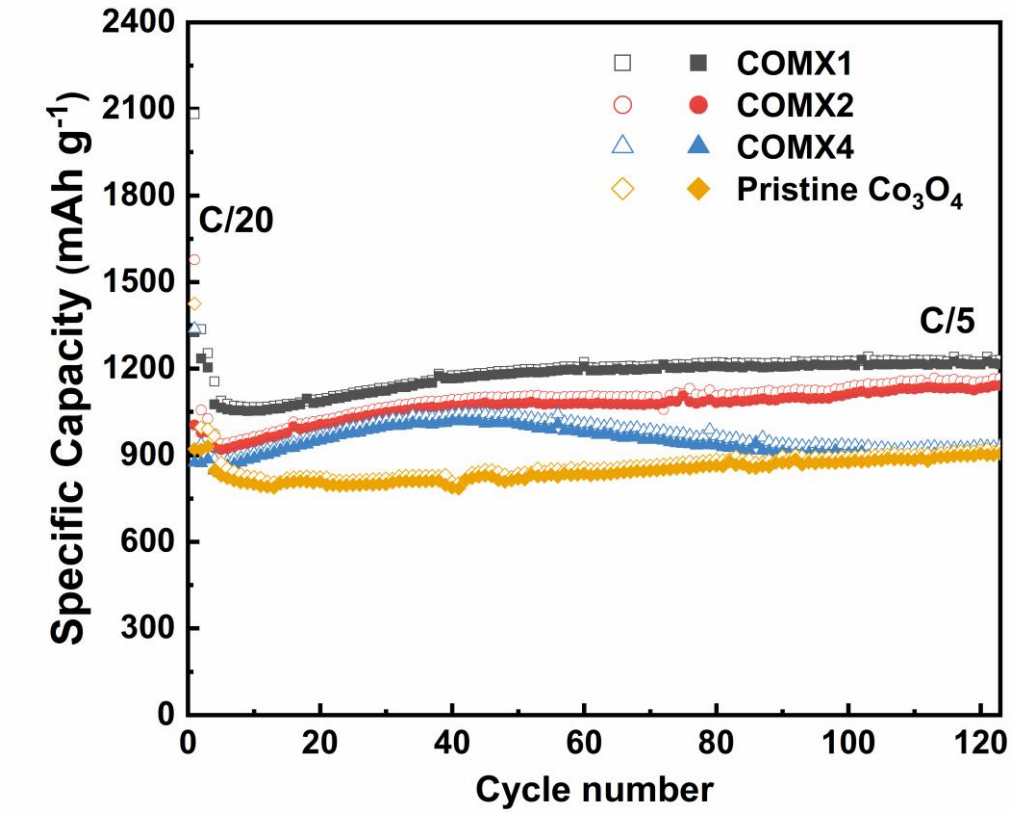

Figure 5.9 Cycling performance of Co_3O_4/MXene composite electrode with different ratios of Co_3O_4/MXene=1:1, 2:1, and 4:1 (labeled with COMX1, 2, and 4), compared with the pristine Co_3O_4 at the current rates of C/5 (C=890 mA g^{-1}).

Figure 5.9 and **Figure 5.10** illustrates the cycling performance of the Co_3O_4/MXene composite electrode with different ratios of Co_3O_4/MXene=1:1, 2:1, and 4:1 (COMX1, 2, and 4), compared with the pristine Co_3O_4 electrode at the current densities of C/5 and 1 C, respectively. Both tests were conducted with three initial cycles at the rate of C/20, aiming to activate and stabilize the batteries. In **Figure 5.9**, at an initial current density of C/20, COMX and pristine Co_3O_4 electrodes show similar initial Coulombic efficiencies between 61-65 %. With fewer MXene nanosheets involved in the composite, the initial Coulombic efficiencies will increase because of

the smaller surface area of electrode, leading to the less irreversible formation of SEI films. It is further confirmed by the cycling performance of the pristine MXene electrode in **Figure 5.8b**, which shows the first discharge/charge capacities of 186.4/75.5 mAh $g^{-1,}$ resulting in an initial Coulombic efficiency of ~40 %. The low reversibility of the pristine MXene electrode owes to the considerable functional groups such as -F and -OH locating on its surface [14]. Therefore, the low content of MXene nanosheets in composite results in higher initial Coulombic efficiency. After the three-cycle initialization, COMX1, COMX2, COMX4, and pristine Co_3O_4 electrodes exhibit the reversible capacities of 1155, 973, 886, and 996 mAh g^{-1}, which remains the capacities of 1230, 1167, 932, and 918 mAh g^{-1} after 120 cycles at the rate of C/5, with the corresponding retention of 106 %, 120 %, 105 %, and 92 %, respectively. It is worth noting that except for the pristine Co_3O_4 electrode, all COMX electrodes increase the capacity by more than 100 percent after 120 cycles, which is caused by the slow activation process for electrolyte ions diffusing through the COMX electrodes when the stacked MXene nanosheets are used [5]. It is further demonstrated in **Figure 5.8c**, where the pristine MXene electrode experiences a minor increase in the specific capacity over a long-term cycling life.

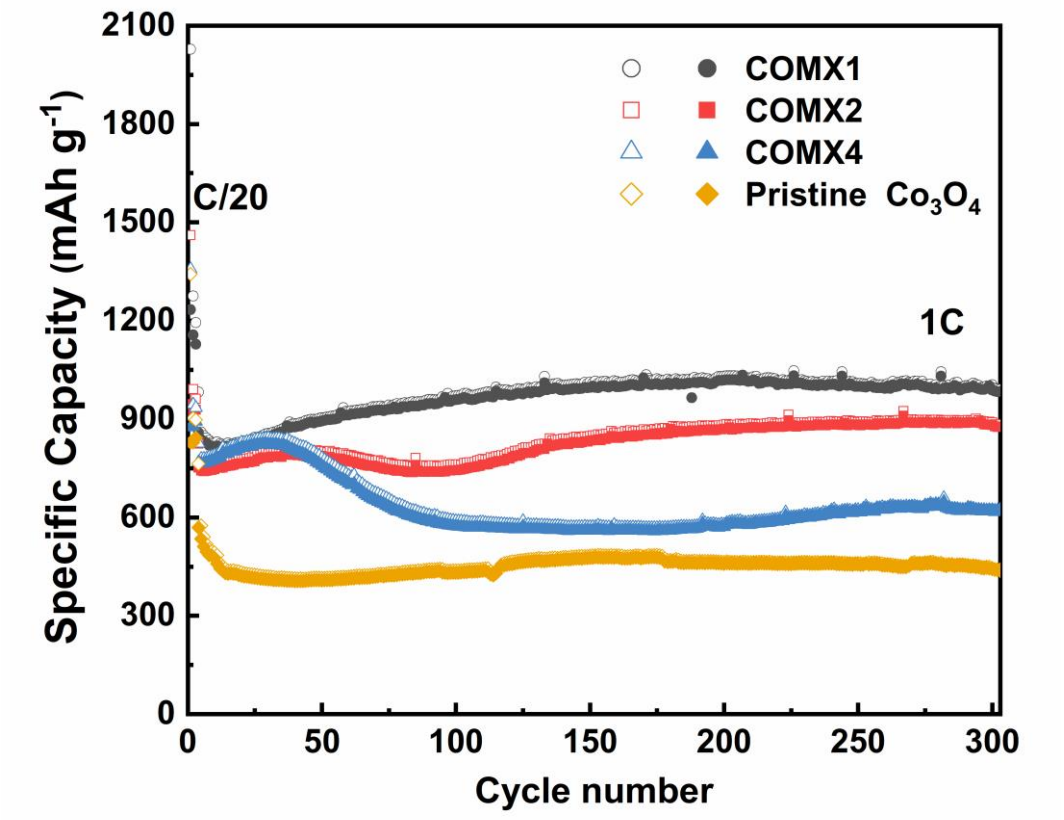

Figure 5.10 Cycling performance of Co_3O_4/MXene composite electrode with different ratios of Co_3O_4/MXene=1:1, 2:1, and 4:1 (labeled with COMX1, 2, and 4), compared with the pristine Co_3O_4 at the current rates of 1 C (C=890 mA g^{-1}).

Likewise, there are almost identical trends for the cycling performance of COMX and pristine Co_3O_4 electrodes at the rate of 1 C in **Figure 5.10**. Compared with the performance of the pristine Co_3O_4 electrode at C/5, the disadvantages of that at 1 C become more noticeable, which arises from the low electrical conductivity of the electrode. Among all the COMX electrodes, the COMX1 electrode shows the highest reversible capacity of 1005 mAh g^{-1} after 300 cycles. The higher percentage of MXene nanosheets in the composite leads to the high Li^+ and electrons transmission efficiency between the electrodes. In contrast, the higher content of Co_3O_4 nanoparticles will not

only have a negative effect on the electrical conductivity of the whole electrode but also increase the agglomeration probability of the nanoparticles leading to the ununiform distribution Co_3O_4 within the MXene nanosheets. However, if the ratio of Co_3O_4 nanoparticles and MXene nanosheets decreases to a specific value, the cycling performance cannot reach the expectation. For example, the cycling performance of the COMX0.5 electrode (Co_3O_4/MXene=1:2) was tested at the current density of 1 C in **Figure 5.11**. By contrast, the COMX0.5 electrode delivers a reversible capacity of 678 mAh g^{-1} after 300 cycles, which is much lower than that of the COMX1 electrode, which is reasonably ascribed to the restacking of MXene nanosheets with fewer Co_3O_4 nanoparticles as spacers. Co_3O_4 nanoparticles play a critical role in separating the MXene nanosheets to prevent them from restacking. Hence, the synergistic effect of MXene nanosheets and Co_3O_4 nanoparticles in the COMX1 electrode fulfills its utmost efficiency.

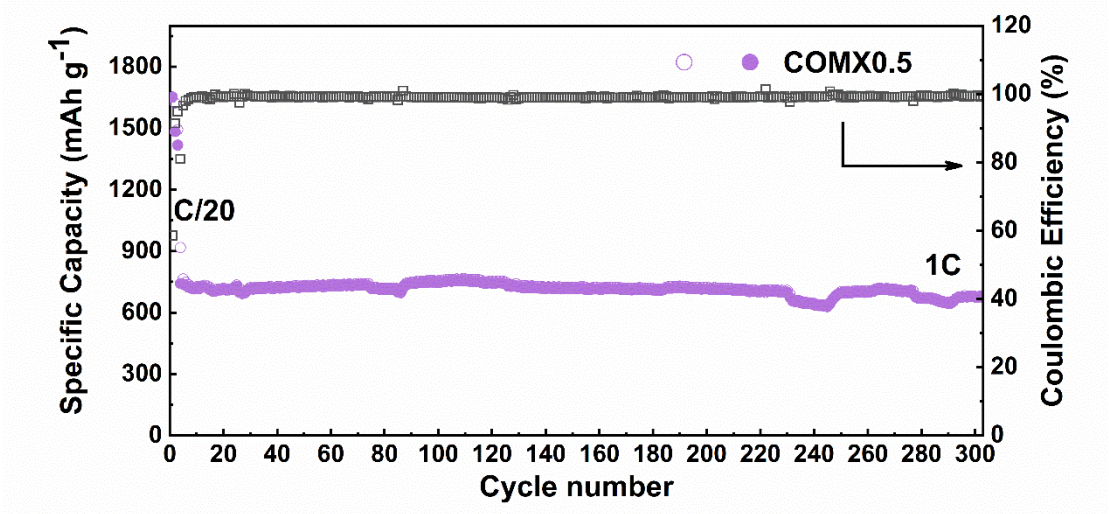

Figure 5.11 Cycling performance of COMX0.5 at the current density of 1 C.

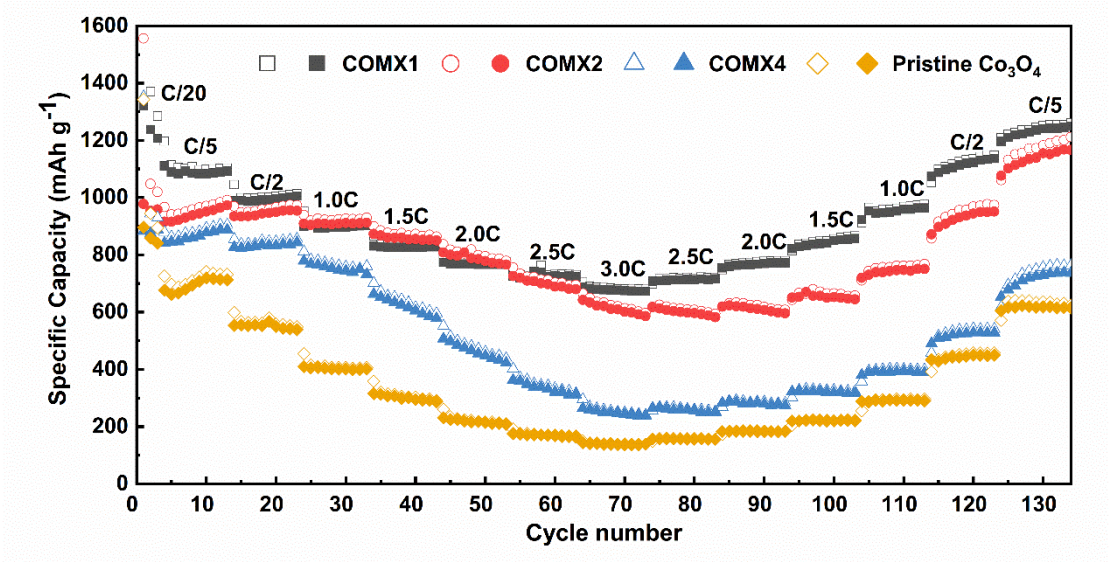

Figure 5.12 Rate capabilities of COMX electrodes with different ratios and pristine Co_3O_4 electrode.

Excellent rate performance of electrode demonstrates the capability of electrodes to support the fast charge and discharge. **Figure 5.12** shows the rate capability of the COMX and pristine Co_3O_4 electrodes at various current densities of C/5, C/2, 1 C, 1.5 C, 2 C, 2.5 C, to 3 C and then back at same rates. The COMX1 electrode delivers the capacities retentions of 100 %, 87 %, 82 %, 75 %, 72 %, 65 %, and 64 %, at the current densities from C/5 to 3 C, respectively. When the current densities return from 3 C to C/5, there is a little increase in the cycling performance due to the laggardly activated Li-ion transporting through the electrodes. Additionally, the COMX1 electrode remains the highest reversible capacities among all electrodes, which are further demonstrated in the Nyquist plots in **Figure 5.13**. The addition of MXene nanosheets can effectively reduce the charge-transfer impedance of Co_3O_4 nanoparticles, which is consistent with

the reduced diameter of the semicircle at the high-frequency region. Accordingly, the COMX1 has the smallest impedance around 35 Ω.

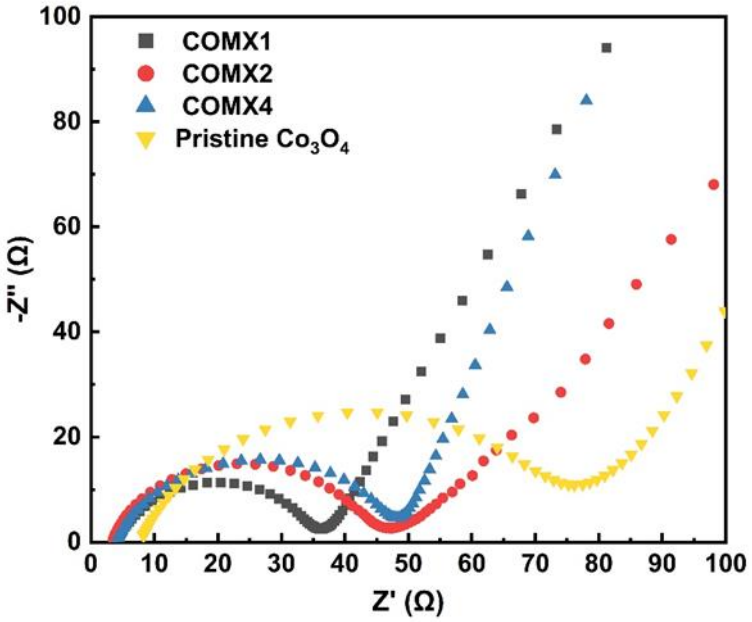

Figure 5.13 Nyquist plots of Co_3O_4/MXene composite with different ratios of Co_3O_4 and MXene.

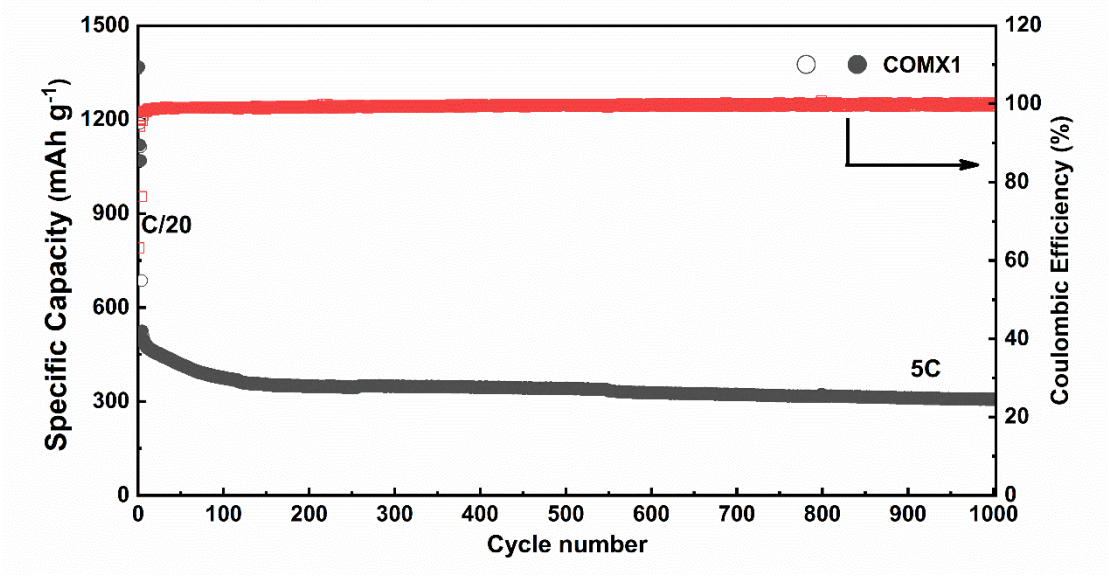

Figure 5.14 Cycling performance of the COMX1 electrode at the current rate of 5 C.

Interestingly, when the current density increases to 5 C as illustrated in **Figure 5.14**, the COMX1 electrode can show a discharge capacity of 307 mAh g^{-1} after 1000 cycles, which implies the long-term stability of the COMX1 electrode. Similarly, the pristine MXene electrode remains the capacity of 76 % after 1000 cycles (**Figure 5.8c**). Therefore, the incorporation of MXene nanosheets with Co_3O_4 enhances the electrical conductivity of the electrode as well as stabilizes the electrode over the long-term cycling by relieving the stress arising from the expansion of active materials.

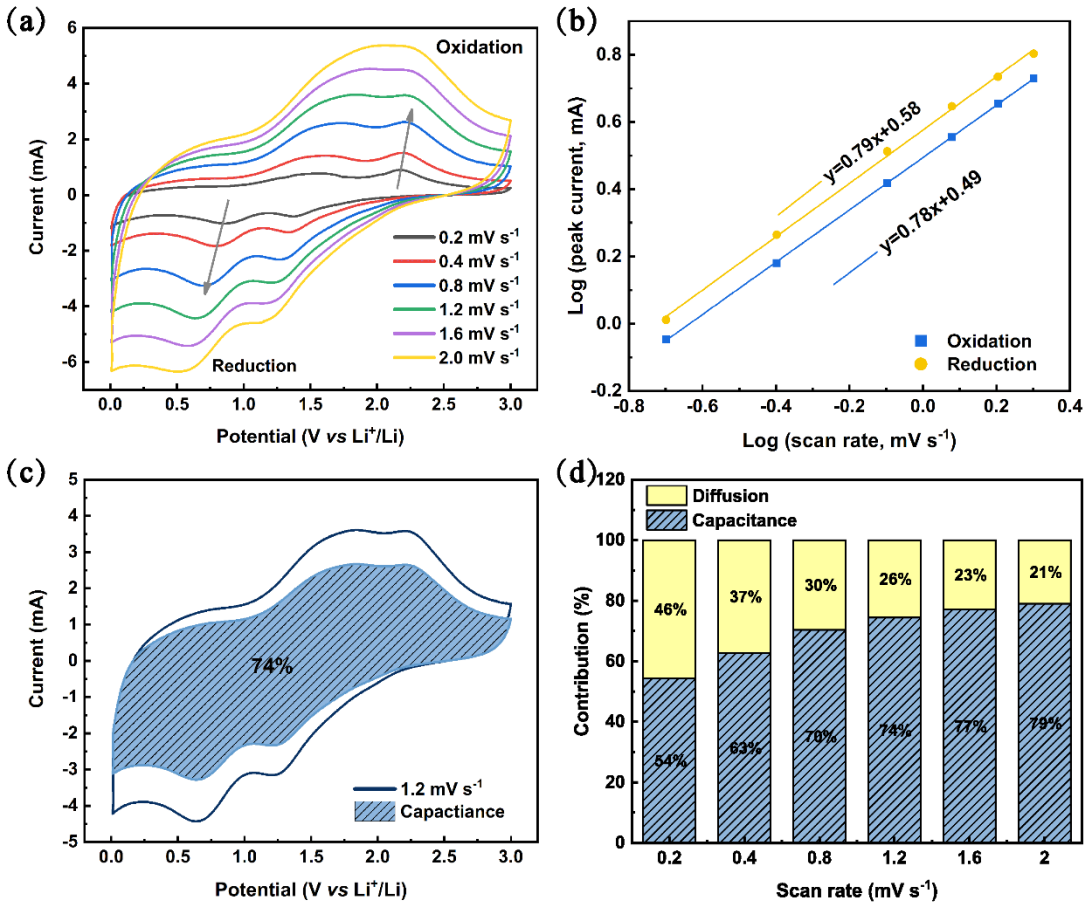

Figure 5.15 (a) CV curves of COMX1 electrode at different sweep speeds of 0.2, 0.4, 0.8,1.2, 1.6, and 2.0 mV s^{-1}. (b) Plots of log(i) versus log(v) depending on reduction and oxidation peaks. (c) Separated diffusion and capacitive current at a scan rate of 1.2 mV s^{-1}. (d) The ratios of the diffusion and capacitive-controlled contributions at different scan rates.

Typically, the capacity of the Co_3O_4/MXene composite electrode is mainly contributed by diffusion-controlled capacity from conversion and alloying reactions and capacitive capacity caused by surface charge transfer [19]. To further understand the electrochemical kinetics of the COMX1 electrode for Li-ion storage, the corresponding CV curves at scan rates ranging from 0.2 to 2 mV s^{-1} were carried out,

as shown in **Figure 5.15a.** The relationship between the current (i) on scan rate (v) can be expressed with Equation (17) and (18) [18]

$$i = av^b \quad \ldots(17)$$

$$\log(i) = b\log(v) + \log(a) \quad \ldots(18)$$

Both a and b are tunable parameters whose value could be determined by the intercept and slope of the plot ($\log(i)$ versus $\log(v)$), as illustrated in **Figure 5.15b**. Generally, b=0.5 represents an ideal diffusion-controlled intercalation procedure and $b = 1$ indicates the surface-induced capacitive procedure. According to **Figure 5.15b**, b is equal to 0.79 and 0.78 for oxidation and reduction, respectively, implying the concurrence of two kinds of capacity contributions in the COMX1 electrode. Moreover, the proportion of two-kind contributions can be quantitatively confirmed by separating the current response (i) at a fixed potential V into the capacitive process ($k_1 v$) and the diffusion-controlled process ($k_2 v^{0.5}$) following the Equation (19) [14, 20]

$$i(V) = k_1 v + k_2 v^{0.5} \quad \ldots(19)$$

To determine the constant value of k_1 and k_2, Equation (19) was transformed into Equation (20) by dividing the $v^{0.5}$ at both sides [21]. Hence, k_1 and k_2 are determined by the slope and intercept of the plots of $i(V)/v^{0.5}$ and $v^{0.5}$.

$$i(V)/v^{0.5} = k_1 v^{0.5} + k_2 \quad \ldots(20)$$

With the explicit k_1 and k_2, the contribution from the capacitive process ($k_1 v$) and the diffusion-controlled process ($k_2 v^{0.5}$) were calculated. For example, the typical voltage profile at the scan rate of 1.2 mV s^{-1} was shown in **Figure 5.15c**, in which a dominating capacitive current (shadow region) accounts for ~74 % compared with the total current, revealing that the electrode is inclined to surface-induced charge storage procedure. With the increasing sweep rate, the COMX1 electrode displays enlarged capacitive contributions of 54 %, 63 %, 70 %, 74 %, 77 %, and 79 %, respectively (**Figure 5.15d**). Interestingly, it is the surface-induced capacitive procedure that plays a significant role in the total current, which is ascribed to the tiny-size Co_3O_4 nanoparticles and stable composite structure. Moreover, the highly conductive MXene nanosheets favor the charge transfer kinetics in the composite electrode. Therefore, the dominating surface-induced capacitive procedure contributes to enhancing the rate capability of the COMX1 electrode, which also explains that the COMX1 electrode delivers a much larger capacity than the theoretical capacity.

5.4 Conclusion

In conclusion, the Co_3O_4/MXene composite electrodes can be prepared with high-performance for the enhanced LIBs. The 2D MXene nanosheets serve as substrates for Co_3O_4 nanoparticles to relieve the stress arising from the huge volume expansion of Co_3O_4 during the charge/discharge processes. More importantly, the highly conductive MXene nanosheets promote the electronic and ionic conductivity of the whole electrode with a higher transmission efficiency of Li^+ and electrons. Moreover, the addition of MXene nanosheets can enhance the stability of Co_3O_4/MXene composite electrodes over long-term cycling. Besides, the moderate content of Co_3O_4 nanoparticles could efficiently limit the restacking of MXene nanosheets. The facile preparation method and the excellent electrochemical performance of Co_3O_4/MXene composite electrodes promise it as a competitive anode for LIBs.

5.5 References

[1] Y. Tian, Y. An, and J. Feng, "Flexible and Freestanding Silicon/MXene Composite Papers for High-Performance Lithium-Ion Batteries," *ACS Appl Mater Interfaces,* vol. 11, no. 10, pp. 10004-10011, 2019.

[2] A. Byeon, M. Q. Zhao, C. E. Ren, J. Halim, S. Kota, P. Urbankowski, B. Anasori, M. W. Barsoum, and Y. Gogotsi, "Two-Dimensional Titanium Carbide MXene As a Cathode Material for Hybrid Magnesium/Lithium-Ion Batteries," *ACS Applied Materials & Interfaces,* vol. 9, no. 5, pp. 4296-4300, 2017.

[3] S. Luo, R. Wang, J. Yin, T. Jiao, K. Chen, G. Zou, L. Zhang, J. Zhou, L. Zhang, and Q. Peng, "Preparation and Dye Degradation Performances of Self-Assembled MXene-Co_3O_4 Nanocomposites Synthesized via Solvothermal Approach," *ACS Omega,* vol. 4, no. 2, pp. 3946-3953, 2019.

[4] R. Deng, B. Chen, H. Li, K. Zhang, T. Zhang, Y. Yu, and L. Song, "MXene/Co_3O_4 Composite Material: Stable Synthesis and Its Enhanced Broadband Microwave Absorption," *Applied Surface Science,* vol. 488, pp. 921-930, 2019.

[5] M. Q. Zhao, M. Torelli, C. E. Ren, M. Ghidiu, Z. Ling, B. Anasori, M. W. Barsoum, and Y. Gogotsi, "2D Titanium Carbide and Transition Metal Oxides Hybrid Electrodes for Li-Ion Storage," *Nano Energy,* vol. 30, pp. 603-613, 2016.

[6] P. Zhang, Q. Zhu, Z. Guan, Q. Zhao, N. Sun, and B. Xu, "A Flexible Si@C Electrode with Excellent Stability Employing an MXene as a Multifunctional Binder for Lithium-Ion Batteries," *ChemSusChem,* 2019.

[7] Y. T. Liu, P. Zhang, N. Sun, B. Anasori, Q. Z. Zhu, H. Liu, Y. Gogotsi, and B. Xu, "Self-Assembly of Transition Metal Oxide Nanostructures on MXene Nanosheets for Fast and Stable Lithium Storage," *Adv Mater,* vol. 30, no. 23, p. 1707334, 2018.

[8] M. R. Lukatskaya, O. Mashtalir, C. E. Ren, Y. Dall'Agnese, P. Rozier, P. L. Taberna, M. Naguib, P. Simon, M. W. Barsoum, and Y. Gogotsi, "Cation Intercalation and High Volumetric Capacitance of Two-Dimensional Titanium

Carbide," *Science,* vol. 341, no. 6153, pp. 1502-1505, 2013.

[9] M. Gu, Y. He, J. Zheng, and C. Wang, "Nanoscale Silicon as Anode for Li-Ion Batteries: The Fundamentals, Promises, and Challenges," *Nano Energy,* vol. 17, pp. 366-383, 2015.

[10] Z. Ma, X. Zhou, W. Deng, D. Lei, and Z. Liu, "3D Porous MXene (Ti_3C_2)/Reduced Graphene Oxide Hybrid Films for Advanced Lithium Storage," *ACS Appl Mater Interfaces,* vol. 10, no. 4, pp. 3634-3643, 2018.

[11] J. Yan, C. E. Ren, K. Maleski, C. B. Hatter, B. Anasori, P. Urbankowski, A. Sarycheva, and Y. Gogotsi, "Flexible MXene/Graphene Films for Ultrafast Supercapacitors with Outstanding Volumetric Capacitance," *Advanced Functional Materials,* vol. 27, no. 30, 2017.

[12] M. Liu, X. Deng, Y. Ma, W. Xie, X. Hou, Y. Fu, and D. He, "Well-Designed Hierarchical Co_3O_4 Architecture as a Long-Life and Ultrahigh Rate Capacity Anode for Advanced Lithium-Ion Batteries," *Advanced Materials Interfaces,* vol. 4, no. 19, p. 1700553, 2017.

[13] Y. Chen, Y. Wang, Z. Wang, M. Zou, H. Zhang, W. Zhao, M. Yousaf, L. Yang, A. Cao, and R. P. S. Han, "Densification by Compaction as an Effective Low-Cost Method to Attain a High Areal Lithium Storage Capacity in a CNT@Co_3O_4 Sponge," *Advanced Energy Materials,* vol. 8, no. 19, 2018.

[14] X. Sun, K. Tan, Y. Liu, J. Zhang, D. K. Denis, F. U. Zaman, L. Hou, and C. Yuan, "A Two-Dimensional Assembly of Ultrafine Cobalt Oxide Nanocrystallites Anchored on Single-Layer $Ti_3C_2T_x$ Nanosheets with Enhanced Lithium Storage for Li-Ion Batteries," *Nanoscale,* vol. 11, no. 36, pp. 16755-16766, 2019.

[15] D. C. Zuo, S. C. Song, C. s. An, L. B. Tang, Z. J. He, and J. C. Zheng, "Synthesis of Sandwich-Like Structured Sn/SnOx@MXene Composite through In-Situ Growth for Highly Reversible Lithium Storage," *Nano Energy,* vol. 62, pp. 401-409, 2019.

[16] Y. Deng, T. Shang, Z. Wu, Y. Tao, C. Luo, J. Liang, D. Han, R. Lyu, C. Qi, W. Lv, F. Kang, and Q. H. Yang, "Fast Gelation of $Ti_3C_2T_x$ MXene Initiated by

Metal Ions," *Adv Mater,* p. 1902432, 2019.

[17] M. Naguib, O. Mashtalir, M. R. Lukatskaya, B. Dyatkin, C. Zhang, V. Presser, Y. Gogotsi, and M. W. Barsoum, "One-Step Synthesis of Nanocrystalline Transition Metal Oxides on Thin Sheets of Disordered Graphitic Carbon by Oxidation of MXenes," *Chem Commun (Camb),* vol. 50, no. 56, pp. 7420-3, 2014.

[18] X. Zhao, H. Xu, Z. Hui, Y. Sun, C. Yu, J. Xue, R. Zhou, L. Wang, H. Dai, Y. Zhao, J. Yang, J. Zhou, Q. Chen, G. Sun, and W. Huang, "Electrostatically Assembling 2D Nanosheets of MXene and MOF-Derivatives into 3D Hollow Frameworks for Enhanced Lithium Storage," *Small,* p. 1904255, 2019.

[19] Q. Li, Y. Zhao, H. Liu, P. Xu, L. Yang, K. Pei, Q. Zeng, Y. Feng, P. Wang, and R. Che, "Dandelion-Like Mn/Ni Co-Doped CoO/C Hollow Microspheres with Oxygen Vacancies for Advanced Lithium Storage," *ACS Nano,* vol. 13, no. 10, pp. 11921-11934, 2019.

[20] T. Brezesinski, J. Wang, J. Polleux, B. Dunn, and S. H. Tolbert, "Templated Nanocrystal-Based Porous TiO_2 Films for Next-Generation Electrochemical Capacitors," *Journal of the American Chemical Society,* vol. 131, no. 5, pp. 1802-1809, 2009.

[21] D. Chao, C. Zhu, P. Yang, X. Xia, J. Liu, J. Wang, X. Fan, S. V. Savilov, J. Lin, H. J. Fan, and Z. X. Shen, "Array of Nanosheets Render Ultrafast and High-Capacity Na-Ion Storage by Tunable Pseudocapacitance," *Nat Commun,* vol. 7, p. 12122, 2016.

Chapter 6: Conclusion and perspectives

6.1 Conclusion

This thesis illustrates the investigation of employing highly conductive materials in anode for LIBs to improve electrochemical performance. The highly conductive materials not only enhance the rate capability of the electrode by providing the highly efficient electrons and ions pathways but also relieve the stress induced by the huge volume expansion during charge and discharge processes through building the 3D stable framework with considerable interspace.

The Cu NWs were employed to build the 3D conductive structure for Si anode. Firstly, Cu NWs cooperating with MWCNTs formed the porous structure on the current collector to support Si. Secondly, the Si NPs were distributed within the 3D conductive framework created by Cu NWs and encapsulated by carbon layers. Both MWCNTs/Cu NWs/Si and Cu NWs/Si NPs@C composite electrodes exhibited excellent cycling performance with enhanced rate capability as well as stability over long-term cycling. Finally, the novel MXene nanosheets were introduced to substitute the Cu NWs and carbon materials in the electrode, due to its high electrical conductivity and physical strength. MXene nanosheets were combined with the Co_3O_4 nanoparticles, which made a breakthrough in the electrochemical performance of Co_3O_4-based LIBs.

6.2 Perspectives

In this thesis, the highly conductive materials were used in the anode for Li-ion batteries to improve the electrical conductivity of the electrode. Meanwhile, these highly conductive materials could create a 3D porous framework to support the active materials and provide numerous void space to accommodate the massive volume change. The design is expected to be used in the industry to improve the commercialized Li-ion batteries. The mass production of Li-ions batteries requires the facile fabrication procedure and the large surface area of the electrode for pouch cells. The preparation of the 3D framework should be simple to promote the efficiency of production. In addition, the excellent physical properties of materials should maintain when the area of the whole electrode is enlarged. Unfortunately, under the same thickness, the structure of some materials tend to be inflexible and breakable with the increased area. Therefore, the choice of the highly conductive materials for 3D framework during mass production in the industry needs cautions.

If the design is applied in the industry for mass production of Li-ion batteries, the huge mass loading is required for large energy density. The ways to improve the mass loading on the 3D framework involve the increase in mass per areal, which may lead to the instability of the framework and long transport way of Li-ions. The other method is enlarging the thickness of the whole electrode to increase mass loading. However, the corresponding challenges include the ununiform distribution of the active materials within the thicker framework and the insufficient of the Li-ions transmission within the

anode. To solve these challenges, a 3D framework with a controllable void size could be contrived, which results in adjustable mass loading on the framework. According to the environmental effects in different categories of batteries, this framework materials could be flexible to accommodate the different requirements of batteries, such as pouch cells or coin cells.